



(1)

Final Technical Report

LOW FREQUENCY ACTIVE SIGNAL DETECTION METHODOLOGY
AND SIMULATION EMPLOYING DISCRETE WAVELET TRANSFORMS

November 1992

Sponsored by:

Defense Advanced Research Projects Agency
Undersea Warfare Office
AntiSubmarine Warfare Program
ARPA Order No. 7914 612
Issued by ~~OSR~~ under Contract MDA 91-C-0077

DTIC
ELECTE
FEB 4 1993
S C D

93-01914



15708

Prepared by:

Daniel H. Wagner Associates
894 Ross Drive, Suite 205
Sunnyvale, CA 94089

CLEARED
FOR OPEN PUBLICATION

JAN 28 1993

3

DIRECTORATE FOR FREEDOM OF INFORMATION
AND SECURITY REVIEW (OASD-PA)
DEPARTMENT OF DEFENSE

DISTRIBUTION STATEMENT A

Approved for public release
Distribution Unlimited

By:

Eric Dew
Eric Dew

Reviewed:

Stanley J. Benkoski
Stanley J. Benkoski

By:

Robert J. Lipshutz
Robert J. Lipshutz

Approved:

Stanley J. Benkoski
Stanley J. Benkoski

"The views and conclusions contained in this document are those of the authors and should not be interpreted as representing the official policies, either express or implied, of the Defense Advanced Research Projects Agency or any other part of the U.S. Government."

Final Technical Report

**LOW FREQUENCY ACTIVE SIGNAL DETECTION METHODOLOGY
AND SIMULATION EMPLOYING DISCRETE WAVELET TRANSFORMS**

November 1992

Sponsored by:

Defense Advanced Research Projects Agency
Undersea Warfare Office
AntiSubmarine Warfare Program
ARPA Order No. 7914 612✓
Issued by ~~OWO~~ under Contract MDA-91-C-0077

Prepared by:

Daniel H. Wagner Associates
894 Ross Drive, Suite 205
Sunnyvale, CA 94089

By: Eric Dew
Eric Dew

Reviewed: Stanley J. Benkoski
Stanley J. Benkoski

By: Robert J. Lipshutz
Robert J. Lipshutz

Approved: Stanley J. Benkoski
Stanley J. Benkoski

"The views and conclusions contained in this document are those of the authors and should not be interpreted as representing the official policies, either express or implied, of the Defense Advanced Research Projects Agency or any other part of the U.S. Government."

TABLE OF CONTENTS

PREFACE.....	iv
SUMMARY.....	v
CHAPTER I INTRODUCTION	1
CHAPTER II BACKGROUND AND NOTATIONS	6
CHAPTER III DISCRETE WAVELET THEORY.....	16
CHAPTER IV DETECTION ALGORITHM	38
CHAPTER V SIGNAL SELECTION.....	43
CHAPTER VI THE SIMULATION SYSTEM AND A DESCRIPTION OF THE EXPERIMENTS	83
CHAPTER VII SUMMARY OF THE EXPERIMENTAL RESULTS.....	103
CHAPTER VIII CONCLUSIONS FROM THE PRESENT RESEARCH	142
CHAPTER IX RECOMMENDATIONS FOR FUTURE RESEARCH.....	145
REFERENCES.....	148

DTIC QUALITY INSPECTED 3

Accession For	
NTIS SECRET	<input checked="" type="checkbox"/>
DTIC TAB	<input type="checkbox"/>
Unannounced	<input type="checkbox"/>
Justification	
By <i>Rec Hc</i>	
Distribution/	
Availability Codes	
Dist	Special
<i>A-1</i>	

PREFACE

This report is the final report on the tasking by Daniel H. Wagner Associates to the Defense Advanced Research Projects Agency (DARPA) under contract MDA 972-91-C-0077. The aim of the research is to develop low frequency active/low probability of intercept acoustic signals and detection mechanism. Our approach includes implementing the discrete wavelet theory for detection and classification purposes.

The principal investigator is Dr. Robert J. Lipshutz. Contributors to this report include Dr. Eric Dew and Mr. Darren Miner. Mr. Derek Bernhart, Ms. Kirsten Holmquist, Mr. Jason Kastner, and Ms. Angela Schillace provided additional support for software development, graphics production, computation results, and the write-up of the User's Guide for the transmission simulation system. Consulting services were provided by Dr. Jay Epperson and Dr. Michael Frazier.

SUMMARY

This final report presents the methodology used and the results achieved in the Low Frequency Active/Low Probability of Intercept research project for DARPA.

THE PROBLEM. The general objective of this work is to develop a fast, accurate signal detection methodology based on Discrete Wavelet Theory. The questions addressed in this report include:

- **Sonar signal choice.** We discuss the general types of sonar signals currently in use. The choice of sonar signals must take into account Doppler and other transmission effects, probability of intercept, and type of information one wants the signal to relay. Physical constraints such as projector characteristics will also play a role in determining the type of signals one can send.
- **Signal detection.** One needs a quantitative measure to determine whether a return signal is present in the incoming sample. This measurement is made difficult by the presence of stochastic noise in the return signal. An additional complication arises in shallow water scenarios. Here, the sound channel includes multiple paths due to bottom bounce. Multiple paths change the structure of the signal quite significantly, and sometimes by so much so that one cannot recognize the relation between the return signal and the prototype signal.

In the processing end, one needs to know where the signal lies within the detection window. Such information yields understanding about the target's position or momentum.

- **Choosing a detector.** Although we have settled on the optimal Neyman-Pearson detection algorithm, its implementation in the compressed version is basis dependent. For a given sonar signal choice, one would want a basis which is capable of efficiently detecting the return of this signal.
- **Algorithm speed.** The computation must be fast enough to handle a constant stream of incoming information in real time.

METHODOLOGICAL RESULTS. Some of the methodological results are:

- **Construction of a multi-level wavelet basis from two generating functions.** Examples include the real Shannon basis and the Daubechies D_4 basis. We also include the Haar basis for mathematical illustration.
- **Construction of a multi-level wavelet basis in which the p^{th} -level wavelet function approximates a given signal.** This technique allows one to tailor the wavelet transform to detect a given signal.
- **Construction of a multi-level wavelet basis in which all the wavelet functions from each level are close to a given signal.** This technique is designed to yield small compression loss for reproduction and detection purposes.
- **Construction of a multi-level wavelet basis in which wavelet functions are close to a given signal and to all rotations of it.** This technique allows one to tailor the wavelet transform to detection of a given signal in a robust manner, allowing for errors in positioning the signal in the sample window.
- **Construction of specialized signal types.** These are standard sonar signals having varying properties. These properties include being invariant or very sensitive to Doppler shifts.
- **Description of the compressed Neyman-Pearson detector.** We give formulas for compressing the standard Neyman-Pearson detector using wavelets so as to increase the speed of the algorithm without significantly degrading performance.
- **Description of the multi-channel detector.** This detector is based on the compressed Neyman-Pearson detector and a p -level l^2 -closest orthonormal wavelet basis. It is designed to detect the presence of any translate of a returned signal even when there is Doppler shifting.

EMPIRICAL RESULTS. In order to test the utility of wavelet-based detectors, we created a set of five standard signal types common to sonar processing. These types are continuous wave (CW), hyperbolic frequency modulated (HFM), linear frequency modulated (LFM), pulse (PUL), and pseudo-random noise (PRN). These signals are depicted in Figure V-2. Individual signals of each type are made by setting certain signal parameters like the bandwidth or the sampling

frequency. "Chip" signals are constructed by concatenating a sequence of the above type signals. Transmission effects are simulated on a chip signal, including Doppler shifting, and the signal is offset to model the effect of not capturing the returned signal properly in the receiving sample window. The multi-channel detector methodology uses the compressed Neyman-Pearson detector. The basis choice used in this detector is made by the user. We show that orthonormal l^2 -closest wavelet bases generally outperform the more standard bases like the Fourier basis or the delta (time) basis. Details of the test results are given in Chapter VII. The major empirical results are:

- **The l^2 -closest wavelet basis outperforms the other wavelet bases tested using the compressed Neyman-Pearson detector.**
- **The l^2 -closest wavelet basis performs best for an unaffected signal with no offset or Doppler shifting.**
- **Our experiments with the multi-channel detector were successful in that the detector carried out all the tasks requested. However, the experimental results were not enlightening. The rather uninformative results were due mainly to the choice of the prototype signal. On the other hand, the multi-channel detector showed that only by using wavelets could such results be achieved. Wavelets allowed for compact storage and efficient recursive algorithms, which were all exploited in building the multi-channel detector.**
- **We have built several time-frequency distributions, or spectrograms. These spectrograms give us a new way to analyze signals. The wavelet spectrogram is another way to see the power of the time-frequency localization of wavelet theory.**

FURTHER RESEARCH. Recommendations for further research include the following:

- Conduct simulation studies using real world noise.
- Conduct simulation studies to model real world transmission channels.
- Conduct at-sea tests using proposed signals and analyzing methodologies.

- Continue study on other potential uses of these l^2 -closest wavelet basis for signal processing.
- Continue study on other types of discrete wavelets, perhaps those that are more effective for time-frequency analysis.
- Enhance and refine the current transmission models used in the simulation software.

CHAPTER I

INTRODUCTION

This document is the final report on the Low Frequency Active / Low Probability of Intercept Sonar Signals research work for DARPA. This report highlights results using discrete wavelet theory in the development of near-optimal detection schemes. We also detail the construction of the sonar signals, their characteristics, and their effectiveness. Since we wish to emphasize practical results over theoretical results in this report, we give only a summary of the theory. Our main premise is that wavelet theory, especially the development of the " l^2 -closest" discrete wavelet bases, shows substantial performance improvement over standard bases (i.e., the delta basis and the Fourier basis) for signal detection and computational efficiency.

Additionally, we have created a simulation system to simulate the effects of transmitting a sonar signal underwater – including Doppler effects and bottom bounce – to test the effectiveness of the detection method as well as to highlight the characteristics of the various sonar signals that we produce. User directions and details of the front-end are given in the User's Guide: Low Frequency Active Simulation System, Reference [a].

1. Overview of the Contents

A complete understanding of sonar system technology is beyond the scope of any one report. A sonar system entails everything from transmission to reception. On the transmission end, this includes the hardware choice for the transmitter, signal choice, power capabilities, transmitter characteristics, and signal strength. After transmission, one has to deal with media effects (i.e., effects on the signal during its trip from transmitter to receiver), such as reverberation, Doppler effects, transmission loss, ambient noise, reflection characteristics, and bottom bounce. Finally, at the receiving end, one has to deal with signal detection, classification of signal type, interpretation of the return signal (e.g., has the signal been Doppler-shifted?), receiver characteristics, and other associated problems. We should add that we are considering only active sonar signals, that is, signals that the receiving team has sent out. Passive sonar technology is – by default – simpler at the transmitting end, but much more difficult at the receiving end.

Our research concentrates on two main aspects of the sonar system. One aspect is the signal processing phase of the system – that is, the receiving end, and in particular, signal detection. We assume that the "received" signal – one which is ready to input to the detector – has

already been discretized and windowed. Thus, the received signal is represented by a vector $\mathbf{s} = \mathbf{s}[n] = (s(0), s(1), \dots, s(N-1))$, where each $s(k)$ is a complex number. Chapters III and IV discuss discrete wavelet theory and the optimal (and near-optimal) Neyman-Pearson detection method, respectively.

The second aspect deals with a part of the transmitting phase of the system, namely the signal choice. Here, we construct and evaluate several standard signal types, generically called "chirps" or "chips." Different signal types have different characteristics, some of which are useful for certain purposes and some of which are totally useless for those same purposes. For example, some signals are capable of detecting Doppler shifts; some are invariant under Doppler shifts. Thus, the latter would not be a wise choice if one wants to know whether the target is moving or stationary. These topics are discussed in Chapter V.

Although we did not research transmission effects (e.g., reverberation and bottom bounce) in the same vein as the above two aspects, we did develop a simulation system to model these effects. Additionally, we developed a multi-channel detector, using the compressed Neyman-Pearson (near-optimal) detector technology, to simultaneously detect a range of possible Doppler shifts of an active signal. Both the simulation model and the multi-channel detector are detailed in Chapter VI. Chapter VII gives the results of our research and includes many graphs supporting the claim that certain wavelet bases perform better than other bases for detection purposes.

The areas that are not addressed in this report and that were not considered during the research consist mainly of hardware and software-hardware interface issues (such as size of window, type of windowing function, and sampling rate). However, we do address issues concerning computing time and memory storage capabilities. We strive to minimize computing time, and this is achieved to some extent through the use of wavelets. The recursive nature of wavelet functions also allows one to minimize storage problems. We add here that these issues are not separate from the above issues of signal detection and generation and transmission simulation. Our research in detection methods was guided in part by selecting those algorithms that minimize computing time. The multi-channel detector, on the other hand, was created only after realizing the potential storage savings that wavelets afford, as opposed to other bases like the Fourier basis.

2. Sonar Signal Technology

Sonar systems are prescribed by certain parameters, collectively known as the sonar parameters. These basic parameters are needed when designing the system. Since we are not designing the system, we have assumed reasonable values for these parameters. Some parameters are unnecessary for us to specify; others are specified, but need not be strictly adhered to. The classes of sonar parameters considered are:

- Projector size. This measures the power output capabilities of the sonar projector. This parameter is used mainly in the simulation model.
- Projector characteristics. This describes the frequency spectrum of the projector. This parameter is also used in the simulation model.
- Transmission effects. These parameters include:
 - Bottom bounce and reverberation (for shallow water scenarios).
 - Doppler effects. We assume relative speeds < 15 knots (kts).
 - Distance attenuation. Total source-to-target-to-receiver distances are in the 50–100 nautical mile (nm) range.
 - Noise. There are a number of noise sources. One is biologics, like schools of fish or whales. Shipping also produces noise, mainly from the blades and the trailing eddies. Natural convection of fluids also produces a characteristic noise. Reverberation of all the above noise upon topography (e.g., rocks) and biologics (a school of fish can reflect noise) also produces noise.

The noises described above are not entirely stochastic; that is, each type is characteristic of the source. For example, propellor noise is distinctly in the 50 or 60 Hertz (Hz) range. There is another source of noise that is purely stochastic. This source is the ambient "white" noise that is present in every system (including the machines that transmit, receive, and analyze signals). In the detection algorithm, we assume only white noise. We have not modeled real noise for use in the detection algorithm, although real noise can be applied in the simulation system. Such implementation requires further research into stochastic noise modeling.

- Target strength and reflective properties. This measures the effective signal reflection of the target based on its orientation relative to the signal path and on the reflective surface characteristics of the target.

3. Broad Technical Issues

As stated in Section 1 above, we concentrate on two main aspects of sonar systems technology. The first is detection, and the second is signal creation. The primary issue concerning detection is the following question:

Is there a signal? Even in an active sonar system, in which the time of transmission is known, it is impossible to know exactly when the signal will return. Thus, the receiver is constantly receiving something that we generically call "incoming signal." Embedded in this incoming signal may be the active signal that was transmitted. One only has to detect it above the ever-present noise. However, the active signal has undergone significant changes due to the transmission effects. (By modeling the transmission effects, we hope to give an accurate simulation of a returned signal to test the detector.)

The detector is a variation of the Neyman-Pearson detector. The Neyman-Pearson detector is optimal in the sense that for a fixed probability of false alarm and Gaussian noise, the detector has the highest probability of detection. The near-optimal versions, which we use, sacrifice optimality for computing speed. Nevertheless, our research shows that wavelet-based compressed Neyman-Pearson detectors do not lose much optimality in return for substantial gains in computing speed.

A subtler issue is the location of the signal within the window. The location of the active signal within the window yields range information, which is essential. On the other hand, the detector should be location-invariant. This means the detector should detect the presence of the active signal positioned anywhere in the window. Certain bases (such as the delta basis) give better range information than other bases, but the drawback is that detectors using this delta basis do not perform equally well when the signal is translated within the window.

This trade-off is part of a broader constraint known as the Uncertainty Principle. The Uncertainty Principle forbids the simultaneous determination of both range and speed information with complete precision. To deal with this constraint, one devises active signals that can yield the desired information on range or speed. In our situation, the detector is built upon the basis chosen

to represent the vector space (this is explained in Chapter IV), and different bases yield different information. Wavelet bases, in general, are characterized by their ability to yield both range and directional information, albeit the Uncertainty Principle forces the information to be imprecise.

We create several types of sonar signals and demonstrate their characteristics, especially whether they yield range or direction information. These characteristics are shown by a surface plot called a Doppler Ambiguity display. Such plots (see the figures at the end of Chapter V) show how "different" a signal is when it is shifted in time (thus yielding range information) or in frequency (thus yielding Doppler shift, or direction, information).

One of the early directions of this research was to use wavelets to generate active signals with desirable characteristics. Subsequent research indicated that wavelets would provide no significant advance in signal design. Nonetheless, we devised a method to use any signal to generate wavelet bases for detection purposes. This is described in Chapter III.

4. Chapter Summary

We start with a brief mathematical and historical background in the following chapter. Chapter III gives our main mathematical results in discrete wavelet theory. This chapter, as well as this whole report, will emphasize the results and will delve into the mathematics only to give the motivation for the procedures. Chapter IV discusses the detection algorithm and includes quantitative results of the efficacy of certain discrete wavelet bases. Standard sonar signals, along with their characteristics, are described in Chapter V. Chapter VI discusses the transmission simulation model. Chapter VII includes an explicit example of its use in conjunction with various detector bases as well as with the multi-channel detection method. Chapter VII consists of the results of the experiments and tests described in Chapter VI. We end with a discussion of possible future research directions in Chapter VIII.

CHAPTER II

BACKGROUND AND NOTATIONS

This chapter provides the motivation and notation used throughout the rest of this report. In Section 1, we trace the evolution of a signal, from reception through the analyzer right up to the detector. Section 2 discusses – in more detail – the mathematics of discrete signal processing. The details are essential for the notations and definitions used in other sections of the report. Section 3 presents a brief overview of the historical results in classical harmonic analysis, which led to the development of modern-day signal processing. We end this chapter, in Section 4, with a brief historical introduction to wavelets and its relation to signal processing.

1. Signal Analysis

A signal is a real-valued function of one variable, usually the time variable. For most purposes we do not have to assume this function is smooth or even continuous, but we will assume the signal has finite energy. Thus, we consider the signal as a function $s(t) \in L^2(\mathbf{R})$ (the function space, $L^2(\mathbf{R})$, is a *Hilbert space*) that is, we require

$$\int_{-\infty}^{\infty} |s(t)|^2 dt < \infty.$$

As briefly discussed in Chapter I, this signal is our "incoming" signal; it is what the receiver picks up at all times. In this case, the finite energy requirement is only an approximation, since at all times there is some nontrivial ambient noise. This noise is frequently above some threshold so that the integral over all time would indeed be infinite.

Modern signal analysis is almost exclusively conducted with digital computers. This means the first step for the signal after reception will be discretization. For this process, a "sampler" picks off the amplitude of the signal at discrete intervals. We are not concerned with the hardware aspects of this process the end result is a discrete-time signal, represented by an infinite sequence, $s = s[n] = (\dots, s(-2), s(-1), s(0), s(1), s(2), \dots)$. (We denote the vector, s , in the standard basis by $s[n]$ and $s(n)$ to denote the n^{th} coordinate of $s[n]$.)

One can just as well consider this infinite sequence as a real-valued function of one discrete variable. In the continuous case, the variable is a real variable. In the discrete case, the variable is

an integer variable. Thus, the signal is now considered as a function, $s[n] \in l^2(\mathbf{Z})$. The relation between the continuous and the discrete version of the signal is given by

$$s[n] = s[nT_{\text{samp}}], n \in \mathbf{Z}.$$

The sampling period is T_{samp} . Its inverse, $\nu_{\text{samp}} = 1/T_{\text{samp}}$, is the sampling frequency. One often fixes the sampling frequency, as required by the Nyquist Sampling Theorem, to be greater than twice the highest expected frequency, which can be determined by the frequency spectrum of the signal. In signal processing parlance, $s[n]$ is called the *discrete-time signal*.

The discrete-time signal is now ready to be analyzed. Analysis involves sending the discrete-time signal through a filter¹. The type of filters we employ are *finite impulse response filters*. Finite impulse response filters, or FIR filters, use only a finite sequence. An example of a FIR filter is the Discrete Fourier Transform (DFT). We require finite sequences because we do use DFTs in our computations and because the detector cannot process an infinite stream of data in real time; thus, storage problems arise as the detector bottlenecks the whole process.

The process of chopping an infinite sequence into a finite sequence is called *windowing*. This entails taking a windowing function, $w[n] \in l^2(\mathbf{Z})$, to "mask" a section of the discrete-time signal. A *windowing function*, or *window*, is any function that is nonzero in a finite interval. That is,

$$w(n) = \begin{cases} \neq 0 & \text{for } n = 0, 1, \dots, N-1 \\ = 0 & \text{for all other } n \in \mathbf{Z} \end{cases}.$$

We assume $w(n) > 0$ for $n = 0, 1, \dots, N-1$. The integer, N , is called the *window size*. In this report, N will always denote the window size. Also, the window size is often set to be a power of 2, that is, $N = 2^L$, for algorithmic speed considerations. Again, N is usually chosen larger than the sampling frequency, because the discrete frequency for this window size is bounded above by $\frac{N}{2}$, thus minimizing information loss. In the research conducted for this report, we chose the rectangular windowing function,

$$w(n) = \begin{cases} 1 & \text{for } n = 0, 1, \dots, N-1 \\ 0 & \text{otherwise} \end{cases}.$$

¹ A *filter* is a generic term for an analyzing processor – a black box, so to speak. Its root comes from the early processors which literally did filter out the high or the low frequencies.

We chose this primarily for convenience. To make the discrete-time signal finite, one computes the product to get the windowed signal, $s_w[n]$, where $s_w(n) = w(n) s(n)$ for all n . If the window is the rectangular, then there is no need to compute N multiplications. All we have to do is set $s_w(n) = s(n)$ for $n = 0, \dots, N - 1$ and set $s_w(n) = 0$ otherwise. Since $s_w(n) = 0$ for $n \neq 0, \dots, N - 1$, we consider this windowed signal as a finite sequence, which we also label as $s[n]$, abusing the notation somewhat. We will only consider finite sequences for our signals. Such signals are called *discrete signals*. A source for discrete signal processing is Reference [b].

2. Some Mathematics of Discrete Signal Processing

The discrete signal, $s[n]$, can be considered in a number of ways. One way is to consider $s[n]$ as a real-valued function of one integer (modulo N) variable. That is, $s[n] \in l^2(\mathbf{Z}_N)$, where \mathbf{Z}_N denotes the integers modulo N . Another way to interpret the finite sequence $s[n]$ is as an N -dimensional vector. In this case, we also generalize a bit by viewing $s[n]$ as a complex-valued vector. This generalization facilitates using the Fourier transform, which is complex-valued. Indeed, we could have started at the very beginning and considered the signal $s(t)$ as a complex-valued function from the start. We choose to view $s[n]$ as a vector because we can use linear algebra techniques to understand the problems. However, there are nonlinear facets involved with discrete signal processing. In those instances, we view $s[n]$ as a complex-valued function on the integers $0, 1, \dots, N - 1$.

Now that we have established $s[n]$ as a vector in complex N -dimensional vector space, denoted by $\mathcal{V} = \mathcal{V}_0$, we have to determine the signal processing equivalents to all the standard linear algebra objects, like bases, matrices, linear operators, and so on.

Finite-dimensional vector spaces are best viewed independent of a basis. In this regard, a signal (i.e., vector) \mathbf{s} no longer has the implication of a function of time. In our notation, $\mathbf{s} \in \mathcal{V}_0$ is the signal in a basis-free notation. The standard basis for the vector space is deemed the delta, or time, basis. We write $s[n] \in \mathcal{V}_0$ to represent the signal in the standard basis. Since all signals in time are real, the coordinates of $s[n]$ are all real-valued. That is, $s[n] = (s(0), s(1), s(2), \dots, s(N - 1))$, where $s(k) \in \mathbf{R}$ for all $k = 0, 1, 2, \dots, N - 1$.

Another important basis for the vector space is the Fourier basis. The signal in the Fourier basis is denoted by $\hat{s}[n]$. The relation between the Fourier basis and the standard basis is given by the Fourier and inverse Fourier transforms:

$$\hat{s}(n) = \sum_{m=0}^{N-1} s(m) e^{-2\pi i mn/N}$$

and

$$s(n) = \frac{1}{N} \sum_{m=0}^{N-1} \hat{s}(m) e^{2\pi i mn/N}.$$

An important non-linear algebra operation on \mathcal{V}_0 is the convolution of two signals. For $s[n]$ and $t[n]$ in \mathcal{V}_0 , define the convolution, $(s*t)[n]$, by

$$(s*t)(n) = \sum_{k=0}^{N-1} s(k) t(n-k),$$

where the index is computed modulo N . The main convolution result is the convolution theorem:

Theorem 1: $(\widehat{u*v})(n) = \hat{u}(n) \hat{v}(n)$, $n = 0, 1, \dots, N-1$.

See Reference [b] for a proof. The multiplication of the Fourier transforms, $\hat{u}[n]$ and $\hat{v}[n]$, is coordinate-wise, which we call the *outer product* of the two vectors. We repeat that neither convolution nor the outer product is a linear operation.

Additional linear algebra facts are given in Reference [c]. We now summarize the important linear operators used in the following chapters. Linear operators are the linear algebra analogue of linear systems in signal processing. Special types of linear systems, such as linear time-invariant systems, are just special types of linear operators. Some systems in signal processing are not linear. These correspond to nonlinear operators, and in this case, we no longer view $s[n]$ as a vector; we view it as a function whose domain consists of N numbers.

Our interpretation of linear operators here differs from standard linear algebra definitions in one very crucial aspect. This main difference is that our operators are given in matrix form (no difference here with most linear algebra interpretations), but *independent* of basis. In this respect, our linear operators are not technically linear operators in the linear algebra sense; that is, we name the operator by what it does to a vector (expressed in *any* basis) not by what it does to a vector (expressed with respect to a *given* basis). This is a very important difference. The reason for the difference is that their algorithmic implementation requires us to do so.

The first linear operator is the *rotation by k* operator. This operator is denoted by R^k . It takes a vector (expressed in whatever basis) and translates the indices by k . Specifically,

$$(R^k s)(n) = s(n - k).$$

We assume here that the basis is the standard basis, which is where this operator is most often used. Signal processing engineers usually call this operator the *delay* (by k) operator. We also call this operator the *translation* (by k) operator. Note that translation by N is the identity operator.

Two other operators coming from signal processing are the *upsampling* and *downsampling* operators. They are denoted by U and D , respectively, and are defined as follows:

$$(U s)(n) = \begin{cases} s(\frac{N}{2}) & \text{if } n \text{ is even} \\ 0 & \text{if } n \text{ is odd} \end{cases}, n = 0, 1, 2, \dots, 2N - 1,$$

and

$$(D s)(n) = s(2n), n = 0, 1, 2, \dots, \frac{N}{2} - 1.$$

Note that the length of the vector doubles when upsampled and halves when downsampled. Again, the vector is expressed here in the delta basis, but the upsampling and downsampling operators work the same way with respect to any basis. Because these operators take vectors from one vector space to a different vector space, one must be very careful when defining the bases in the respective spaces.

The Fourier transform of the above two operators results in the *spreading* and *folding* operators. These are denoted by S and F , respectively, and are defined as follows:

$$(S v)(n) = \begin{cases} v(n) & \text{for } n \in \{0, 1, \dots, N-1\} \\ v(n-N) & \text{for } n \in \{N, N+1, \dots, 2N-1\}, \end{cases}$$

and

$$(F v)(n) = v(n) + v(n+N), n \in \{0, 1, \dots, N-1\}.$$

Reference [c] details the relationships between the upsampling and the spreading operators and between the downsampling and the folding operators. We will assume knowledge of these relationships in the following chapters.

3. Harmonic Analysis

The decomposition of functions into sines and cosines as described by J. Fourier at the end of the 19th century introduced the field of harmonic analysis, abstractly culminating with the current study of Hilbert spaces. On the practical side, there are a number of reasons for decomposing a function – or in our case, a signal – into trigonometric components. A few of them are:

1. Frequency Analysis. One would like to know the tonals making up the signal.
2. Noise discrimination. With *a priori* knowledge of the signal's frequency range, one may zero out all contributions from outside the range, since they are essentially noise.
3. Data storage and retrieval. A pure tonal has infinite support in the time domain. However, its Fourier transform has compact support. Thus, storage is simpler in the Fourier domain.

The Fourier transform is given by the formula (the smooth analogue to the above discrete Fourier transform),

$$\hat{f}(\omega) = \int_{-\infty}^{\infty} f(t) e^{-i\omega t} dt,$$

although the integral is sometimes normalized by scaling with $\frac{1}{\sqrt{2\pi}}$. The inverse transform is given by

$$f(t) = \frac{1}{2\pi} \int_{-\infty}^{\infty} \hat{f}(\omega) e^{i\omega t} d\omega,$$

where the scaling constant applies when the above Fourier transform is used. This is the continuous analogue to the discrete Fourier transform given in Section 2.

Current applications-related work in harmonic analysis include time-frequency (T-F) distributions. T-F Distributions are surface plots of a signal, given in two variables corresponding to time and frequency. The time-dependent Fourier transform, or the windowed Fourier spectrogram, is one example of a time-frequency distribution. Another well-known time-frequency distribution is the Wigner-Ville distribution. We show some examples of these T-F distributions in Chapter V.

In our research, we have also developed a wavelet-based T-F distribution. This distribution does not perform as well as the windowed Fourier spectrogram, but it is much faster, since it does not require multiple uses of the Fourier transform over a number of windows. Reference [d] gives a thorough treatment of the various T-F distributions.

Our application of harmonic analysis comes in Chapter V, which deals with signal generation. Another analyzing device we use is the Doppler Ambiguity Display. This is also a surface plot, much like the T-F distributions. The Doppler Ambiguity Display is not, however, a distribution plot. It measures how "different" a signal is after it is shifted in time or frequency (by Doppler), compared to its unshifted self. The difference is measured by computing an integral of an inner product. A more complete explanation is given in Chapter V, as well as in Reference [c].

4. Wavelet Theory

One reason for the creation of T-F distributions is to study nonstationary signals. Stationary signals are those with a fixed frequency spectrum over all time. It is clear that most signals (acoustic signals, in particular) are nonstationary. In fact, many signals are transient. Finding the frequency spectrum of a nonstationary signal, then, no longer has its original meaning. Thus, one looks at the windowed Fourier spectrogram, which assumes the signal is stationary (i.e., has a fixed spectrum) over a small period of time. This process attempts to localize (in time) the frequency distribution, because the Fourier transform (i.e., the Fourier basis) has no time localization.

What is needed, then, is a basis which has time localization. Of course, the delta, or time, basis provides perfect time localization. However, the delta basis has no frequency localization. This means the delta basis offers no information on the frequency spectrum of the signal, which is essential if one were to try to quantitatively distinguish between similar looking, but different, signals. For example, compare a linear frequency-modulated signal to a hyperbolic frequency-modulated signal; the two look similar in time, but very different in frequency (see Chapter V for illustrations).

The reason for these constraints is, again, the Uncertainty Principle. The Uncertainty Principle is quantitatively given by the inequality,

$$\sigma_v^2 \sigma_t^2 \geq \pi/4,$$

where, assuming a normalized signal, σ_v^2 is the variance in the frequency v and σ_t^2 is the variance in the time t . Since $\sigma_v^2 = 0$ in the Fourier transform of a signal and $\sigma_t^2 = 0$ in the time series representation of a signal, the complementary variances must be infinite.

Thus, the inadequacies of both the time domain and the Fourier (frequency) domain for signal processing led researchers to consider domains (i.e., alternative bases for $L^2(\mathbf{R})$) that capture a bit of both. The Uncertainty Principle, people recognize, limits any domain from precisely determining both time and frequency information. In this regard, there is no optimal domain in which to perform signal analysis.

Results in this area led to the study of wavelet theory. Initial works by Gabor based on works of Wigner (Reference [e]), and many others considered a set of functions in time consisting of dilations and translations of a single scaling function. The translates would operate in the same vein as translates of a delta basis function (i.e., the delta function): give temporal information. The dilations correspond to translations in the Fourier domain, thus yielding frequency information. This set of functions – provided the functions together satisfy some orthonormality and admissibility conditions – forms a *wavelet* basis for the Hilbert space.

Many researchers in wavelet theory currently follow the Multiresolution Analysis construction developed by Mallat and furthered by Daubechies, Mallat, Meyer, and many others, see References [f], [g], and [h]. Here, the Hilbert space $L^2(\mathbf{R})$ is decomposed into a nested sequence of closed subspaces:

$$\cdots V_{-2} \subset V_{-1} \subset V_0 \subset V_1 \subset V_2 \subset \cdots \subset L^2(\mathbf{R})$$

such that:

$$\{0\} = \bigcap V_k = \lim_{k \rightarrow -\infty} V_k$$

and

$$L^2(\mathbf{R}) = \overline{\bigcup V_k} = \overline{\lim_{k \rightarrow \infty} V_k},$$

where the overline denotes closure (in the sense of Cauchy sequences). From this, there exists a unique scaling function $\phi_0(x) \in V_0$ such that for $\phi_k(x) = \sqrt{\frac{1}{2^k}} \phi_0(2^k x)$, $k \in \mathbf{Z}$, the set $\{\phi_k(x - 2^{-k}m) \mid m \in \mathbf{Z}\}$ spans V_k for all k .

Define complementary subspaces $W_k = V_k^\perp \subset V_{k+1}$, $k \in \mathbf{Z}$, so that $W_k \oplus V_k = V_{k+1}$. Then, the W_k 's are mutually orthogonal, and the direct sum of them all spans $L^2(\mathbf{R})$. Each orthogonal subspace W_k is in turn spanned by a complementary set of functions, $\{\psi_k(x - 2^{-k}m) \mid m \in \mathbf{Z}\}$. These functions are called wavelets. The ψ_k 's are constructed to complement the ϕ_k 's. See References [f], [g], and [i] for detailed expositions of the Multiresolution Analysis.

Our approach to and use of wavelet theory will be slightly different. We go into more detail in the next chapter.

CHAPTER III

DISCRETE WAVELET THEORY

In this chapter, we cover the main theoretical results of discrete wavelet theory. We begin in Section 1 with a brief overview of discrete wavelet bases and how they are constructed. This description includes the filter bank design to implement the wavelet transform. In Section 2, we study the construction of the l^2 -closest wavelet and its corresponding wavelet basis. Examples in Chapter V show the utility of this wavelet basis for detection. We end with Section 3, giving another application of the l^2 -closest wavelet basis: computing the ψ -binary decomposition of a signal. This decomposition seems to be useful in detecting translates of a given signal. There are examples of its use in Chapters V and VII.

1.1. Discrete Wavelet Basis

The term "wavelets" generically refers to a set of functions satisfying certain properties. These properties are detailed, for the continuous case, in References [f], [g], and many others. Some of these properties for the continuous case do not carry over to the discrete case. We are concerned specifically with the discrete case. Nonetheless, the basic premises do carry over, namely that the set of functions forms an orthonormal basis and that translates and dilates of the functions look "alike."

The principal difference between our discrete wavelet functions and the discrete wavelet functions from some of the literature (see References [f], [j], [g]) is that our discrete wavelet functions are actually discrete functions whereas others' discrete wavelet functions are just continuous functions that have been discretely sampled. The difference is that we can guarantee normality while the others' wavelets have to be renormalized. Furthermore, our version allows for direct application of linear algebra and is easier to implement, compared to the other types. The drawback is the lack of resolving power. The discretely sampled continuous wavelet functions can resolve to any magnification. Our discrete wavelet basis can resolve to a resolution power of, at most, $\log_2 N$ (which is 10 for $N = 1024$).

Some of the wavelet functions are illustrated at the end of this subsection. Of note is the Daubechies D_4 wavelet basis. We took the algorithm given in Reference [g] and created a "compactly supported," orthonormal wavelet basis. The wavelet basis functions are compactly supported in the continuous sense: as functions in one real variable. In our case, all our wavelet

basis functions are always compactly supported, since they are functions in one integer (modulo N) variable. From the pictures, Figures III-1, III-2, and III-3, we see that both the real Shannon wavelet basis functions and the l^2 -closest wavelet basis functions are not "compactly supported" in the intuitive sense, compared to the Daubechies' D_4 wavelet basis.

Before we continue, we need to set some notations used in the rest of this report. Recall our fixed parameters. Our window size is denoted by N , where $N = 2^L$ for some positive integer L . For $1 \leq p \leq L$, we will abbreviate $N/2^p$ by N_p . Also, we shall denote the Hilbert spaces $l^2(\mathbb{Z}_{N_p})$ by \mathcal{V}_p . This fits with our previous notation of \mathcal{V}_0 for the Hilbert space $l^2(\mathbb{Z}_N)$. The dimension of \mathcal{V}_p is N_p . We will use the words, "vector," "signal," and "function" synonymously, although "signal" alludes primarily to the vector being written in the standard basis.

Definition 1: Let $f_1(n), f_2(n), \dots, f_p(n)$, and $g_p(n) \in \mathcal{V}_0$ be $p+1$ pair-wise orthonormal vectors, expressed in the time basis. Consider the rotations of the above functions, $(R^{2^m k} f_m)(n) = f_m(n - 2^m k)$, for $k = 0, 1, \dots, N_m - 1$, and $m = 1, 2, \dots, p$, including the rotations of $g_p(n)$ by $2^p k$, $k = 0, 1, \dots, N_p - 1$. These rotations of the $p+1$ functions make up N functions in all. We say this set of N functions is an *orthonormal p -level wavelet basis* if these N functions are mutually orthonormal (and hence, span an N -dimensional space). This wavelet basis is also called a *$p+1$ st generation wavelet basis*. Note that there is no "scaling" function in the definition. See References [d], [c], and [k].

The requirement that the rotations of the $p+1$ functions be orthonormal is written as,

$$\langle R^{2^m j} f_m, R^{2^n k} f_n \rangle = \delta_{m,n} \delta_{j,k},$$

where $\delta_{x,y}$ is the Kronecker delta function. One may also replace g_p for f_p in the above formula.

ELEMENTS OF THE 3-LEVEL REAL SHANNON WAVELET BASIS CENTERED WAVELET FUNCTIONS IN TIME SERIES

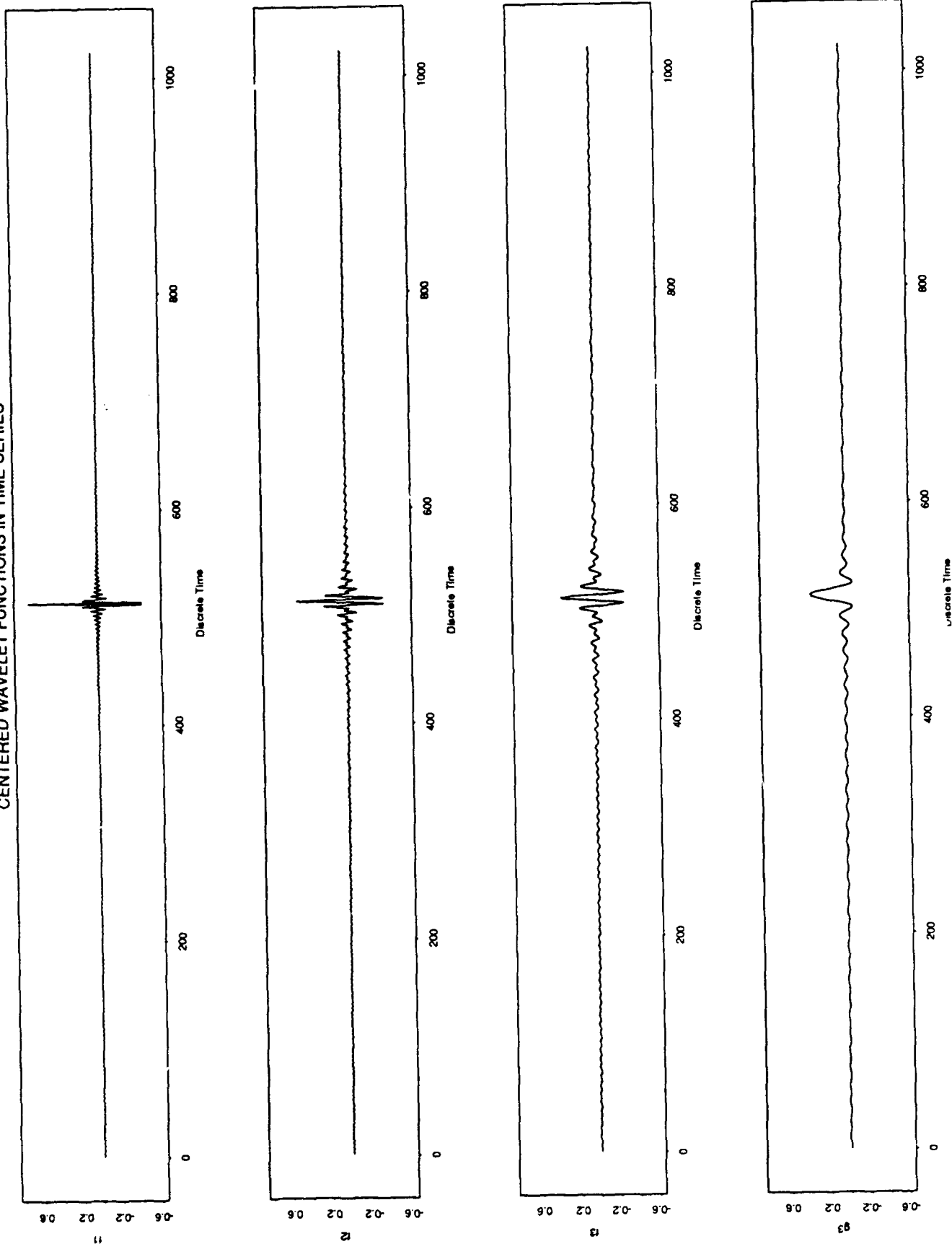


Figure III-1

ELEMENTS OF THE 3-LEVEL L2-CLOSEST TO CHIP2 WAVELET BASIS CENTERED WAVELET FUNCTIONS IN TIME SERIES

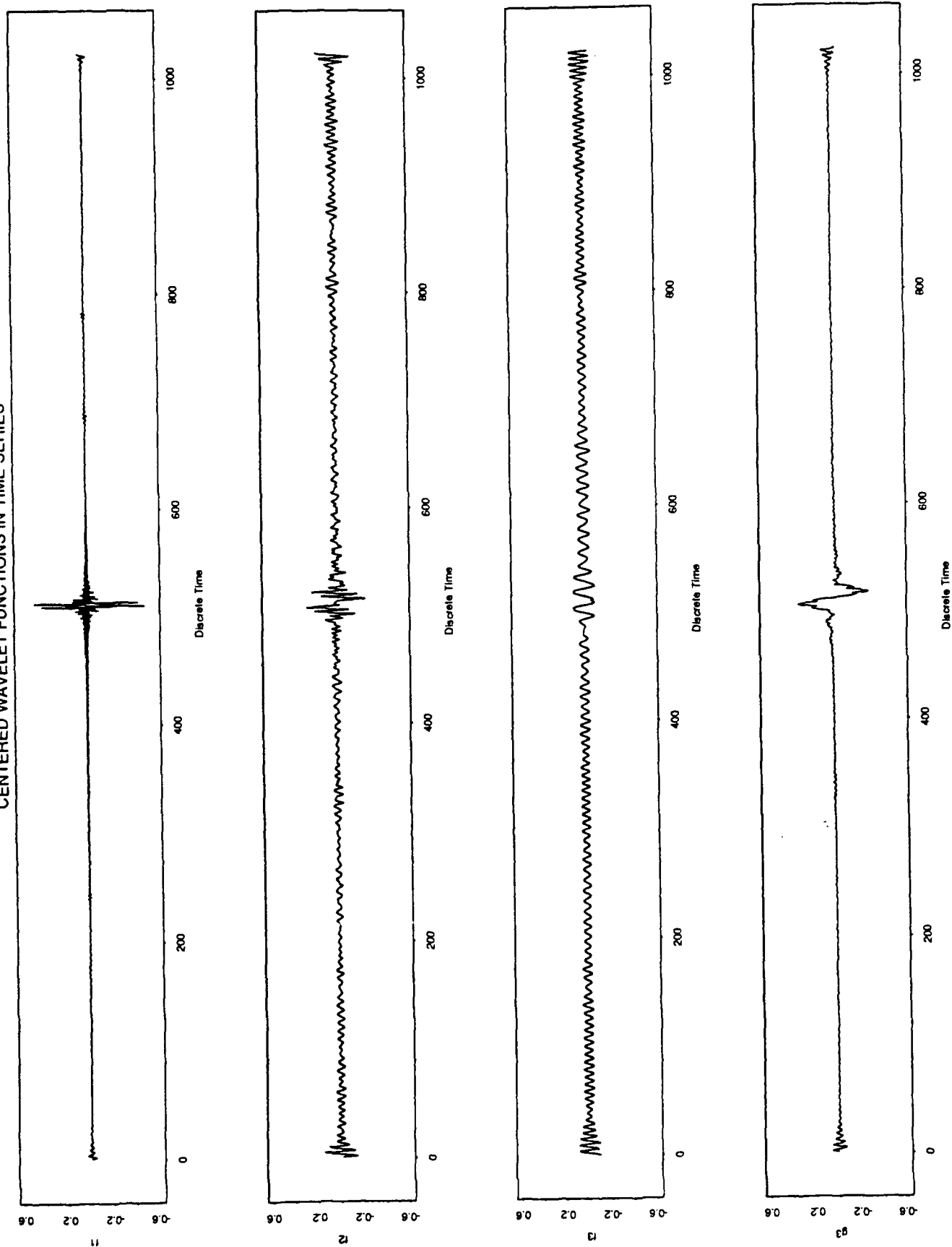


Figure III-2

ELEMENTS OF THE D4 WAVELET BASIS CENTERED WAVELET FUNCTIONS IN TIME SERIES

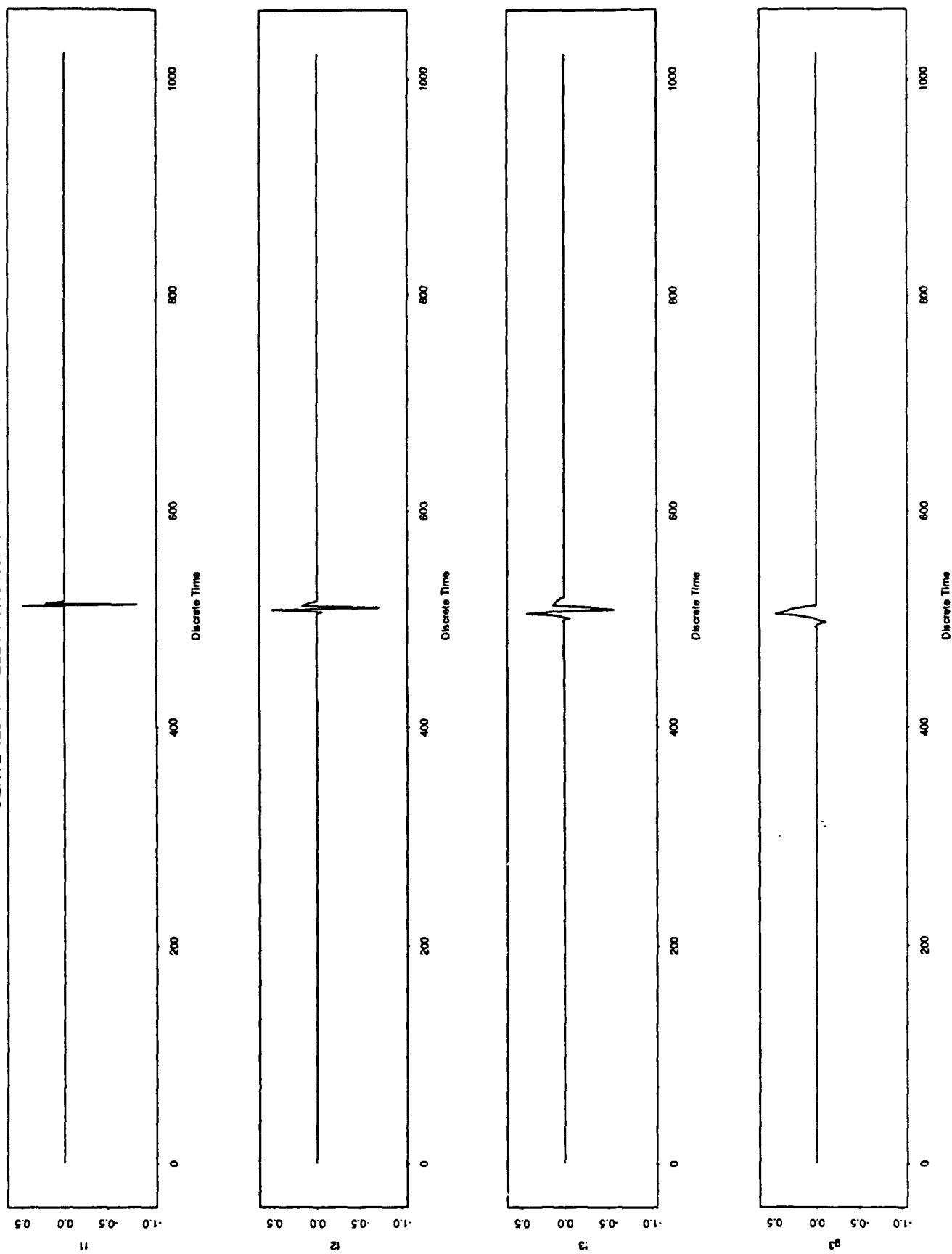


Figure III-3

So far, we have not described how to construct such a wavelet basis, or even if such a basis exists. To do so, we begin with some definitions. Recall the notation to denote a vector in the time basis: $\mathbf{f} = f[n]$. We may also use the boldface (i.e., basis-free) notation of the vector to denote the vector in the time basis.

Definition 2: A vector, $f[n] \in \mathcal{V}_{p-1}$, is said to be *p-admissible* if

$$|\hat{f}(n)|^2 + |\hat{f}(n + N_p)|^2 \equiv 2 \text{ for all } n \in \mathbb{Z}_{N_p}.$$

Definition 3: A pair of functions, $f[n]$ and $g[n] \in \mathcal{V}_{p-1}$, is *p-satisfactory* if the matrix

$$\frac{1}{\sqrt{2}} \begin{pmatrix} \hat{f}(n) & \hat{g}(n) \\ \hat{f}(n + N_p) & \hat{g}(n + N_p) \end{pmatrix}$$

is unitary for all $n \in \mathbb{Z}_{N_p}$. Note that each function of a p-satisfactory pair, $(f[n], g[n])$, is p-admissible. Compare this definition of p-satisfactory to Equation (66) in Reference [g] and Equation 3.22 in Reference [f].

The following theorem gives a constructive method for making an orthonormal wavelet basis.

Theorem 1: Suppose $\psi_1, \phi_1 \in \mathcal{V}_0$. Fix a p, $1 < p \leq L$, and define $\psi_k, \phi_k \in \mathcal{V}_{k-1}$ by $\hat{\psi}_k = D^{k-1} \hat{\psi}_1$ and $\hat{\phi}_k = D^{k-1} \hat{\phi}_1$, for $k = 2, 3, \dots, p$. Let $\mathbf{f}_1 = \phi_1$, and for $k = 2, 3, \dots, p$ let

$$\mathbf{f}_k = \psi_1 * U \psi_2^* \dots * U^{k-2} \psi_{k-1} * U^{k-1} \phi_k$$

and

$$\mathbf{g}_p = \psi_1 * U \psi_2^* \dots * U^{p-2} \psi_{p-1} * U^{p-1} \psi_p.$$

Then the collection of functions

$$\{\mathbf{R}^{2k} \mathbf{f}_1\}_{k=0}^{N_1-1}, \{\mathbf{R}^{4k} \mathbf{f}_2\}_{k=0}^{N_2-1}, \dots, \{\mathbf{R}^{2^p k} \mathbf{f}_p\}_{k=0}^{N_p-1}, \{\mathbf{R}^{2^p k} \mathbf{g}_p\}_{k=0}^{N_p-1}$$

is an orthonormal p-level wavelet basis for \mathcal{V}_0 if and only if $\psi_1, \phi_1 \in \mathcal{V}_0$ form a 1-satisfactory pair.

The rotations of g_p are called the "extra" p^{th} -level wavelet basis elements. It is also the $p+1^{\text{st}}$ generation of the wavelet basis. The functions, $\psi_1, \phi_1 \in \mathcal{V}_0$, are called the *mother* and *father* wavelet functions.

Example 1: Haar wavelet basis.

$$\text{Let } \phi_1(n) = \begin{cases} \frac{1}{\sqrt{2}} & \text{for } n = 0 \\ \frac{-1}{\sqrt{2}} & \text{for } n = 1 \\ 0 & \text{for } n > 1 \end{cases} \text{ and } \psi_1(n) = \begin{cases} \frac{1}{\sqrt{2}} & \text{for } n = 0 \\ \frac{1}{\sqrt{2}} & \text{for } n = 1 \\ 0 & \text{for } n > 1 \end{cases}.$$

Then, (ϕ_1, ψ_1) is a 1-satisfactory pair. Following the construction given in the above theorem, we get functions $f_1, f_2, \dots, f_p, g_p \in \mathcal{V}_0$, which, together with their appropriate rotations, form an orthonormal basis, called the p -level *Haar basis*. By following the computations used in Theorem 1, one may check that

$$f_2 = .5 (1, 1, -1, -1, 0, 0, 0, \dots, 0),$$

$$f_3 = \frac{1}{\sqrt{8}}(1, 1, 1, 1, -1, -1, -1, -1, 0, 0, \dots, 0),$$

and so on.

Example 2: Real Shannon Basis.

Define the mother and father wavelet functions, ϕ_1 and $\psi_1 \in \mathcal{V}_0$ by

$$\hat{\psi}_1(m) = \begin{cases} \sqrt{2} & \text{if } 0 \leq m \leq N_2 - 1 \text{ or } 3N_2 + 1 \leq m \leq N - 1 \\ i & \text{if } m = N_2 \\ -i & \text{if } m = 3N_2 \\ 0 & \text{if } N_2 + 1 \leq m \leq 3N_2 - 1 \end{cases},$$

and

$$\hat{\phi}_1(m) = \begin{cases} 0 & \text{if } 0 \leq m \leq N_2 - 1 \text{ or } 3N_2 + 1 \leq m \leq N - 1 \\ 1 & \text{if } m = N_2 \text{ or } m = 3N_2 \\ \sqrt{2} & \text{if } N_2 + 1 \leq m \leq 3N_2 - 1 \end{cases},$$

so that, in the time basis, they are real-valued and the pair is 1-satisfactory. Follow the construction in Theorem 1 to get the wavelet functions, $f_1, f_2, f_3, \dots, f_p, g_p$, where $\hat{f}_1 = \hat{\phi}_1$ and

$$\hat{f}_k(m) = \begin{cases} 2^{k/2} & \text{for } N_{k+1} + 1 \leq m \leq N_k - 1 \\ & \text{or } N - N_k + 1 \leq m \leq N - N_{k+1} - 1 \\ 2^{(k-1)/2} & \text{for } m = N_{k+1} \text{ or } m = N - N_{k+1} \\ i2^{(k-1)/2} & \text{for } m = N_k \\ -i2^{(k-1)/2} & \text{for } m = N - N_k \\ 0 & \text{otherwise} \end{cases}, k = 2, 3, \dots, p$$

and

$$\hat{g}_p(m) = \begin{cases} 2^{p/2} & \text{for } 0 \leq m \leq N_{p+1} + 1 \\ & \text{or } N - N_{p+1} + 1 \leq m \leq N - 1 \\ i2^{(p-1)/2} & \text{for } m = N_{p+1} \\ -i2^{(p-1)/2} & \text{for } m = N - N_{p+1} \\ 0 & \text{otherwise} \end{cases}.$$

Note that the supports of the various level wavelet functions in the Fourier basis do not intersect at more than two points, thus displaying the strong frequency localization of the real Shannon wavelets. (The original construction created a high-pass function w and a low-pass function v . Our construction creates high-pass and low-pass functions for different levels.) The real Shannon wavelets are also spatially localized. See References [c] and [I] for more details of the real Shannon wavelet basis. See Figure III-1.

Example 3: Daubechies' D_4 Wavelet Basis

This wavelet basis is generated by a different method, compared to the above two examples (and the l^2 -class wavelet basis). We do not actually construct the wavelet basis; instead, we create the wavelet transform so that we can take the wavelet transform of any signal function. This process involves constructing two sparse matrices, denoted by L and H (for Low and High, respectively). The sparseness of the matrices makes the computation very quick. This is why the algorithm has a computation time of $O(N)$, even quicker than the Fast Fourier Transform.

The matrices are made up of four different numbers, c_0, c_1, c_2 , and c_3 . These are exactly the coefficients, $h_N(n)$, as given in Table 1 of Reference [g], for $N = 2$ (the N in the table). Table 1 of Reference [g] only gives an approximate value. For $N < 7$, these coefficients, $h_N(n)$, are computable (they are algebraic numbers). For our case, they are

$$c_i = \frac{1}{\sqrt{2}} \begin{cases} \frac{(1 + \sqrt{3})}{4} & \text{if } i = 0 \\ \frac{(3 + \sqrt{3})}{4} & \text{if } i = 1 \\ \frac{(3 - \sqrt{3})}{4} & \text{if } i = 2 \\ \frac{(1 - \sqrt{3})}{4} & \text{if } i = 3 \\ 0 & \text{if } i > 3 \end{cases}$$

We then create the matrices from these coefficients. Define

$$L_k = \begin{pmatrix} c_{2i-j} \end{pmatrix}_{\substack{1 \leq i \leq N_k \\ 1 \leq j \leq N_{k-1}}} \quad \text{and} \quad H_k = \begin{pmatrix} (-1)^{j+1} c_{j+1-2i} \end{pmatrix}_{\substack{1 \leq i \leq N_k \\ 1 \leq j \leq N_{k-1}}}$$

Also define $L_k^* = \text{Transpose}(L_k)$ and $H_k^* = \text{Transpose}(H_k)$. These matrices are defined for $k = 1, 2, \dots, p$, where p is the level of the wavelet basis. Now, let $\mathbf{a}^p = \mathbf{f}$, the signal (in time basis). For $m = p, p-1, \dots, 2, 1$, define

$$\mathbf{a}^{m-1} = L_{p-m+1} \mathbf{a}^m \quad \text{and} \quad \mathbf{b}^m = H_{p-m+1} \mathbf{a}^m.$$

Then,

\mathbf{b}^{p-1} contains the first $\frac{N}{2}$ wavelet coefficients.

\mathbf{b}^{p-2} contains the next $\frac{N}{2^2}$ wavelet coefficients.

⋮

\mathbf{b}^0 contains the next $\frac{N}{2^p}$ wavelet coefficients, and

\mathbf{a}^0 contains the last $\frac{N}{2^p}$ wavelet coefficients.

To reconstruct the signal, iterate backwards. Set

$$\mathbf{a}^m = \mathbf{L}_{p-m+1}^* \mathbf{a}^{m-1} + \mathbf{H}_{p-m+1}^* \mathbf{b}^{m-1},$$

for $m = 1, 2, \dots, p$. Then, $\mathbf{a}^p = \mathbf{f}$ as desired.

The filter bank design for this wavelet transform is shown in Figure III-4. It is a simpler design than the other wavelet filter banks, since it only involves matrix multiplication with a sparse matrix. The sparseness allows for a fast matrix multiplying algorithm.

1.2. Constructing Wavelet Bases

The construction of a wavelet basis, as given in the above theorem, has many iterative steps. This suggests a possible filter bank design to implement this wavelet transform. Indeed, we have developed two versions; one runs in the time domain (see Figure III-5), and the other runs in the Fourier domain (see Figure III-6). The Fourier domain version runs substantially faster than the time domain version, due mainly to fewer convolutions being needed. The figures depict a 2-level wavelet basis transform.

Figure III-4
Daubechies' D_4 Wavelet Filter Bank Design

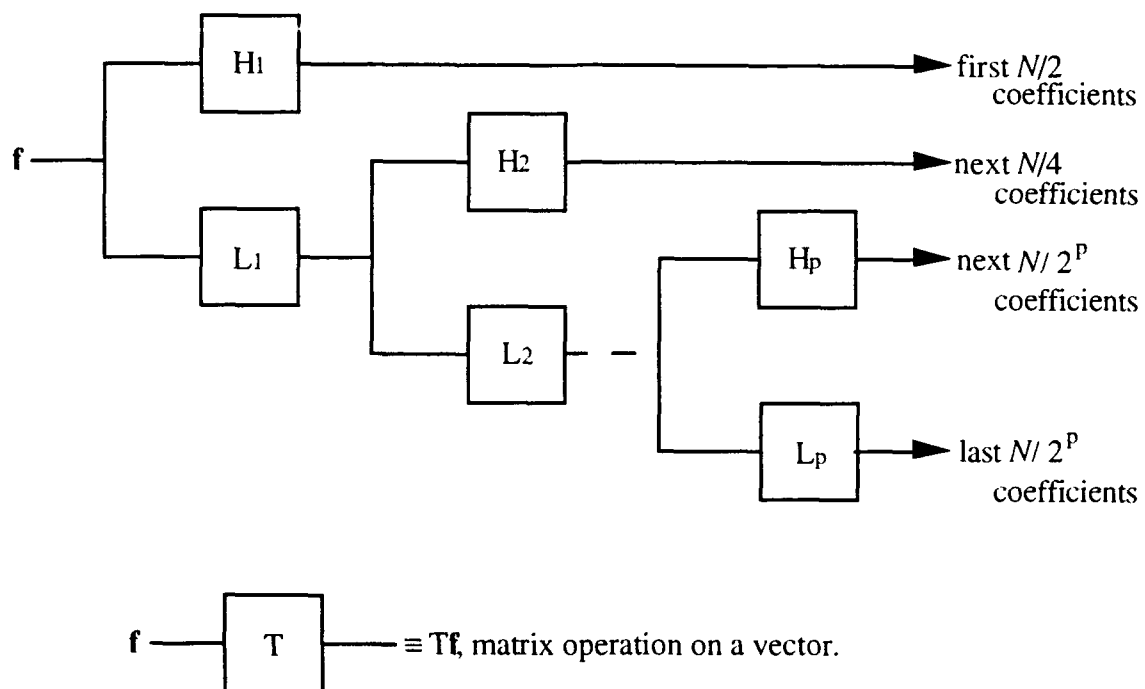
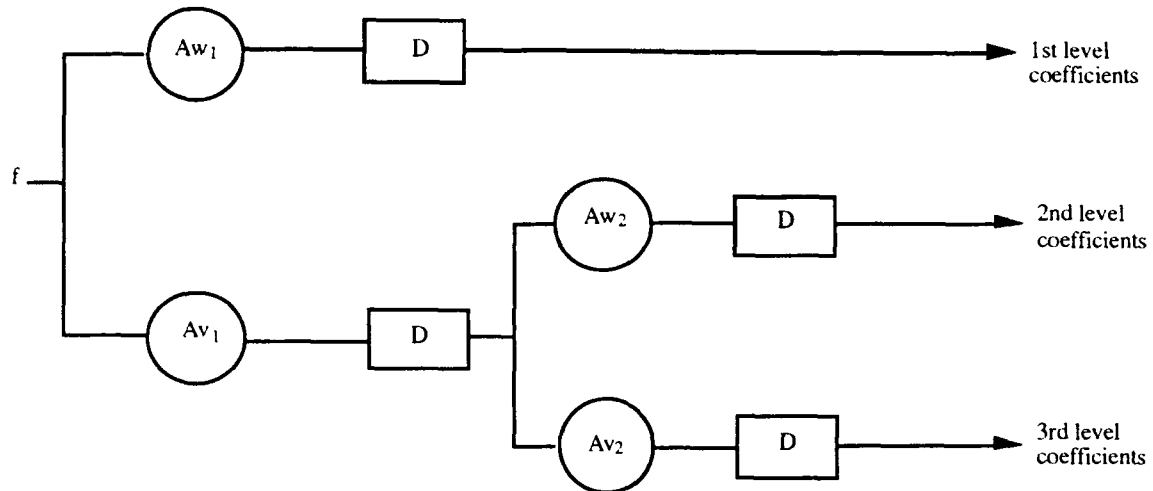


Figure III-5
Time Domain Wavelet Filter Bank Design



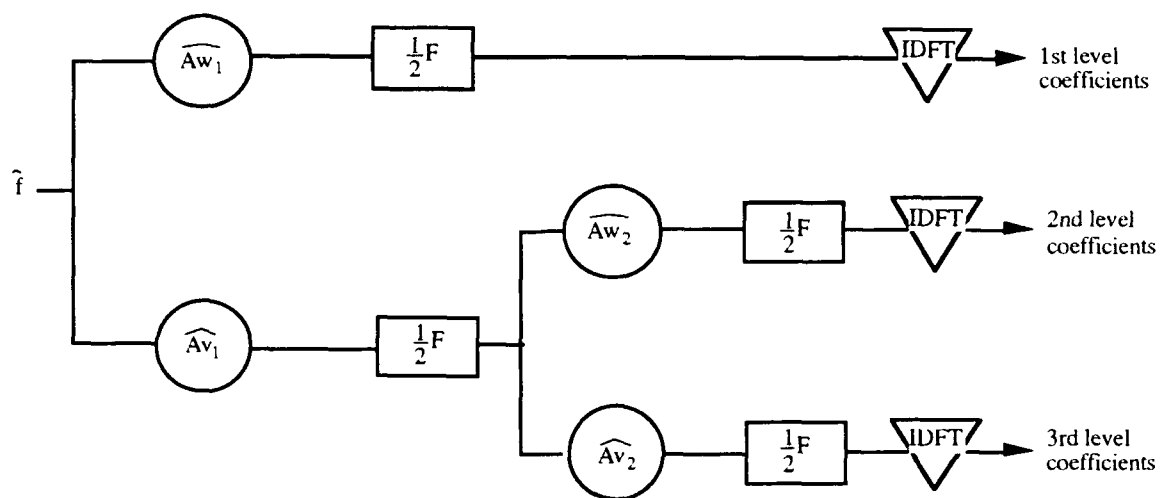
$$Av_i(n) = \overline{v_i(-n)} \quad n = 0, 1, \dots, N-1$$

$$\hat{v}_i = D^{i-1} \hat{v}_1$$

$$x \text{ --- } \bigcirc \text{ y} \equiv x * y \text{ "circular convolution"}$$

$$g \text{ --- } \boxed{D} \equiv Dg \text{ "downsampling"}$$

Figure III-6
Fourier Domain Wavelet Filter Bank Design



$$Av_i(n) = \overline{v_i(-n)} \quad n = 0, 1, \dots, N-1$$

$$v_i = Fv_{i-1}$$

$$x \text{ --- } \bigcirc y \equiv x y$$

$$g \text{ --- } \boxed{\frac{1}{2}F} \equiv \frac{1}{2} Fg = \frac{1}{2} (g(n) + g(\frac{N}{2})) \quad n = 0, 1, \dots, \frac{N}{2} - 1$$

$$g \text{ --- } \nabla \text{IDFT} \equiv \text{Inverse DFT of } g$$

There are other ways to construct wavelet bases (although the accompanying filter banks are still the same as above). The following theorem gives another construction process. We start with a definition:

Definition 4: For a function, $f \in \mathcal{V}_0$, define $\Sigma_p f \in \mathcal{V}_p$ for $p = 1, 2, \dots, L$ by the following:

$$(\Sigma_p f)(n) = \sqrt{\frac{1}{2^p} \sum_{k=0}^{2^p-1} |\hat{f}(n + k N_p)|^2}, \quad n = 0, 1, \dots, N_p - 1.$$

We also define for $p = 0$: $\Sigma_0 f = \hat{f}$. Note the definition takes a function written with respect to the time basis, uses the Fourier transform of this function, and yields a function written in the Fourier basis. It is important to use the non-normalized version of the Discrete Fourier Transform. This vector, $\Sigma_p f$, can also be considered as a vector in \mathcal{V}_0 by periodic extension.

Theorem 2: Fix a level p , $1 \leq p \leq L$. The following are equivalent:

1. $\langle R^{2^p k} f, f \rangle = \delta_{0,k}$, $k = 0, 1, \dots, N_p - 1$. Hence $\{R^{2^p k} f\}_{k=0}^{N_p-1}$ is an orthonormal set.
2. $(\Sigma_p f)(n) \equiv 1$, for all $n = 0, 1, \dots, N_p - 1$.
3. $f = v_1 * U v_2 * U^2 v_3 * \dots * U^{p-1} v_p$ for some $v_1, v_2, v_3, \dots, v_p$ such that v_k is k -admissible for each $k = 1, 2, \dots, p$.
4. There exists a p -level wavelet basis whose p^{th} -generation wavelet functions are rotations of f .

Remarks:

- Statement 2 is the DFT of Statement 1, hence their equivalence.
- The v_k 's of Statement 3 are determined in the Fourier domain by:

$$\hat{v}_k(n) = \frac{(\Sigma_{k-1} f)(n)}{(\Sigma_k f)(n)} \text{ for each } n = 0, 1, \dots, N_k - 1.$$

- To create a $p+1$ generation wavelet basis whose $p+1^{\text{st}}$ generation wavelet functions are rotations of \mathbf{f} , we construct \mathbf{w}_k , $k = 1, 2, \dots, p$, such that $(\mathbf{v}_k, \mathbf{w}_k)$ is a k -satisfactory pair for each k . We present an algorithm for this process later. Now, follow the procedure from Theorem 1. At the end, we get \mathbf{f}_p and \mathbf{g}_p with $\mathbf{f} = \mathbf{g}_p$. To get $\mathbf{f} = \mathbf{f}_p$, just interchange the roles of \mathbf{f}_p and \mathbf{g}_p . This is possible since both functions are elements of \mathcal{V}'_p .
- Statement 3 can also be written in the Fourier basis:

$$\hat{\mathbf{f}} = \hat{\mathbf{v}}_1 \cdot S \hat{\mathbf{v}}_2 \cdot S^2 \hat{\mathbf{v}}_3 \cdot \dots \cdot S^{p-1} \hat{\mathbf{v}}_p,$$

where (\cdot) denotes the outer product.

The proof of Theorem 2 can be found in Reference [m].

1.3. Constructing k -Satisfactory Pairs

Let $\mathbf{v} \in \mathcal{V}_{k-1}$ be a k -admissible function. For our purposes, we assume \mathbf{v} is real-valued. We would like to find a $\mathbf{w} \in \mathcal{V}_{k-1}$ (also real-valued) so that (\mathbf{v}, \mathbf{w}) is a k -satisfactory pair. Assume the Fourier transform of \mathbf{v} is given by:

$$\hat{\mathbf{v}}(n) = |\hat{\mathbf{v}}(n)| e^{i\rho(n)} \text{ (By convention, take } \rho(n) = 0 \text{ when } \hat{\mathbf{v}}(n) = 0.)}$$

Then, set the Fourier transform of \mathbf{w} to have coordinates:

$$\hat{\mathbf{w}}(n) = |\hat{\mathbf{v}}(n + N_k)| e^{i\sigma(n)}.$$

That \mathbf{v} is real-valued implies:

$$\rho(0) = 0 \text{ or } \pi, \rho(N_k) = 0 \text{ or } \pi$$

and

$$\rho(n) = -\rho(N_{k-1} - n) \pmod{2\pi}.$$

Similarly, \mathbf{w} is supposed to be real-valued, so $\sigma(n)$ satisfies the same conditions. The condition for a pair (\mathbf{v}, \mathbf{w}) to be k -satisfactory requires an accompanying matrix to be unitary. By assuming the above expressions for the Fourier transforms of \mathbf{v} and \mathbf{w} , we need:

$$\rho(n) - \rho(n + N_k) = \pi + \sigma(n) - \sigma(n + N_k) \pmod{2\pi} \text{ for } n = 0, 1, \dots, N_{k-1}.$$

The choice we took was to set:

- $\sigma(0) = \rho(0)$
- $\sigma(N_k) = \rho(N_k) + \pi$
- $\sigma(n) = \rho(n) - \pi/2$ for $n = 0, 1, 2, \dots, N_k - 1$
- $\sigma(n) = \rho(n) + \pi/2$ for $n = N_k, N_k + 1, \dots, N_{k+1} - 1$,

all modulo 2π . This is the procedure we used to generate our discrete orthonormal wavelet bases.

The usefulness of wavelet transforms is enhanced, certainly, by their multitude. A particular wavelet transform can be tailored so as to effect a desirable response. This is one main advantage of the discrete wavelet transform over the Fourier transform.

2. Closest p-level Wavelet Bases

The variability of wavelet bases allows one to choose a wavelet basis such that the p^{th} -level wavelet function \mathbf{f}_p is close to a given signal $\mathbf{s} \in \mathcal{V}_0$. Specifically,

Definition 5: By Statement 2 of Theorem 2, we say a function $\mathbf{f} \in \mathcal{V}_0$ is a p^{th} -level wavelet function if $(\Sigma_p \mathbf{f})(n) \equiv 1$ for all $n = 0, 1, \dots, N_p - 1$. We can also extend the function $(\Sigma_p \mathbf{f})(n)$ periodically to be a function on $\{0, 1, \dots, N - 1\}$.

Theorem 3: Let $\mathbf{f} \in \mathcal{V}_0$. Then there exists a p^{th} -level wavelet function $\mathbf{f}_p \in \mathcal{V}_0$ closest in the l^2 -metric to \mathbf{f} among all other p^{th} -level wavelet functions. Moreover, \mathbf{f}_p is given by:

$$\hat{\mathbf{f}}_p(n) = \frac{\hat{\mathbf{f}}(n)}{(\Sigma_p \mathbf{f})(n)}.$$

Proof: The set of all p^{th} -level wavelet functions is a compact set in \mathbb{C}^N ; hence, existence is clear. Now, check that every element of this set has norm equal to 1. The function $\hat{\mathbf{f}}_p$ is in this set (one can also check that $\Sigma_p \mathbf{f}$ is a p^{th} -level wavelet function, after extending periodically to be a function on $\{0, 1, \dots, N - 1\}$) and has the same direction as $\hat{\mathbf{f}}$; hence, it is closest, by the triangle inequality.

This division by $\Sigma_p \mathbf{f}$ is what we shall call p -normalization. For $p = L$, it is the standard normalization.

The closest wavelet need not be unique. Note that for some $n \in \{0, 1, \dots, N-1\}$, $(\Sigma_p \mathbf{f})(n)$ may be zero. In this case then, $\hat{\mathbf{f}}(n)$ must also be zero; hence, $\hat{\mathbf{f}}_p(n)$ is undefined. One may assign $\hat{\mathbf{f}}_p(n)$ to take on any value so long as \mathbf{f}_p is still p -admissible. The option we took when implementing this was to set $\hat{\mathbf{f}}_p(n) = 1$ in this case. This allowed us to generate l^2 -closest p^{th} -level wavelet functions (and hence, p^{th} -level orthonormal wavelet bases) to any function $\mathbf{f} \in \mathcal{V}_0$.

A particular application of l^2 -closest wavelets construction is a wavelet basis where *all* the wavelet functions from each level are close to a given function. The impetus is still to find orthonormal bases yielding small compression loss for reproduction and detection purposes.

Theorem 4: Suppose $\mathbf{f} \in \mathcal{V}_0$ satisfies $(\Sigma_p \mathbf{f})(n) \equiv 1$. Then $(\Sigma_{p+1} \mathbf{f})(n) \equiv 1$.

The proof of this fact follows from direct computation and using the definition of the expressions. Using Theorem 4, we can create an extremely quick algorithm for generating a p -level orthonormal wavelet basis where the p^{th} -level wavelet function is closest to a given signal.

Let $\mathbf{f} \in \mathcal{V}_0$ be a real-valued signal. Set $\hat{\mathbf{f}}_p(n) = \frac{\hat{\mathbf{f}}(n)}{\Sigma_1 \mathbf{f}(n)}$, where $\Sigma_1 \mathbf{f}(n)$ has been extended periodically. Then, $\hat{\mathbf{v}}_1(n) = |\hat{\mathbf{v}}_1(n)|e^{i\rho(n)} = \hat{\mathbf{f}}_p(n)$ and $\hat{\mathbf{w}}_1(n) = |\hat{\mathbf{v}}_1(n + \frac{N}{2})|e^{i\sigma(n)}$, where, as before, $\rho(n) - \rho(n + \frac{N}{2}) = \pi + \sigma(n) - \sigma(n + \frac{N}{2}) \pmod{2\pi}$ for $n = 0, 1, \dots, N-1$. Note that $\hat{\mathbf{v}}_k \equiv 1$ for $k = 2, 3, \dots, p$. So, creating the other level wavelet functions, $\mathbf{f}_1, \mathbf{f}_2, \dots, \mathbf{f}_p$, and \mathbf{g}_p is much easier:

$$\begin{aligned}\hat{\mathbf{f}}_1 &= \hat{\mathbf{w}}_1, \\ \hat{\mathbf{f}}_2 &= \hat{\mathbf{v}}_1 \cdot S\hat{\mathbf{w}}_2, \\ \hat{\mathbf{f}}_3 &= \hat{\mathbf{v}}_1 \cdot S^2\hat{\mathbf{w}}_3, \\ &\vdots \\ \hat{\mathbf{f}}_p &= \hat{\mathbf{v}}_1 \cdot S^{p-1}\hat{\mathbf{w}}_p, \text{ and} \\ \hat{\mathbf{g}}_p &= \hat{\mathbf{v}}_1 \cdot S^{p-1}\hat{\mathbf{v}}_p = \hat{\mathbf{v}}_1.\end{aligned}$$

As in Theorem 2, we switch the definitions of $\hat{\mathbf{f}}_p$ and $\hat{\mathbf{g}}_p$ to get the desired result. The only place where choice is involved is in defining the $\hat{\mathbf{w}}_k$'s. We used a very simple formulation. For $k = 2, 3, \dots, p$, define $\hat{\mathbf{w}}_k$ by:

$$\hat{\mathbf{w}}_k(n) = \begin{cases} 1 & \text{for } n = 0 \\ -i & \text{for } 0 < n < N_k \\ -1 & \text{for } n = N_k \\ +i & \text{for } N_k < n < N_{k-1} . \end{cases}$$

We now give another construction for a 1-level orthonormal wavelet basis. This construction's main purpose is to correct for a deficiency in using the standard l^2 -closest wavelet basis for compressed detection methods (see Chapter IV-2). Our results (see Chapter VII) show that the l^2 -closest wavelet basis performs well in detecting the signal, via the compressed Neyman-Pearson detector. However, if the signal is translated by one, this same l^2 -closest wavelet basis does not detect the translate as well.

We choose a 1-satisfactory pair, (\mathbf{f}, \mathbf{g}) , such that \mathbf{f} is l^2 -closest to a given signal ψ and \mathbf{g} is l^2 -closest – among all such \mathbf{g} 's for which (\mathbf{f}, \mathbf{g}) is 1-satisfactory – to $R\psi$. This wavelet basis induces a decomposition algorithm, called the ψ -binary decomposition. Before we describe the decomposition algorithm, we first derive the pair (\mathbf{f}, \mathbf{g}) for ψ .

Let ψ be a function (in the time basis) in $\mathcal{V}_0 = l^2(\mathbb{Z}_N)$. By Theorem 3, we can find an l^2 -closest first-level wavelet function to ψ ; that is, there exists a 1-admissible function, \mathbf{f} , which is l^2 -closest to ψ among all 1-admissible functions. This 1-admissible function is then the mother wavelet \mathbf{f} , and the corresponding father wavelet \mathbf{g} is determined as follows.

Set $\hat{\mathbf{f}}(n) = \frac{\hat{\psi}(n)}{(\Sigma_1 \psi)(n)}$, $n = 0, 1, \dots, N-1$, as in Theorem 3. One can check that \mathbf{f} is a 1-admissible function. Moreover, let $\hat{\psi}(m) = a(m)e^{i\alpha(m)}$. Then

$$\hat{\mathbf{f}}(m) = \frac{\sqrt{2}a(m)}{\sqrt{a(m)^2 + a(m+N_1)^2}} e^{i\alpha(m)},$$

in the standard complex polar representation. Note that the phases of $\hat{\psi}$ and \hat{f} are the same. As before, we construct \mathbf{g} so that (\mathbf{f}, \mathbf{g}) is 1-satisfactory. It follows that the Fourier transform of the father wavelet \mathbf{g} has the form $\hat{g}(n) = \hat{f}(n + N_1)e^{i\sigma(n)}$ and that $\sigma(n)$ is given by our required relation,

$$\sigma(m) - \sigma(m + N_1) = \pi + \alpha(m) - \alpha(m + N_1) \pmod{2\pi}, \text{ for } m = 0, 1, \dots, N - 1.$$

Let $\omega = e^{i\theta}$, where $\theta = 2\pi/N$. We have seen that $(R\hat{\psi})(m) = \hat{\psi}(m)\omega^m$, where R is the rotation operator. We want to make \mathbf{g} as close to $R\hat{\psi}$ as possible in the l^2 -metric. Therefore, we want to minimize the value D given by

$$\begin{aligned} D = \|\mathbf{g} - R\hat{\psi}\|^2 &= \|\hat{g} - R\hat{\psi}\|^2 = \sum_{m=0}^{N-1} |\hat{g}(m) - \hat{\psi}(m)\omega^m|^2 \\ &= \sum_{m=0}^{N_1-1} (|\hat{g}(m) - \hat{\psi}(m)\omega^m|^2 + |\hat{g}(m + N_1) - \hat{\psi}(m + N_1)\omega^{m+N_1}|^2) \\ &= \sum_{m=0}^{N_1-1} \left(\left| \frac{\sqrt{2}a(m + N_1)e^{i\sigma(m)}}{\sqrt{a(m)^2 + a(m + N_1)^2}} - a(m)e^{i(\alpha(m) + m\theta)} \right|^2 + \right. \\ &\quad \left. \left| \frac{\sqrt{2}a(m)e^{i\sigma(m + N_1)}}{\sqrt{a(m)^2 + a(m + N_1)^2}} - a(m + N_1)e^{i(\alpha(m + N_1) + m\theta + \pi)} \right|^2 \right). \end{aligned}$$

Set $b(m) = \frac{\sqrt{2}}{\sqrt{a(m)^2 + a(m + N_1)^2}}$. Thus, we need only minimize each term,

$$\begin{aligned} A(m) &= \left| b(m)a(m + N_1)e^{i\sigma(m)} - a(m)e^{i(\alpha(m) + m\theta)} \right|^2 + \\ &\quad \left| b(m)a(m)e^{i\sigma(m + N_1)} - a(m + N_1)e^{i(\alpha(m + N_1) + m\theta + \pi)} \right|^2. \end{aligned}$$

The term $A(m)$ is minimized when the arguments of the terms in each difference are identical, i.e.,

$$\sigma(m) = \alpha(m) + m\theta$$

and

$$\sigma(m + N_1) = \alpha(m + N_1) + m\theta + \pi.$$

Defined in this way, σ satisfies the phase relation above. From this result we get,

$$\widehat{g}(m) = b(m)a(m + N_1) e^{i(\alpha(m) + m\theta)} = \frac{\widehat{f}(m)}{\|\widehat{f}(m)\|} \|\widehat{f}(m + N_1)\| \omega^m,$$

which determines \widehat{g} , in turn, determining g . Note that g is not necessarily the l^2 -closest 1-admissible function to $R\psi$. The l^2 -closest 1-admissible function to $R\psi$ is Rf , where

$$\widehat{Rf}(n) = \frac{\widehat{\psi}(n) \omega^n}{(\sum_1 \psi)(n)}.$$

To use the ψ -binary decomposition algorithm, we first have to create the decomposition operator. This decomposition operator takes a vector, s , and decomposes it into, essentially, another vector, \underline{s} . Note: \underline{s} is not the vector s written with respect to the basis generated by even translates of f and g .

The decomposition operator takes the vector $s \in \mathcal{V}_0$ and decomposes it into two vectors, s_f and s_g , lying in orthogonal subspaces of equal dimensions. This process repeats again with these two vectors, s_f and s_g . Specifically, this operator projects the vector s into two orthogonal subspaces of dimension $\frac{N}{2}$, respectively. In each of these subspaces, we project the image of the original vector in each subspace into two more orthogonal subspaces, four altogether, and each having dimension $\frac{N}{4}$. We repeat this process until we project into two-dimensional subspaces. The final projection into one-dimensional subspaces is canonical: the two-dimensional subspaces are spanned by a particular vector (which will be described when we give the details of the operator) and its orthogonal complement; thus, the projected two-dimensional vector is canonically projected into the one-dimensional subspace spanned by that particular vector.

Let us now determine the first set of subspaces. Fix a real-valued function, ψ (written in the time domain) in $\mathcal{V}_0 = l^2(\mathbb{Z}_N)$. We assume this function is normalized. As explained above, we get the " l^2 -closest pair," f and g . Both f and g are also real-valued. The even translates of f and g , respectively, span mutually orthogonal subspaces of dimension $\frac{N}{2}$. Now, project the function ψ into the subspace spanned by the translates of f , and project the function $R\psi$ into the subspace spanned by the translates of g .

Call these projected functions ψ_f and ψ_g , respectively. Now, repeat the process within each subspace. Find the " l^2 -closest pair to ψ_f ," f_0 and g_0 , and the " l^2 -closest pair to ψ_g ,"

\mathbf{f}_1 and \mathbf{g}_1 . These vectors and their even translates span four subspaces, each of dimension $\frac{N}{4}$. Project the functions, ψ_f , $R\psi_f$, ψ_g , and $R\psi_g$, into the respective subspaces as in the first step above. Repeat the process until the subspaces are two-dimensional. Note that this operator, once the subspaces are determined, is a linear operator; it is just a sequence of linear projection maps.

This set of nested subspaces forms the ψ -binary decomposition operator. To use this operator on a function, s , take the function s and project it into this set of nested subspaces. The decomposition of the projection of s in the two-dimensional subspaces into scalars is canonical; the projections into the two-dimensional subspaces give pairs of numbers that will be the scalars.

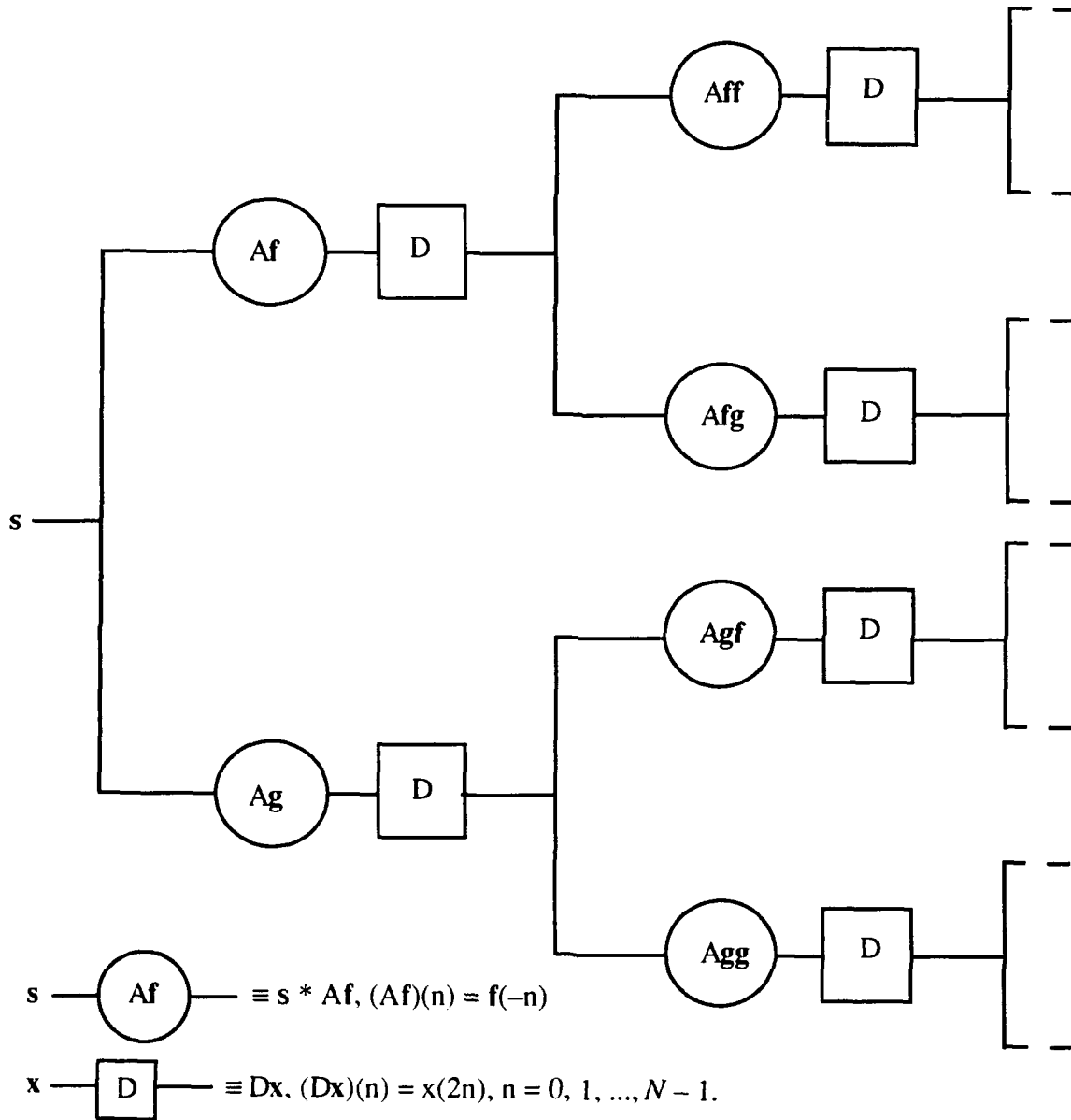
This projection is computed taking the inner products, $\langle s, R^{2k}\mathbf{f} \rangle$ and $\langle s, R^{2k}\mathbf{g} \rangle$ for $k = 0, 1, \dots, \frac{N}{2} - 1$. These inner products can be quickly computed by convolution:

$$\begin{aligned} \langle s, R^{2k}\mathbf{f} \rangle &= \sum_{n=0}^{N-1} \overline{f(n-2k)} s(n) \\ &= \sum_{n=0}^{N-1} f(n-2k) s(n), \text{ since } \mathbf{f} \text{ is a real vector,} \\ &= \sum_{n=0}^{N-1} (A\mathbf{f})(2k-n) s(n), \text{ where } (A\mathbf{f})(n) = f(-n), \text{ the involution operator,} \\ &= ((A\mathbf{f}) * s)(2k), \text{ where } * \text{ denotes convolution,} \\ &= D((A\mathbf{f}) * s)(k), \text{ where } D \text{ is the downsampling operator.} \end{aligned}$$

The inner products, $\langle s, R^{2k}\mathbf{g} \rangle$, are computed similarly. Like the wavelet filter bank designs, these inner products can be computed in the Fourier domain for added speed. This ψ -binary decomposition is illustrated in the following filter bank schematic in Figure III-7. Here, the first " l^2 -closest pair" will be denoted by \mathbf{f} and \mathbf{g} ; the second set of " l^2 -closest pair" will be denoted by \mathbf{ff} , \mathbf{fg} , \mathbf{gf} , and \mathbf{gg} , where \mathbf{ff} and \mathbf{fg} are the " l^2 -closest pair" in the subspace spanned by \mathbf{f} , and \mathbf{gf} and \mathbf{gg} are the " l^2 -closest pair" in the subspace spanned by \mathbf{g} .

Figure III-7

ψ -Binary Decomposition Filter Bank



CHAPTER IV

DETECTION ALGORITHM

In this chapter, we discuss the signal detection method used in the research. The method is a modification of the Neyman-Pearson (N-P) detection algorithm. This detection algorithm is optimal in a certain sense, which we will explain later. See References [n], [o], [l], [m], and [c].

We now explain the N-P detector in the context of this report; that is, we want to detect windowed, discretized signals. Assume we receive an incoming signal,

$$\mathbf{x} = (x(0), x(1), \dots, x(N-1)).$$

We would like to determine whether this incoming signal carries the prototype signal \mathbf{s} embedded in noise, where

$$\mathbf{s} = (s(0), s(1), \dots, s(N-1)),$$

or whether the incoming signal is just noise,

$$\mathbf{n} = (n(0), n(1), \dots, n(N-1)).$$

So we have two hypotheses:

$$H_1 : \mathbf{x} = \mathbf{s} + \mathbf{n},$$

and

$$H_0 : \mathbf{x} = \mathbf{n}.$$

Denote the choice of H_0 by C_0 , and the choice of H_1 by C_1 . Then there are four possible outcomes,

1. We correctly identify the presence of the signal. The probability of this outcome is called the *probability of detection* (P_d), denoted by $P(C_1 | H_1)$.

2. We mistakenly identify the presence of a signal when in fact the signal is not present. The probability of this outcome is called the *probability of false alarm* (P_{fa}), denoted by $P(C_1 | H_0)$.
3. We incorrectly determine that no signal is present when in fact the signal is present. The probability of this outcome is called the *probability of a false negative* (P_n) and is denoted by $P(C_0 | H_1)$.
4. Finally, we correctly determine the absence of the signal in an incoming signal that consists of just noise. The probability of this outcome is called the *probability of a true negative* (P_{tn}), denoted by $P(C_0 | H_0)$.

The two outcomes with which we are most concerned are the first two: the probabilities of detection and false alarm. Moreover, we assume an active sonar system. Thus, we should have, *a priori*, the probabilities of whether the signal is present, $P(H_1)$, or absent, $P(H_0)$. These probabilities will affect the overall outcome. For example, there is an expected return time of a transmitted signal. Around this expected time, the probability that the incoming signal carries the prototype signal in noise increases. Thus, the probabilities of detection and false alarm will differ from the usual situation where there is no signal expected.

The essence of the N-P detector is that for a fixed probability of false alarm, the probability of detection is maximized. This gives the optimality. This is accomplished through computing a maximum likelihood ratio. For a threshold β (determined by the false alarm probability), we choose H_1 when the test statistic λ is greater than or equal to the threshold; we choose H_0 otherwise. The test statistic, λ , is computed by the maximum likelihood ratio:

$$\lambda = \frac{p_1(y)}{p_0(y)}$$

where

λ = test statistic,

y = a value assigned to the observation \mathbf{x} ,

$p_1(y)$ = probability density function of y given that H_1 is true,

$p_0(y)$ = probability density function of y given that H_0 is true.

The probability density functions are Gaussian normal functions with means and deviations determined empirically. Essentially, the probability of false alarm sets a critical value for y , denoted by y_T . This critical value then determines the value of the threshold, β .

Without going into details (see References [n], [o], [m], [c], and [l] for the details and the computations), the test statistic is computed by a simpler expression,

$$\lambda = \mathbf{s}^T \mathbf{R}^{-1} \mathbf{x},$$

where \mathbf{R} is the noise correlation matrix. This test statistic is shown (see Reference [c]) to be independent of the basis for expressing the vectors and matrix. (In this sense, this implies that no particular basis choice will affect the outcome of the detector. In particular, wavelet basis or the Fourier basis will perform just as well as the time basis, with regard to the N-P detector.) This test statistic is essentially an inner product. If the noise is white noise, then the noise correlation matrix can be taken to be the identity matrix. We will assume this for the rest of the report.

The drawback to using the full N-P detector is the computing time. A *compressed* N-P detector will speed up the process by computing a partial inner product; that is, we first choose a basis for computational purposes. We then take M (a positive integer much smaller than N) coordinates of the vectors in this basis and compute the inner product with only these coordinates. Here, the choice of the basis is crucially important, as can be seen in our results.

In short, let A be a subset of $\{0, 1, \dots, N-1\}$, of cardinality L and B be a subset of $\{0, 1, \dots, N-1\}$ containing A and having cardinality $M \geq L$. Then, it is the case that the compressed test statistic based on the partial inner product with coordinates from A will be smaller than the test statistic based on the partial inner product with coordinates from B . Hence, the probability of detection grows as the testing subset increases in cardinality. That is,

$$\lambda_A \leq \lambda_B.$$

On the other hand, choosing a "wrong" subset A may cause λ_A to be small relative to λ . It may even be the case that $\#(A) > \#(B)$, but $\lambda_A \leq \lambda_B$, provided $B \not\subset A$. Here, $\#(A)$ denotes the cardinality of A .

The main contention is that when compressed to a subset $B \subset \{0, 1, \dots, N-1\}$ with respect to a particular basis, it is always the case that the compressed test statistic, λ_B , is less than

or equal to the full test statistic, λ . Thus, it may happen that $\lambda \geq \beta$, yet $\lambda_B \leq \beta$. This would increase the probability of a false negative outcome.

Continuing with the analysis, one constructs the compressed Z-parameter (see Reference [m]), which in our case is given as

$$Z_s^A = \left(\sum_{i \in A} |\underline{s}(i)|^2 \right)^{\frac{1}{2}},$$

where $A \subset \{0, 1, \dots, N-1\}$ is the compressing subset, and $\underline{s} = (\underline{s}(0), \underline{s}(1), \dots, \underline{s}(N-1))$ is the signal written with respect to some fixed orthonormal basis.

This Z-parameter is related to the test statistic, λ . The test statistic gives the probability of detection, P_d , as a function of the probability of false alarm, P_{fa} . The graph of this function is known as the Receiver Operating Characteristic curve, or the *ROC curve*. The compressed Z-parameter arises in the expression of P_d as a function of P_{fa} ,

$$P_d = Q(Q^{-1}(P_{fa}) - Z_s^A),$$

so that increasing the Z values improves the compressed detector toward optimality. (Here, $Q(x) = 1 - \Phi(x)$, where $\Phi(x)$ is the standard normal distribution function, often called the phi-function. See Reference [m]. It is sufficient to know that Q is a decreasing function. As x increases, Q(x) decreases; hence, as Z_s^A increases, $Q^{-1}(P_{fa}) - Z_s^A$ decreases, and P_d increases.)

Finally, we measure this Z-parameter as a dB loss. Define the degradation factor for using the compressing subset A with respect to the fixed orthonormal basis by

$$D_s^A = 20 \log_{10} Z_s^A.$$

Because the signal is normalized, we are actually computing the logarithm of the ratio of the compressed Z-parameter, Z_s^A , to the full Z-parameter, which is 1. By using this degradation factor, we can see how much energy is "lost" due to compression. We often plot the degradation factor as a function of the compression ratio,

$$\rho_A = \frac{\#(A)}{N}.$$

Thus, no degradation occurs when there is no compression and in this case, we have 0 dB loss. We reserve describing the results to Chapters V and VII.

The degradation loss, D_s^A , can also be interpreted as the change in the SNR at the output of detector. Since Z_s^A ranges between 0 and 1, D_s^A ranges from $-\infty$ to 0, respectively. Optimality corresponds to $D_s^A = 0$, that is 0 change in the SNR.

CHAPTER V

SIGNAL SELECTION

In order to test the utility of wavelet based detectors, we created a set of "standard" signals common to sonar processing. We will describe them in detail in Section 1. In Section 2, we describe the properties of these signals. Here, we will also discuss the Doppler Ambiguity Displays and use them to illustrate the differing characteristics of the signals. In Section 3, we discuss time-frequency distributions and how they can be used to understand signals. Although we have specified the parameters for our signals (e.g., signal length and sampling frequency), these parameters may be adjusted for any frequency range desired. Indeed, these parameters are user inputs in our C signal software package.

1. Signal Types

We study five types of signals: continuous wave (CW), hyperbolic frequency-modulated (HFM), linear frequency-modulated (LFM), pulse (PUL), and pseudo-random noise (PRN). They were all computer generated using the *Mathematica* mathematics software package. The routines are now currently rewritten in C for faster implementation and better access to other detection software packages like the multi-channel detection system (see Chapter V). These waveforms are described in the appendix of Reference [n] and are also described in References [p] and [q].

These basic parameters for all these signals are the same:

- Sampling Frequency, $f_s = 1000$ Hz.
- Window size, $N = 1024$.
- Signals are all normalized (in the l^2 -norm) to have unit norm.
- Some signals (e.g., the CHIP2 signal as described in Chapter VI) were created by taking parts of the above signals and concatenating them together.

Definition of the signals ($n = 0, 1, \dots, 1023 = N - 1$).

- CW: $s(n) = \cos(2\pi f n / f_s)$, where f is the desired frequency (in Hz), a user input. The equation given here is not normalized.

- HFM: $s(n) = \cos \left[-2 \pi N \frac{f_2 f_1}{(f_2 - f_1) f_s} \log \left| \frac{N f_2}{(f_2 - f_1) f_s} - \frac{n}{f_s} \right| \right]$, where the frequency range of the signal modulates from the lower value of f_1 (in Hz) to the upper value of f_2 (in Hz); they are user inputs. Again, the equation here is not normalized. The frequency - vs. - time plot of this signal should yield a hyperbola in the form of $y = 1/(C - x)$, where C is the asymptote. Aliasing may occur if the frequency range extends beyond the maximal discrete frequency. Note that the upper and lower frequency bounds cannot be equal.
- LFM: $s(n) = \cos \left[\frac{\pi (2n - N) [4N f_m + f_w (2n - N)]}{4N f_s} \right]$, where f_m is the median frequency, and f_w is the frequency sweep, both in Hz.. At the midpoint of time, the signal has the median frequency. The frequency sweep from the beginning of signal to the end of the signal is f_w . Again, both the median and the sweep frequencies are user inputs. The frequency - vs. - time plot of this signal should yield a line given by the equation $y = mx + b$. If the frequency sweep extends beyond the maximal discrete frequency (Nyquist frequency), there will be aliasing as in the HFM case.
- PRN: The pseudo-random noise is constructed by first taking a completely (uniform) random noise sample (we used the `Random[]` function in *Mathematica*) and taking its Fourier transform. The user inputs are a lower and upper frequency bound. The lower frequency is greater than or equal to the minimal discrete frequency and the upper frequency is less than or equal to the maximal discrete frequency. In the Fourier domain, the lower and upper frequencies are lower and upper bounds. We then take the Fourier transform of the random signal and zero out all the discrete frequency values outside the interval defined by the upper and lower frequency bounds. (Actually, because the random signal is real-valued, there will be two disjoint intervals.) We set $\hat{s}(0)$ equal to its given value instead of zeroing it out because this should be nonzero.
- PUL: $s(n) = \sin(\pi n f_c / f_s) \sin(2 \pi n f_{sig} / f_s)$, where f_c is the carrier frequency, and f_{sig} is the signal frequency, both in Hz. The carrier frequency will typically be much smaller than the signal frequency so that half the period for the carrier is equal to the window length (1.024 seconds in our case). Again, both frequencies are user inputs.

The definitions of the above signals can be seen in the schematics of a time-frequency plot of Figure V-1. We will provide more detail about time-frequency distributions in Section 3. There, we have actual Fourier spectrograms, frequency-versus-time plots, of the above signals.

Figure V-2 shows the time-series plot of the above signals. Note that the time-series plot of HFM and LFM look quite similar; the differences are not easily discerned. In the time-frequency distributions, these differences are easier to discern.

In the following chapter, we use a "chip" signal. A chip – also known as a chirp – is a signal built up by concatenating a sequence of the above type signals.

Figure V-1
Frequency vs. Time Plots

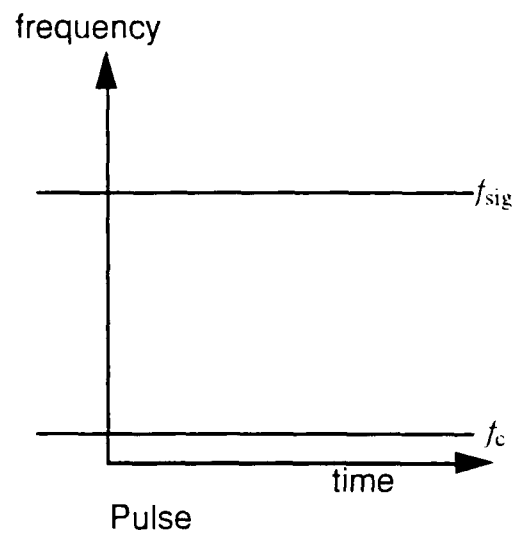
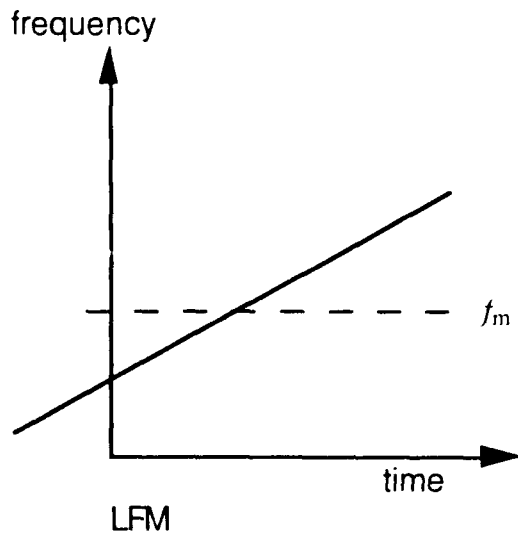
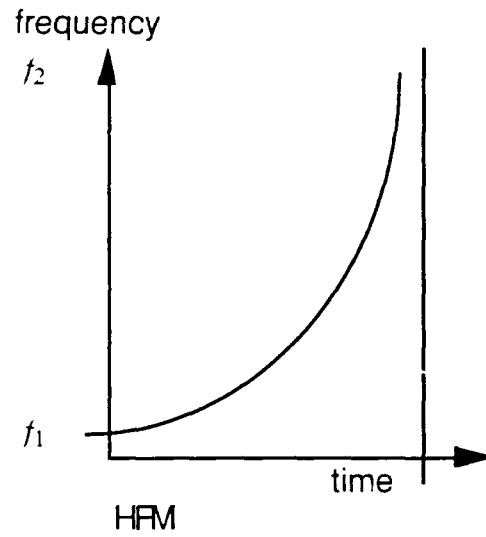
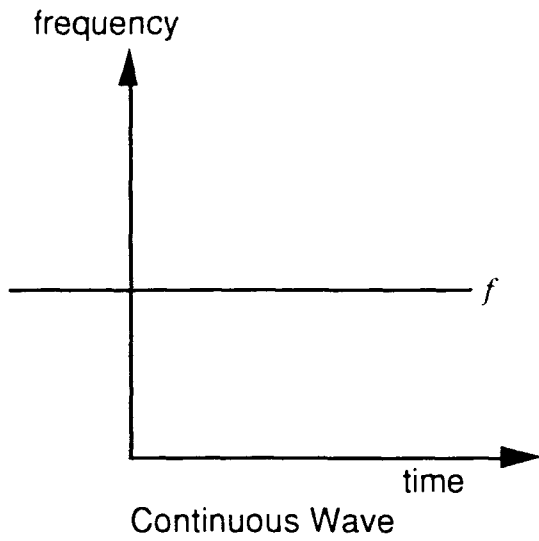
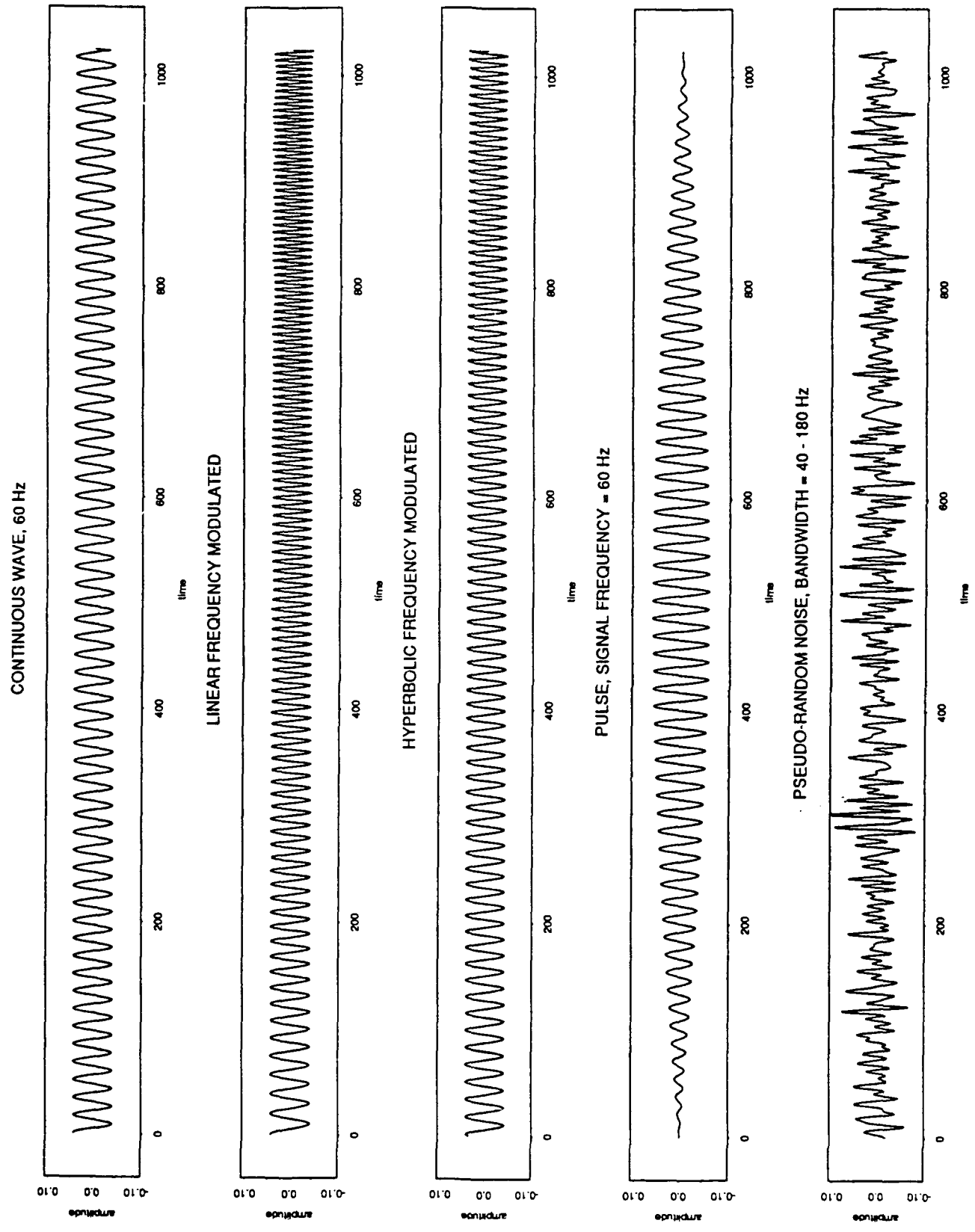


Figure V-2
Time-Series Plots of the Signals



2.1. Properties of these Signal Types

The sonar parameters listed in Chapter I dictate that sonar systems operate at low frequencies and use broad-band and long-duration signals, see Reference [q]. These parameters determine the type of information one can get from the sonar signal, which, in turn, is quantitatively dictated by the Doppler Ambiguity display for the signal.

A Doppler Ambiguity display shows how different a signal is when translated in time or Doppler-shifted in frequency, or both. The ambiguity function for a signal $s(t)$ is the magnitude-squared of the uncertainty function. One defines the uncertainty function (the uncertainty comes from changes in both frequency and time; compare to the Heisenberg Uncertainty Principle of quantum mechanics) by

$$\psi(\tau, \delta) = \frac{1}{E} \int_{-\infty}^{\infty} \overline{s[(1 - \delta)t]} s(t + \tau) dt.$$

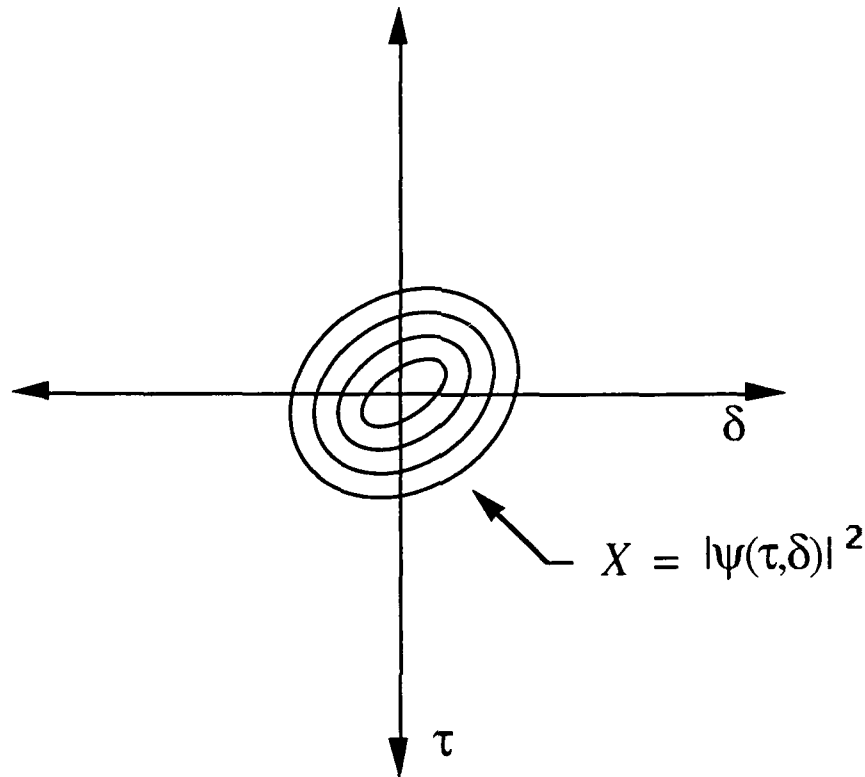
The variables τ and δ correspond to variation in time and frequency respectively. The uncertainty function measures how close a time-shifted version of the signal, $s(t + \tau)$, is to a frequency-shifted version of the signal, $s[(1 - \delta)t]$. We take the complex conjugate of the frequency-shifted version because the signal could conceivably be complex-valued. In the case when δ and τ are both zero, then we get the l^2 -norm of the signal. This is where the uncertainty function achieves its maximum value. The ambiguity function for the signal $s(t)$ is then given by

$$X_s(\tau, \delta) = |\psi(\tau, \delta)|^2.$$

One way to use the Doppler Ambiguity plot is to take the return signal (provided one has detected it) of a prototype signal and compute the inner product of it with time- and frequency-shifted versions of the prototype signal. The maximum value of these inner products will give the user an idea of how much shifting is due to time (i.e., from range effects) or frequency (i.e., from relative motion effects).

Figure V-3 shows the level curves of a hypothetical ambiguity function.

Figure V-3
Level Curves on an Ambiguity Surface



Our standard signals all produce their own characteristic ambiguity diagrams. We will discuss each of the example signals separately. The examples consist of two types of each of the signal types. They are:

- CW: We made two continuous waves, one is at 60 Hz and the other is at 120 Hz.
- HFM: The first hyperbolic frequency-modulated signal has a wide band; it sweeps from 20 Hz to 200 Hz. The second hyperbolic frequency-modulated signal is narrow-banded, sweeping only from 80 Hz to 120 Hz.
- LFM: The linear frequency-modulated signals are similar to the HFMs. The first is wide-banded, with a linear sweep from 20 Hz to 200 Hz, and the second is narrow-banded, sweeping linearly from 80 Hz to 120 Hz. Notice some aliasing in the wide-band signal, near the upper frequency end.

- PRN: Again, the two pseudo-random noise signals are banded like the two frequency-modulated signals. The first pseudo-random noise signal is banded between 20 Hz and 200 Hz. The second is banded between 80 Hz and 120 Hz. Note that the second PRN looks less stochastic than the first, although both were randomly generated.
- PUL: Here, both pulse signals have a signal frequency of 100 Hz. The difference is that the first is more transient; its support is only 0.512 seconds. The second pulse signal has a longer support, taking up the whole window (1.024 seconds).

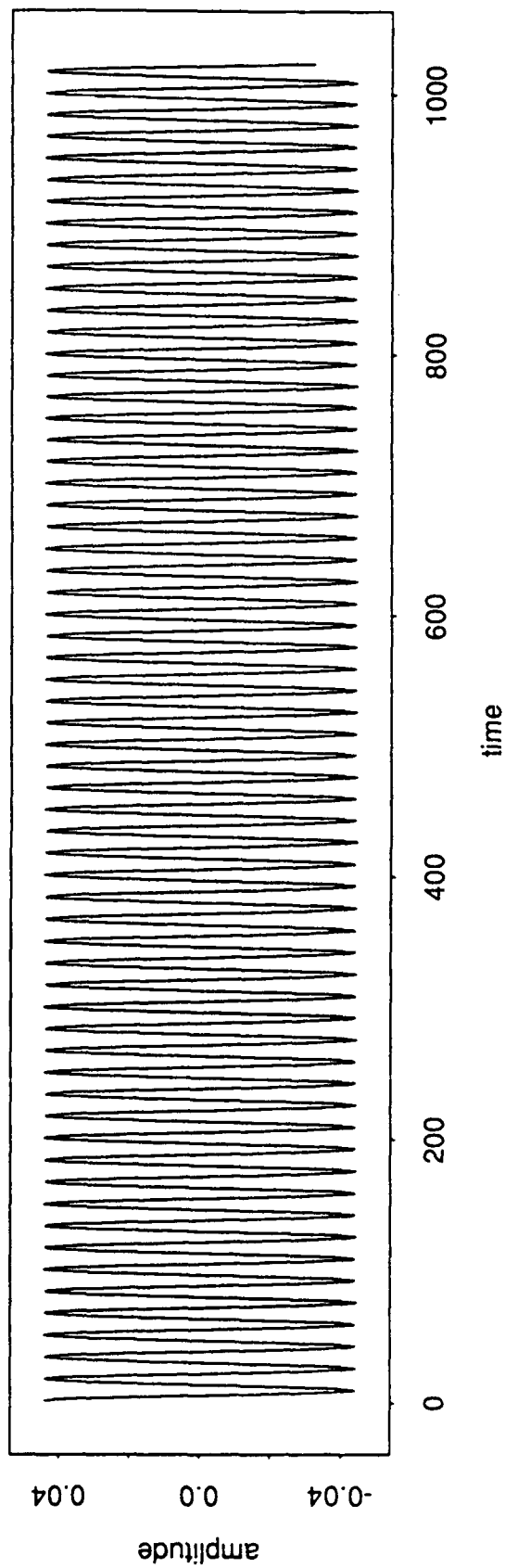
2.2. Continuous Wave Signals

Figure V-4 shows the time-series plot of the two continuous waves. Figures V-5 and V-6 show the Doppler Ambiguity plots for the two signals. Notice in the Doppler Ambiguity plots that the main lobe is an almost vertical ellipse. Also, this lobe repeats itself in the time (horizontal) direction, suggesting that Doppler shifts can be measured by the width of the elliptical lobe (any one of them). The thinner the width, the greater the Doppler shift. One can determine the direction of the Doppler shift by determining whether the frequency has been shifted up or down.

The elliptical lobe shape is more pronounced in the higher frequency signal, CW 120 Hz; see Figure V-6. This occurs because the amount of frequency shifting due to a fixed relative speed is proportional to the square root of the frequency. Thus, the lobes of CW 120 Hz are shorter in the vertical direction. Thus, the CW 120 Hz signal is better for Doppler detection than the CW 60 Hz signal.

The periodicity in the time direction shows that these signals do not perform well in determining time differences (i.e., range determination). If one sends out a CW signal and compares the return signal with time translates of the prototype signal, one cannot tell whether or not there have been delays in the transmitted signal. As seen in the Doppler Ambiguity plots, this drawback is even more pronounced in the higher frequency signal (another example of the effects of the Uncertainty Principle).

CW (60 Hz)



CW (120 Hz)

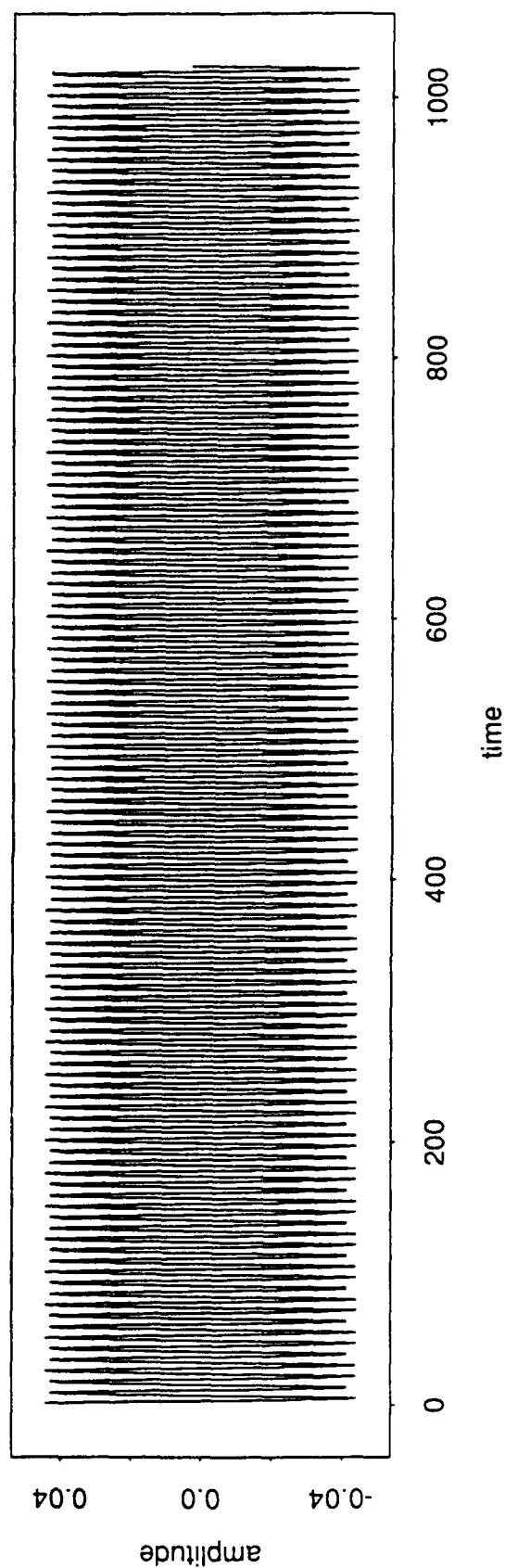


Figure V-4

Doppler Ambiguity for CW 60 Hz

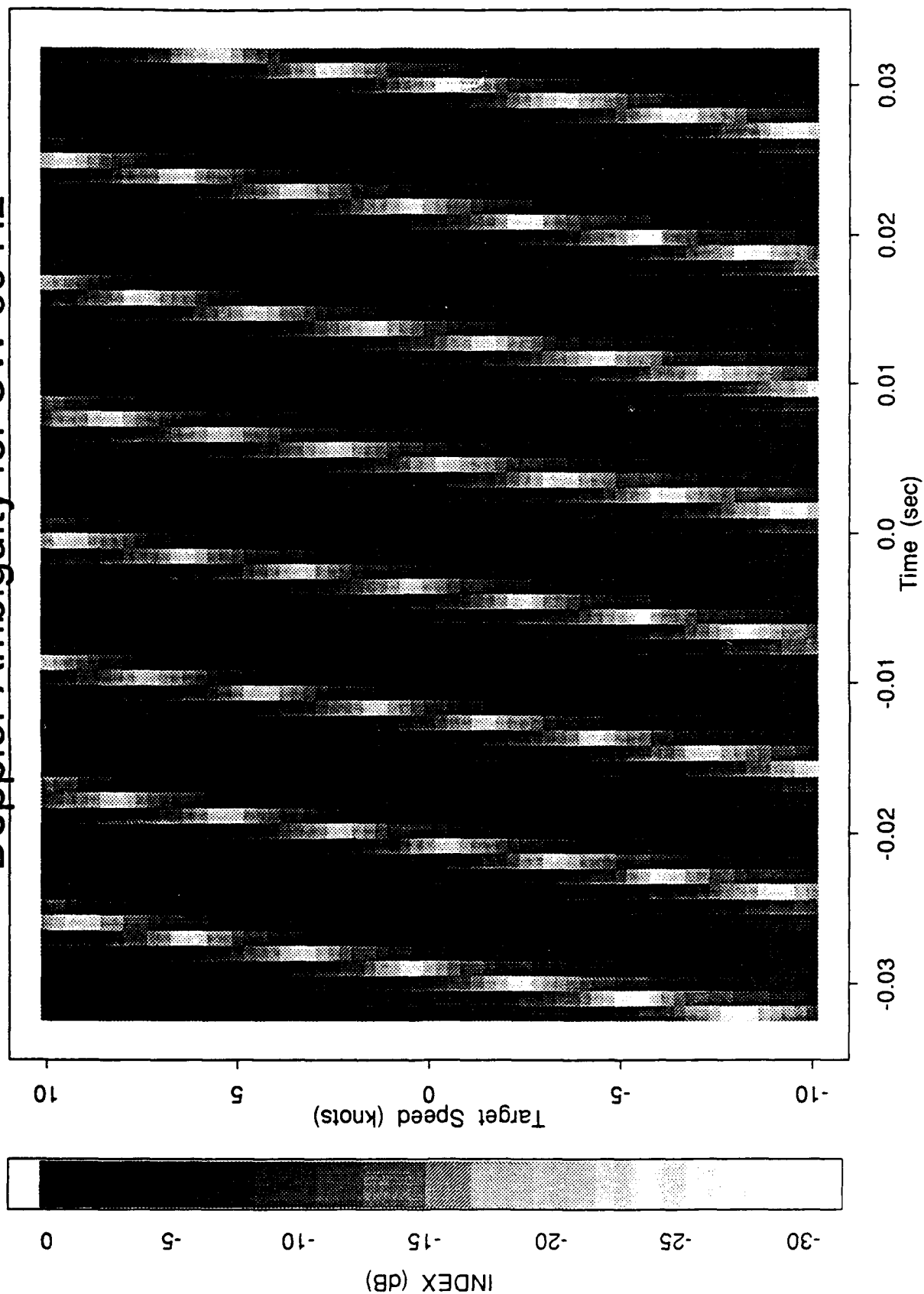


Figure V-5

Doppler Ambiguity for CW 120 Hz

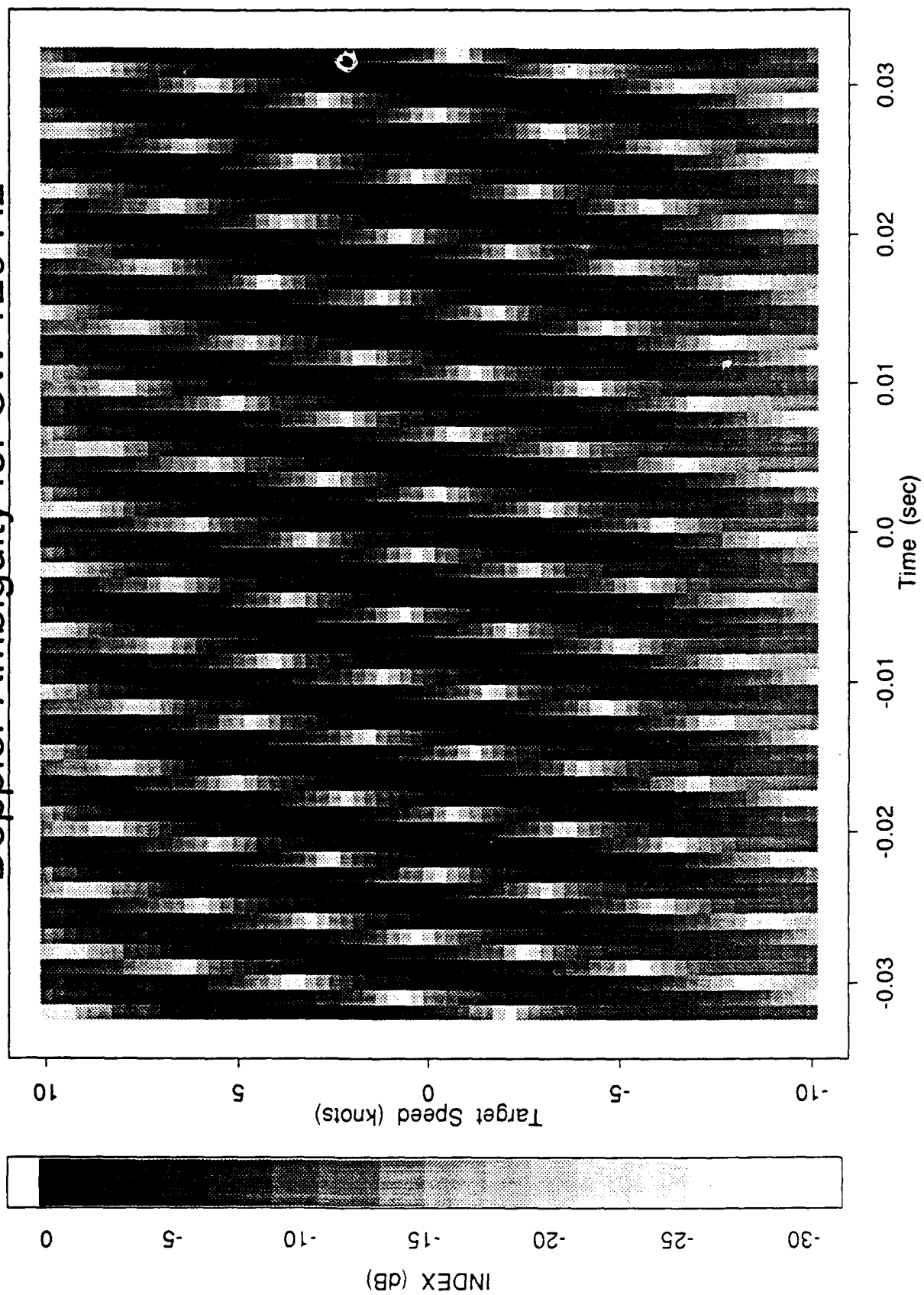


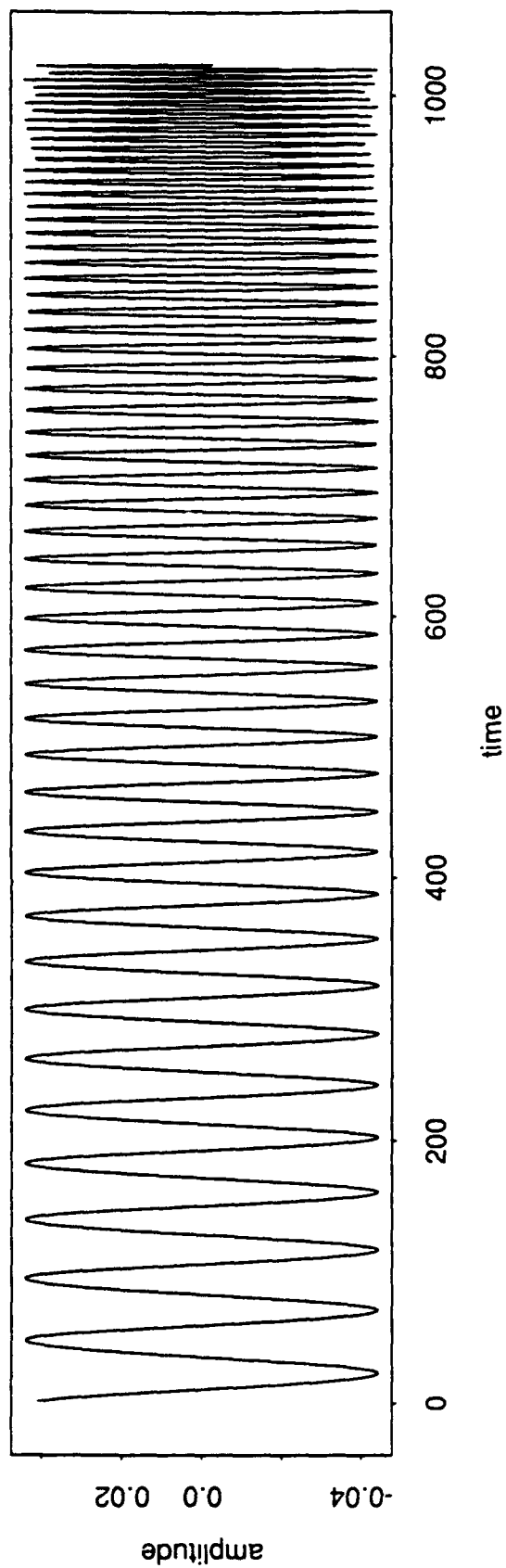
Figure V-6

2.3. Hyperbolic Frequency-Modulated Signals

Figure V-7 shows the time-series plots of the two HFM signals. Notice the second signal is almost like a continuous wave. This effect is also seen in the Doppler Ambiguity plots, Figures V-8 and V-9. The plot for the wide-band HFM signal shows one main lobe (which has a fairly constant width) and two weaker side lobes. The constant width of the main lobe means that a Doppler shift of the original signal behaves similarly to the unshifted version. There would be no side lobes if the signal were infinite in time (or at least sufficiently long in time). In that case, one cannot measure Doppler shifts at all. On the other hand, one can measure time shifts by noting how far one is from the main lobe. For an infinite length signal (i.e., no side lobes), one can measure time shifts with even better accuracy.

The narrow-band HFM signal has a vague main lobe shape, consisting of many small ellipses (characteristic of CW signals). The vagueness of the main lobe says that although one can use this to determine time shifts, it is not very accurate. Similarly, one can also determine Doppler shifts, but not as well as when using CW signals.

HFM (20-200 Hz)



HFM (80-120 Hz)

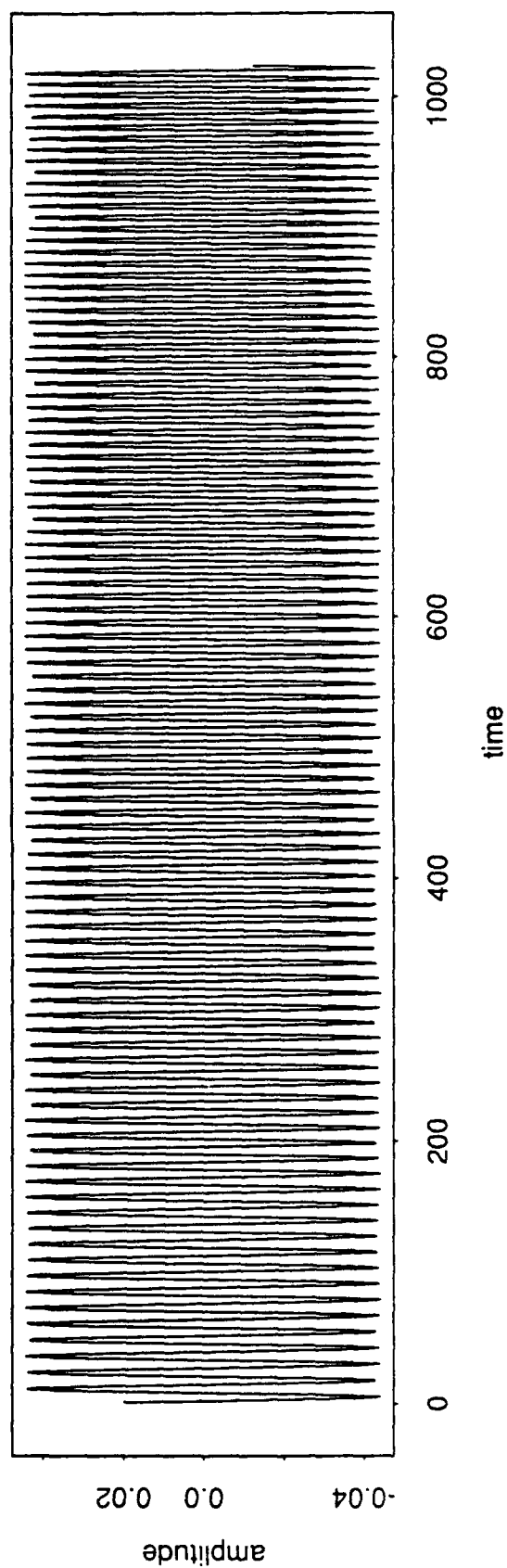


Figure V-7

Doppler Ambiguity for HFM 20-200 Hz

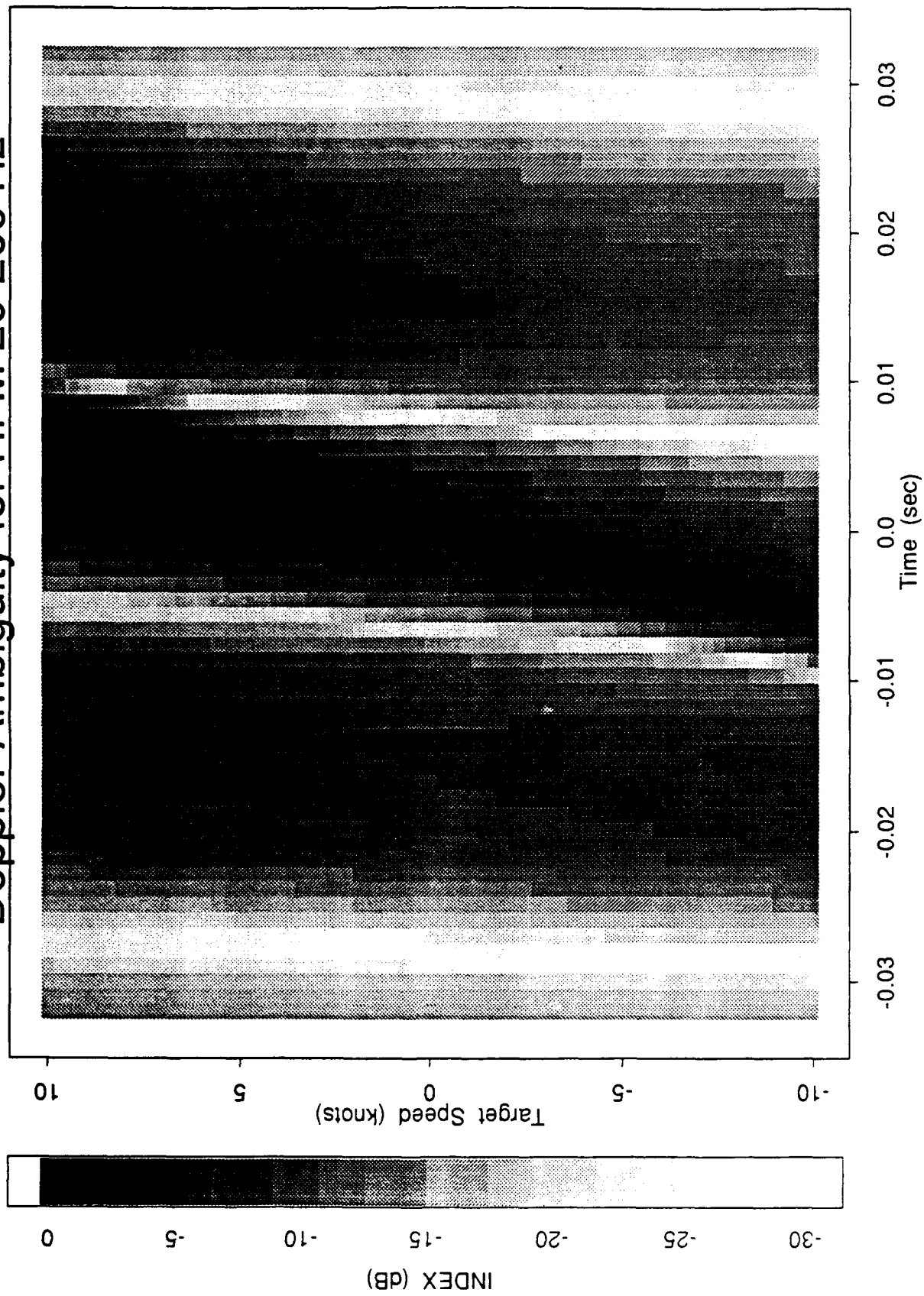


Figure V-8

Doppler Ambiguity for HFM 80-120 Hz

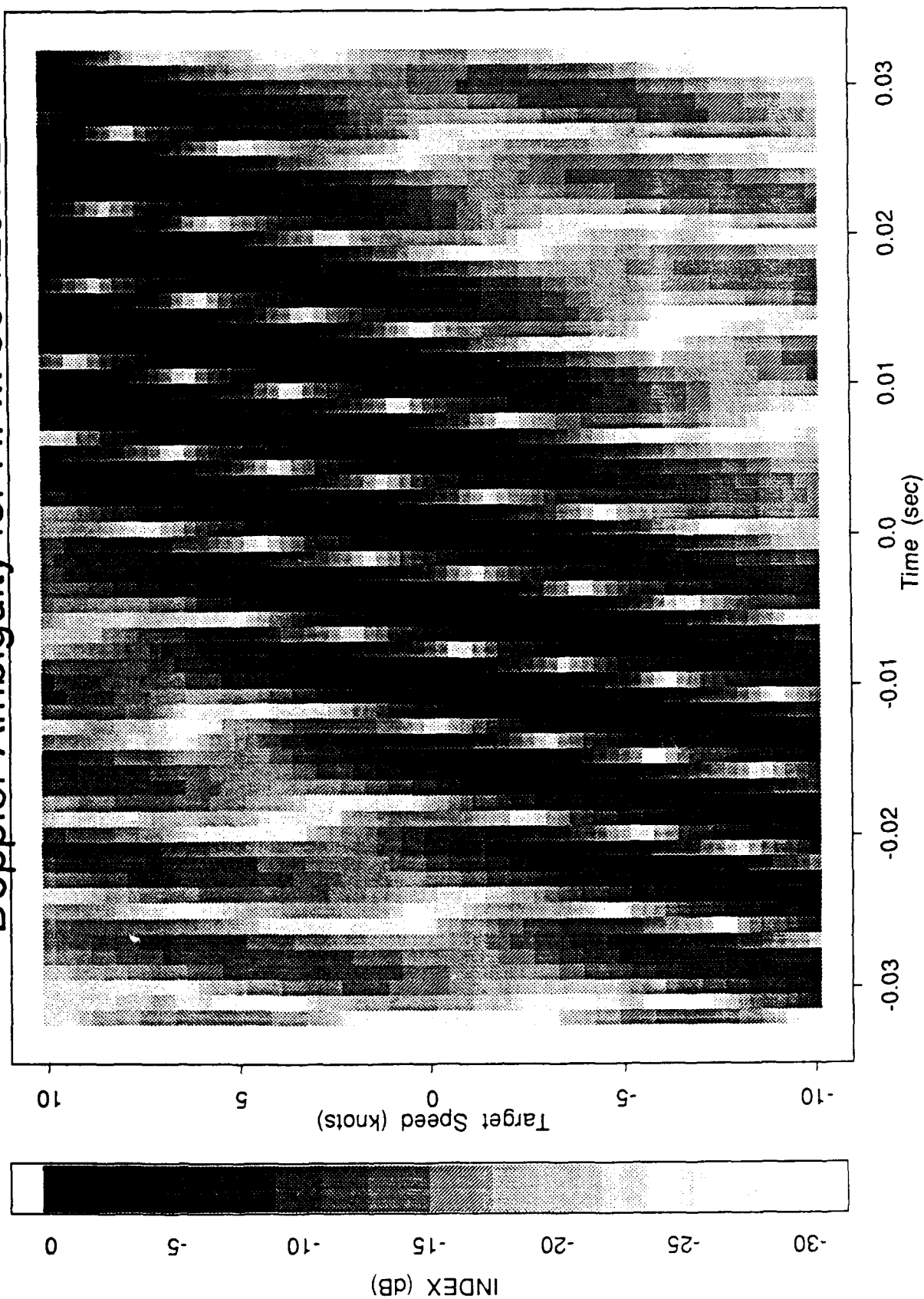


Figure V-9

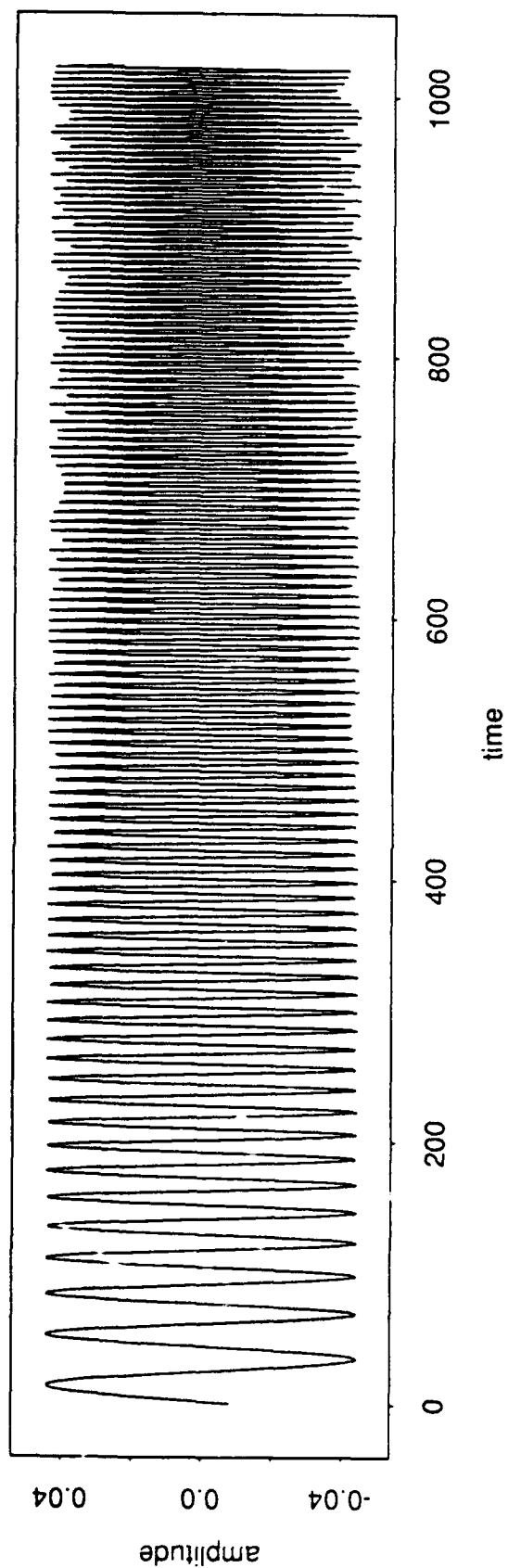
2.4. Linear Frequency-Modulated Signals

It seems as though there is not much difference in the time-series plots of linear frequency-modulated signals versus HFM signals. See Figure V-10 for two time-series plots of LFM signals. There is, however, a great difference in their Doppler Ambiguity plots. One can also see, from the next section, how their Fourier Spectrograms differ. Again, the narrow-band LFM signal is quite similar to the narrow-band HFM signal. This is only reasonable, since there is not much room for the frequency to modulate in either case.

As seen in the Doppler Ambiguity plot of a wide-band LFM signal, Figure V-11, one can determine both time and frequency shifts. The drawback is that, aside from the peak at the middle, the height of the plot is uniformly low. This puts a constraint on the precision of the measurement.

The narrow-band LFM signal, as mentioned above, is very much like the narrow-band HFM signal. Even the Fourier Spectrogram distributions are not much different. As mentioned at the head of Subsection 2.1, the useful choice for signals would be wide-band signals. The similarity of the two narrow-band signals, HFM and LFM, shows why wide-band signals are more useful.

LFM (20-200 Hz)



LFM (80-120 Hz)

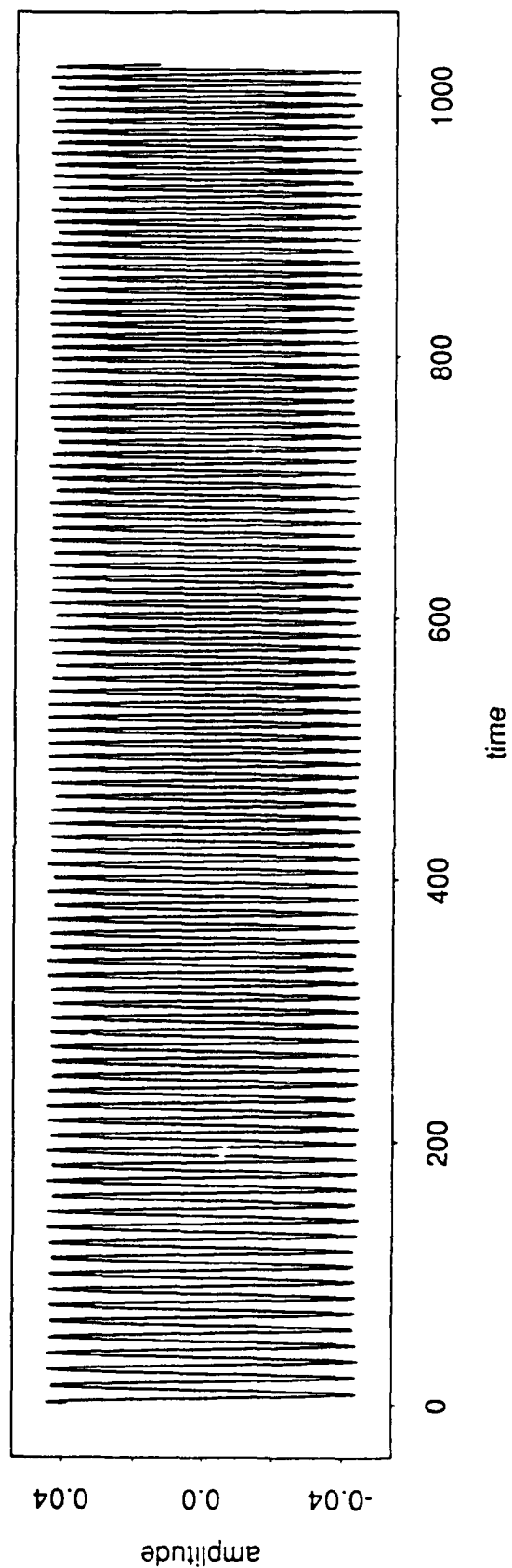


Figure V-10

Doppler Ambiguity for LFM 20-200 Hz

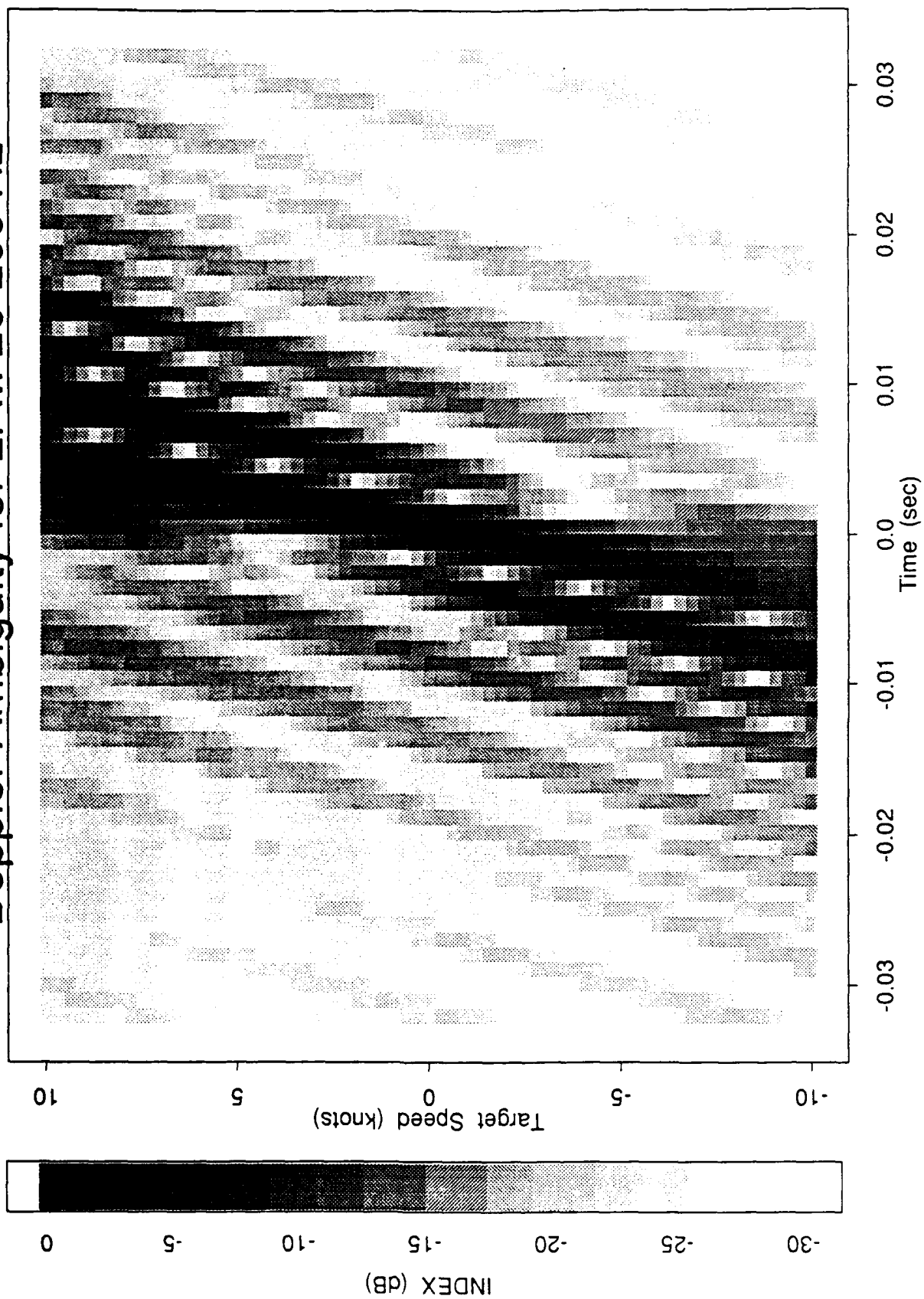


Figure V-11

Doppler Ambiguity for LFM 80-120 Hz

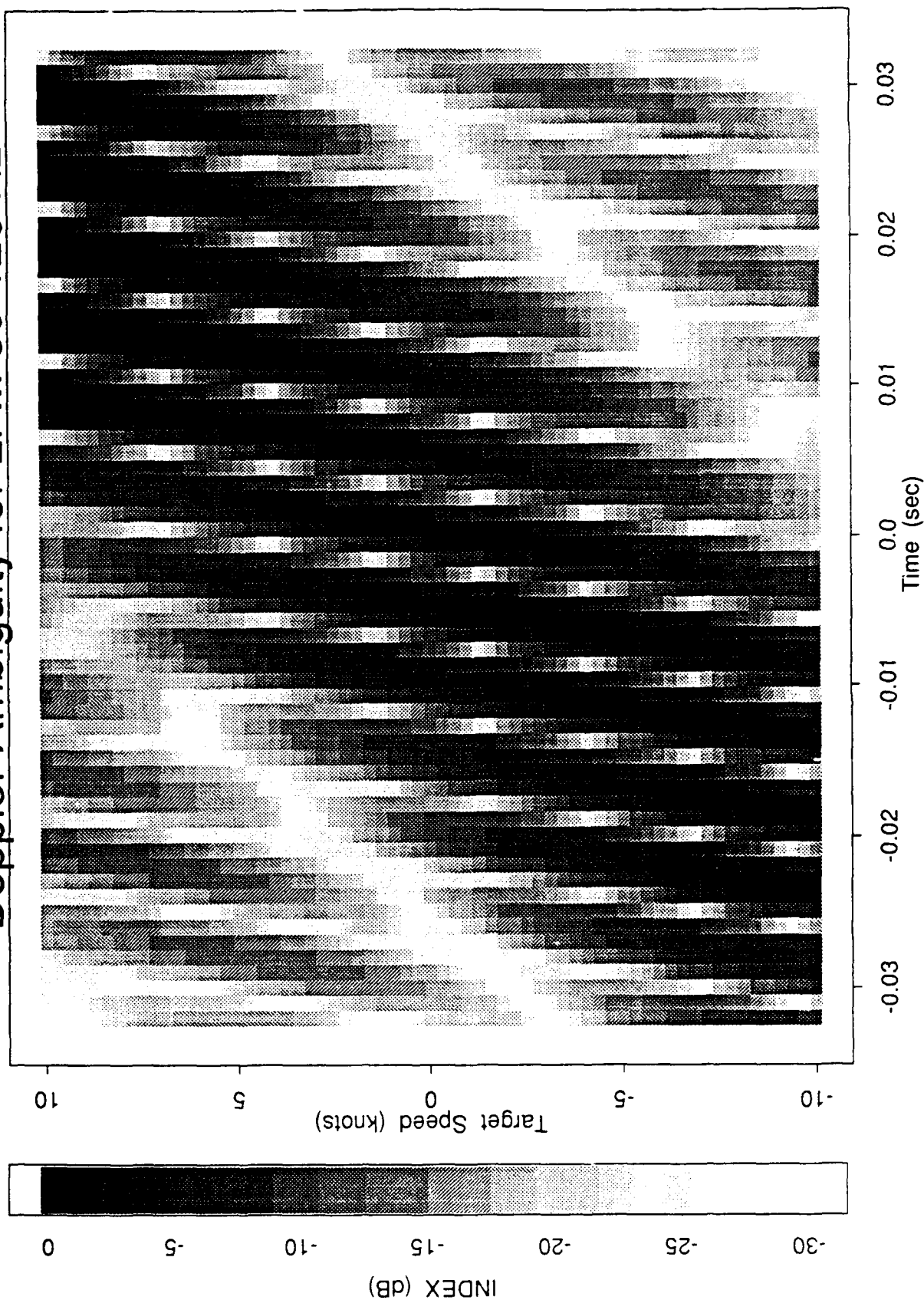


Figure V-12

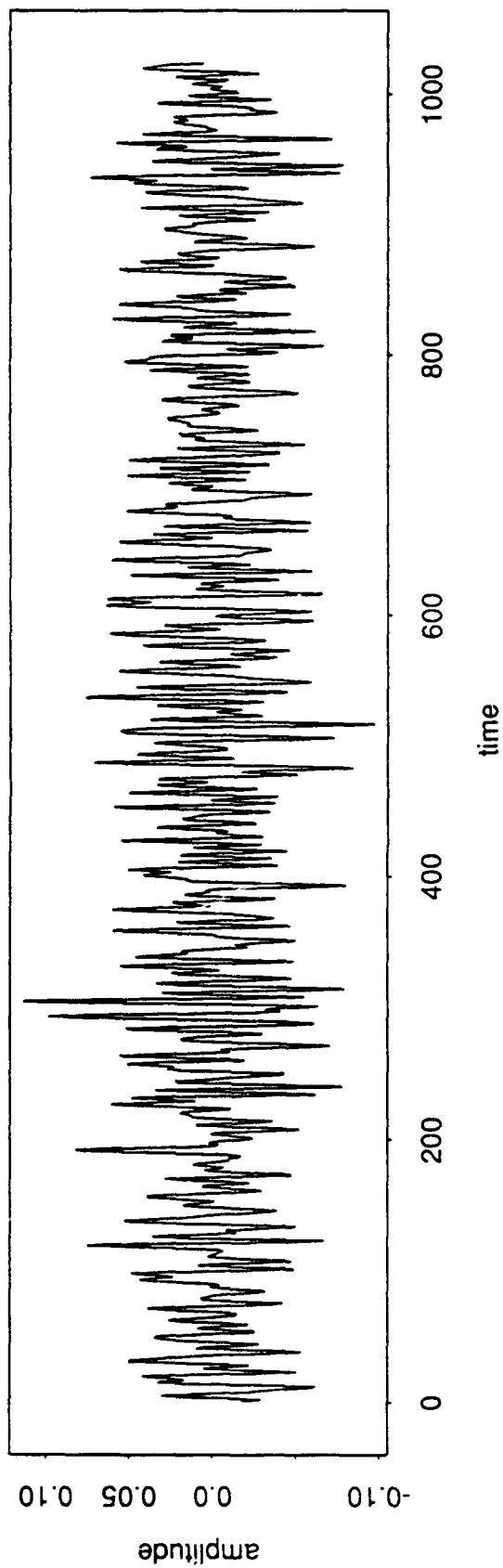
2.5. Pseudo-Random Noise Signals

The first pseudo-random noise signal, band-limited to between 20 Hz and 200 Hz, looks more like noise than the second. Note that we call them signals, for although they were pseudo-randomly generated, they can be re-created exactly. (A pseudo-random number generator is a fixed sequence of random numbers. A random number generator produces random numbers that cannot be re-created. They are truly stochastic. A pseudo-random noise signal is not only generated by a pseudo-random number generator, but is also band-limited. Thus, pseudo-random noise may actually be a signal in the sense that it can be re-created. Figure V-13 shows the two PRN signals.

The Doppler Ambiguity plot of the wide-band PRN signal, Figure V-14, is very peaked at the center and drops off in all directions. This says that such signals have poor Doppler or time-shift measuring capabilities. Their use is primarily for covert pinging. The randomness hides the signal in the ambient noise of the medium, and the signal peak of the Doppler Ambiguity plot means one can get good estimates for range.

The narrow-band PRN signal's Doppler Ambiguity plot, Figure V-15, is also peaked, but the drop-off is not as sudden as in the wide-band PRN signal Doppler Ambiguity plot. This Ambiguity plot also shows just a hint of continuous wave-like properties. One can measure, with more accuracy, both range and direction changes using this narrow-band PRN signal. However, like the LFM signals, the drop-off only makes it more difficult to detect differences.

PRN (20-200 Hz)



PRN (80-120 Hz)

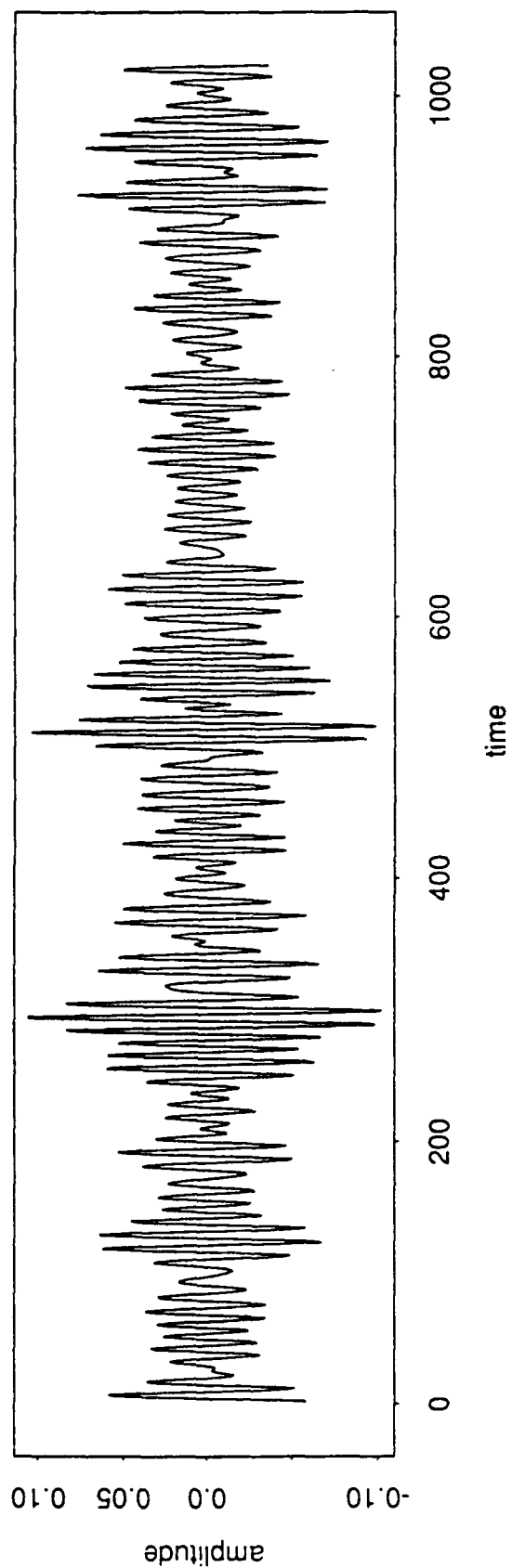


Figure V-13

Doppler Ambiguity for PRN 20-200 Hz

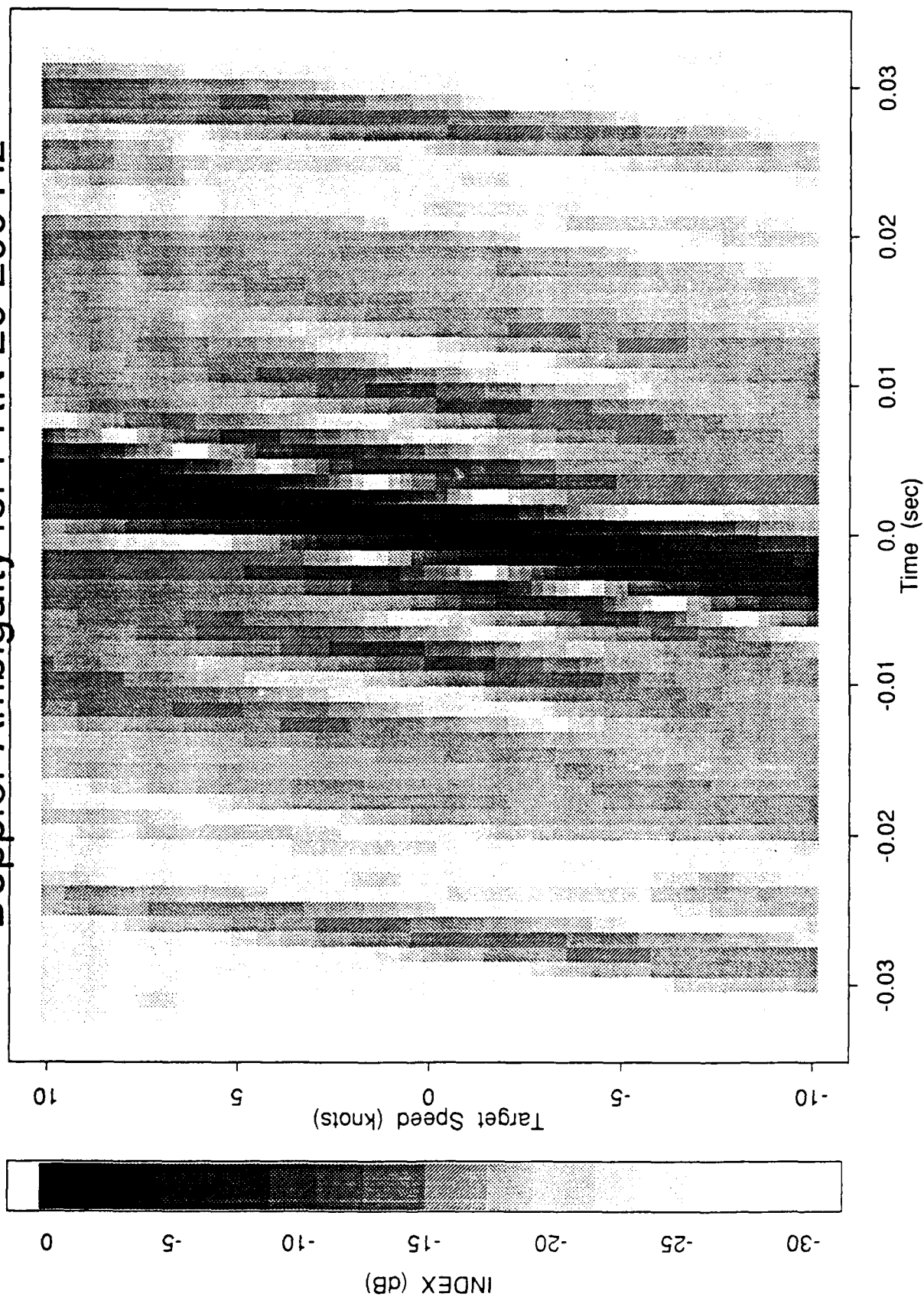


Figure V-14

Doppler Ambiguity for PRN 80-120 Hz

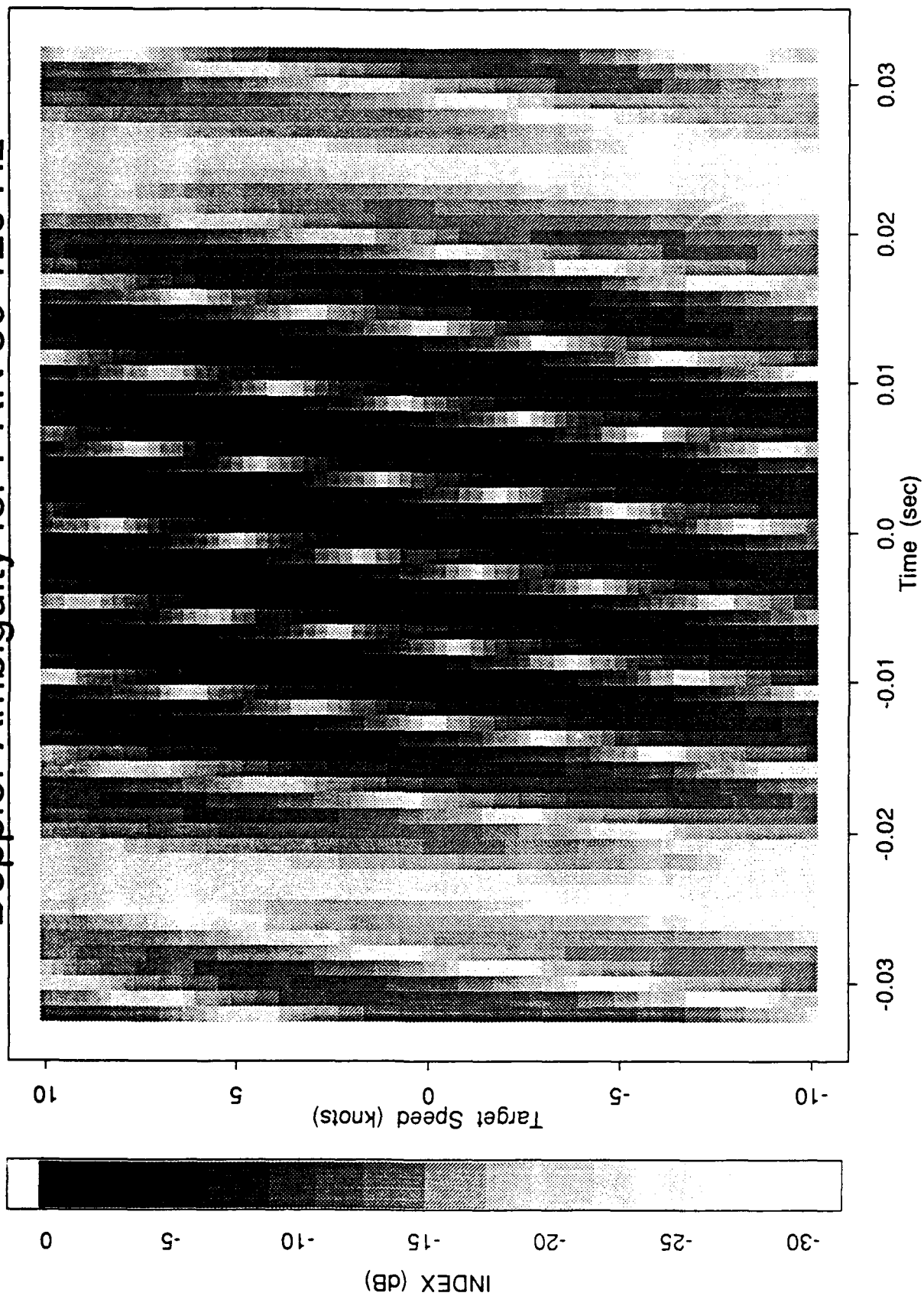


Figure V-15

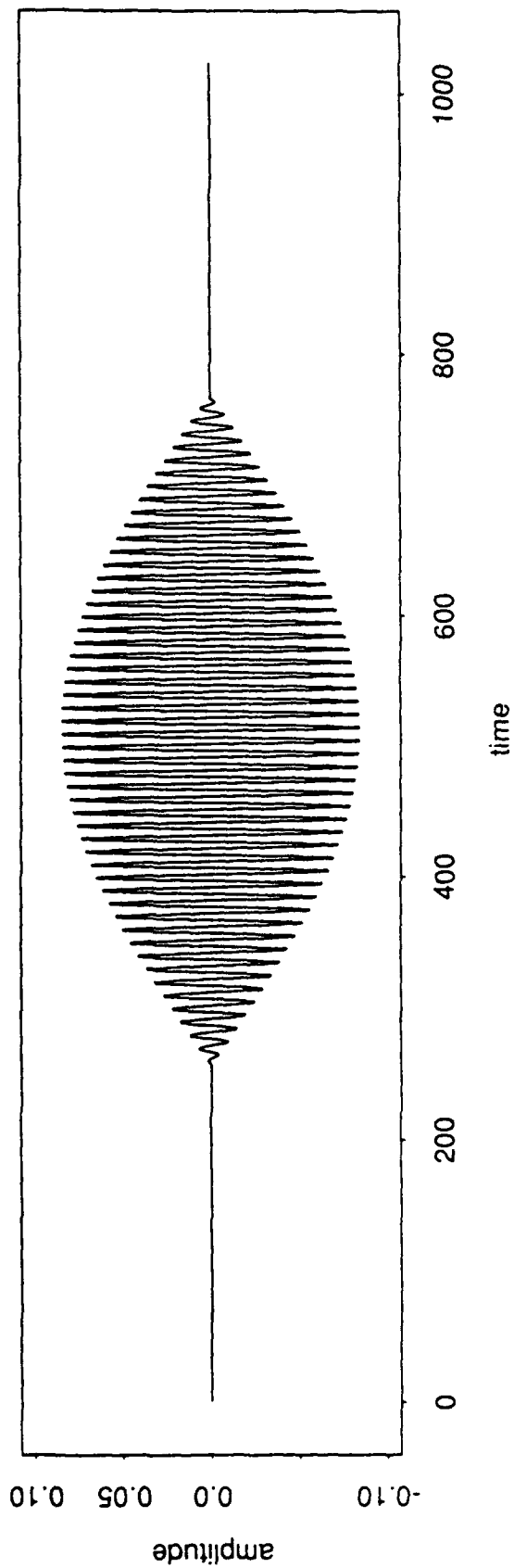
2.6. Pulsed Signals

Our time-series plots of the two pulse signals are shown in Figure V-16. The first is more transient than the second. Because these signals have a constant signal frequency (of 100 Hz), they should perform somewhat like the CW signals. This means they should be able to distinguish Doppler shifts. Also, because these signals are transient, they should also yield some range information. To some extent, they do, but their Doppler Ambiguity plots, Figures V-17 and V-18, do not really bear this out.

For the short pulse, note that the center lobe of the its Doppler Ambiguity plot extends all the way from the bottom to the top with uniform thickness. This suggest a delta function-like property. A delta, or spike, function will yield no information on Doppler shifts and will have a vertical main lobe that is also uniformly thick.

The long pulse has some CW signal-like properties; the vertical lobes are elliptical in shape, so that Doppler shifts can be determined. We believe that even our long pulse is too short. A longer pulse within a larger window would yield much better information on both frequency and time shifts.

PUL (100 Hz, Short)



PUL (100 Hz, Long)

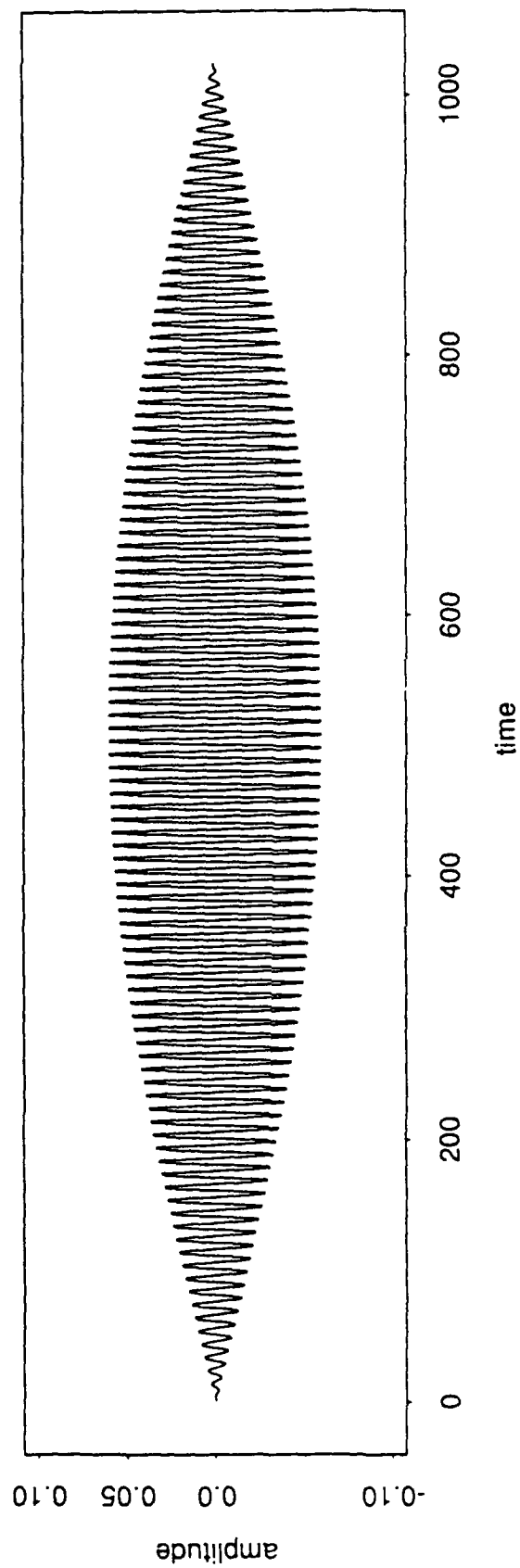


Figure V-16

Doppler Ambiguity for PUL 100 Hz, Short

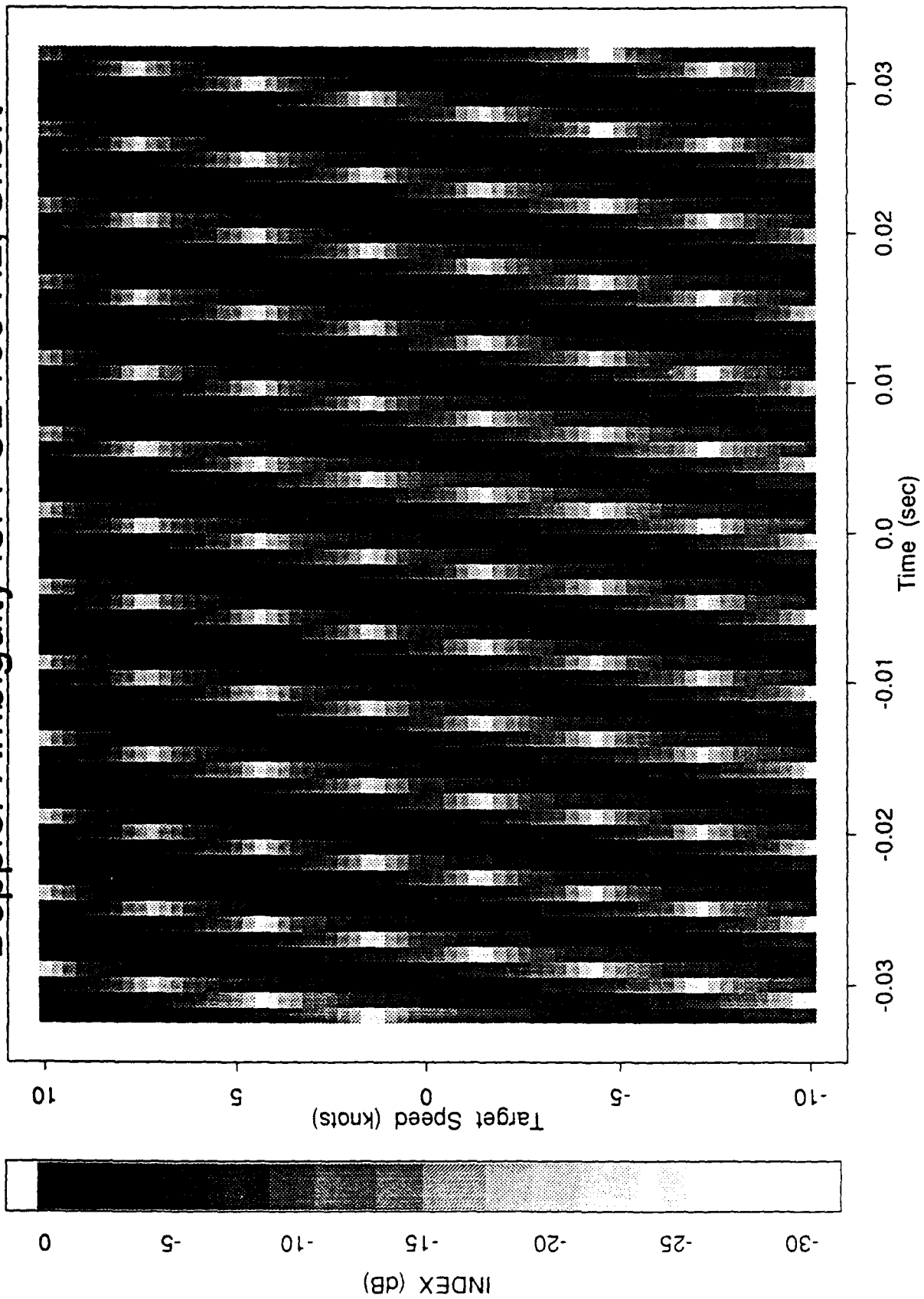


Figure V-17

Doppler Ambiguity for PUL 100 Hz, Long

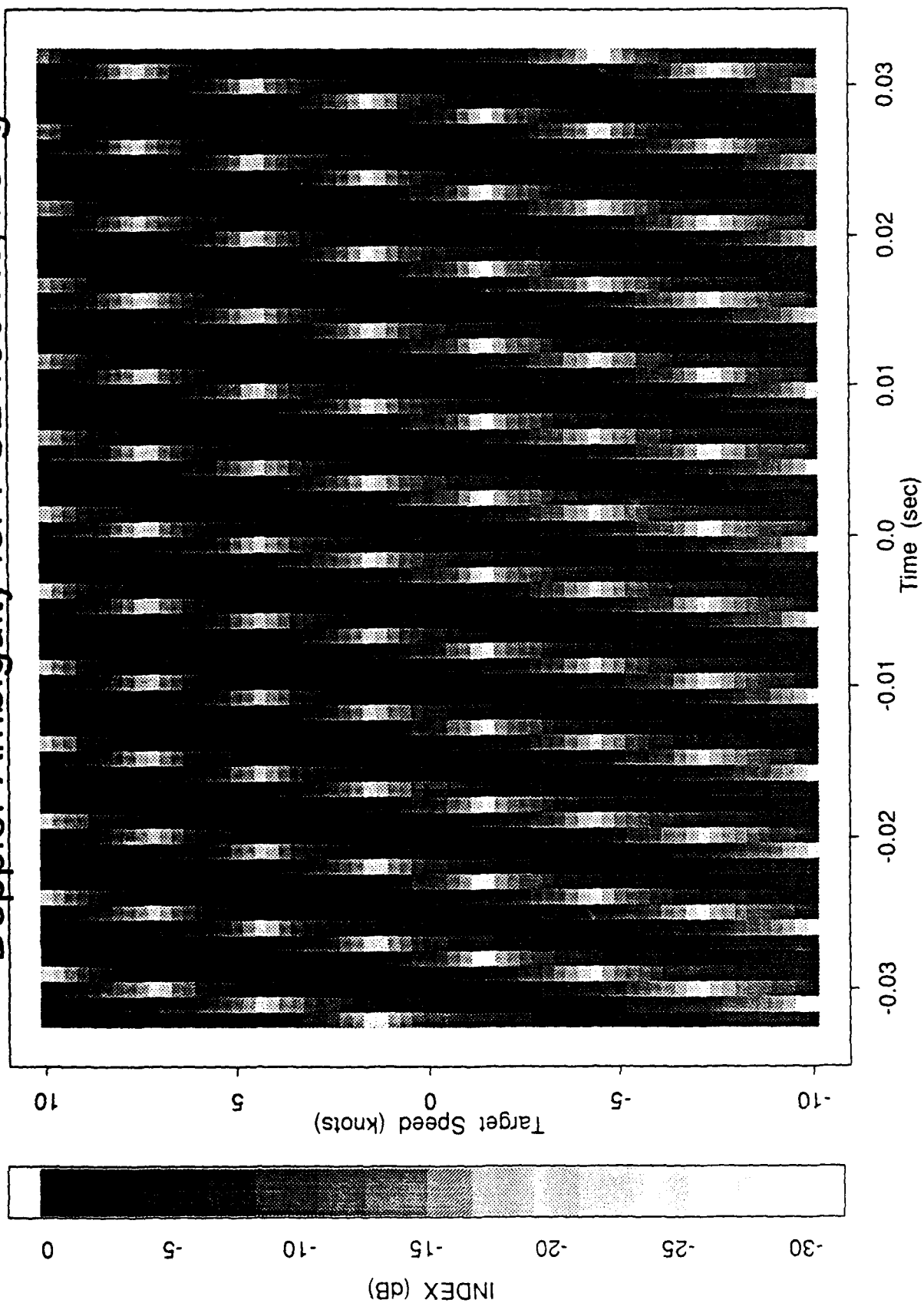


Figure V-18

3. Time-Frequency Distributions

In this section we will briefly describe the notion of time-frequency distributions. Although we will discuss various types of such distributions, we will illustrate only the Fourier Spectrogram.

The basic idea of a joint time-frequency distribution is to describe the energy density or intensity of a signal simultaneously in time and frequency. From harmonic analysis, we know that the instantaneous energy of a signal $s(t)$ (at time t_0) is the square of the absolute value,

$$|s(t_0)|^2 = \text{intensity per unit time at time } t_0.$$

By taking the Fourier transform of the signal $s(t)$,

$$\hat{s}(\omega) = \frac{1}{\sqrt{2\pi}} \int_{-\infty}^{\infty} s(t) e^{-i\omega t} dt,$$

we can also determine the intensity of the signal per unit frequency:

$$|\hat{s}(\omega)|^2 = \text{intensity per unit frequency at frequency } \omega.$$

The normalization in the Fourier transform means that

$$\int |s(t)|^2 dt = \int |\hat{s}(\omega)|^2 d\omega = \text{total energy} = 1$$

where the integrals are over the domain of the respective functions and we will set the intensity of the signal so that the total energy is equal to 1. What we would like to construct is a joint function of time and frequency that represents the energy or intensity per unit time and frequency. We have such a distribution, namely,

$$F(t, \omega) = \text{intensity at time } t \text{ and frequency } \omega.$$

More importantly, integrating over all time or over all frequencies will yield the intensity per unit frequency or the instantaneous intensity respectively:

$$\int F(t, \omega) dt = |\hat{s}(\omega)|^2, \text{ and}$$

$$\int F(t, \omega) d\omega = |s(t)|^2.$$

The total energy of the signal is then expressed as the integral,

$$\text{Energy}(s) = \int F(t, \omega) d\omega dt.$$

This joint function of time and frequency would be our distribution. Its plot is a surface given as a function of two variables, time and frequency. Our plots are given in density plot format. That is, the darker portions correspond to stronger intensities. These plots for the various example signals are given in their respective sections.

There are a number of time-frequency distributions. The most notable ones are the Wigner-Ville Distribution, the Rihaczek Distribution, the Page Distribution, and the Fourier Spectrogram. We are currently developing a Wavelet Spectrogram, which performs better than the above in that it does not need to iterate over subwindows. Our Wavelet Spectrogram uses the fact that the wavelet transform already possesses time and frequency information. The drawbacks, at the moment, are that the Wavelet Spectrogram does not yield as good a frequency resolution as one would like and that the time resolution is only relative (i.e., one needs to do additional computations to determine real-time values). One advantage of the Wavelet Spectrogram is the computational speed. Another advantage is that the choice of wavelet basis will allow for better frequency resolution.

We illustrate the time-frequency distributions with the Fourier Spectrogram (also known as the windowed Fourier Spectrogram or the time-dependent Fourier Spectrogram) for the signals we created in the previous section. Note the difference in the HFM and LFM signals. It is clear in these illustrations that the frequency is linearly modulated for the LFM signal. It is not so clear that the frequency is hyperbolically modulated for the HFM signal, since the modulation is fuzzy near the end (due to the finiteness of the signal).

The PRN signal is seen to have a fairly uniform distribution within the frequency ranges set by the band limits. This indicates the random number generator is a uniform random number generator (as opposed to a normal random number generator).

Finally, note that the ends for the PUL signals are cleaner than the ends of the CW signals. This is because we use the rectangular window function to create the subwindows for the Fourier transforms. Thus, for the CW signals, we get an abrupt drop-off, whereas the PUL signals yield gradual drop-offs.

To generate the Fourier Spectrograms, we set a subwindow size M (in our case, $M = 128$) and a step-size r ($= 8$). Let $\mathbf{s} = \mathbf{s}[n] = (s(0), s(1), \dots, s(1023))$ be the time-series expression of the signal. Then, the distribution, $F(t, \omega)$, is determined by a Fourier transform:

$$F(t, \omega) = \sum_{m=0}^{M-1} s(t r + m) e^{-2 \pi i m \omega / N},$$

where $t = 0, 1, \dots, \frac{N-M}{r}$ and $\omega = 0, 1, \dots, M-1$. Because of the symmetry in the frequency direction (since our signals, \mathbf{s} , are real-valued in time), we take only the first half of the discrete frequencies: $\omega = 0, 1, \dots, \frac{M}{2}$. This is why the vertical frequency axis ranges from 0 to 65.

Fourier Spectrogram of CW 60 Hz

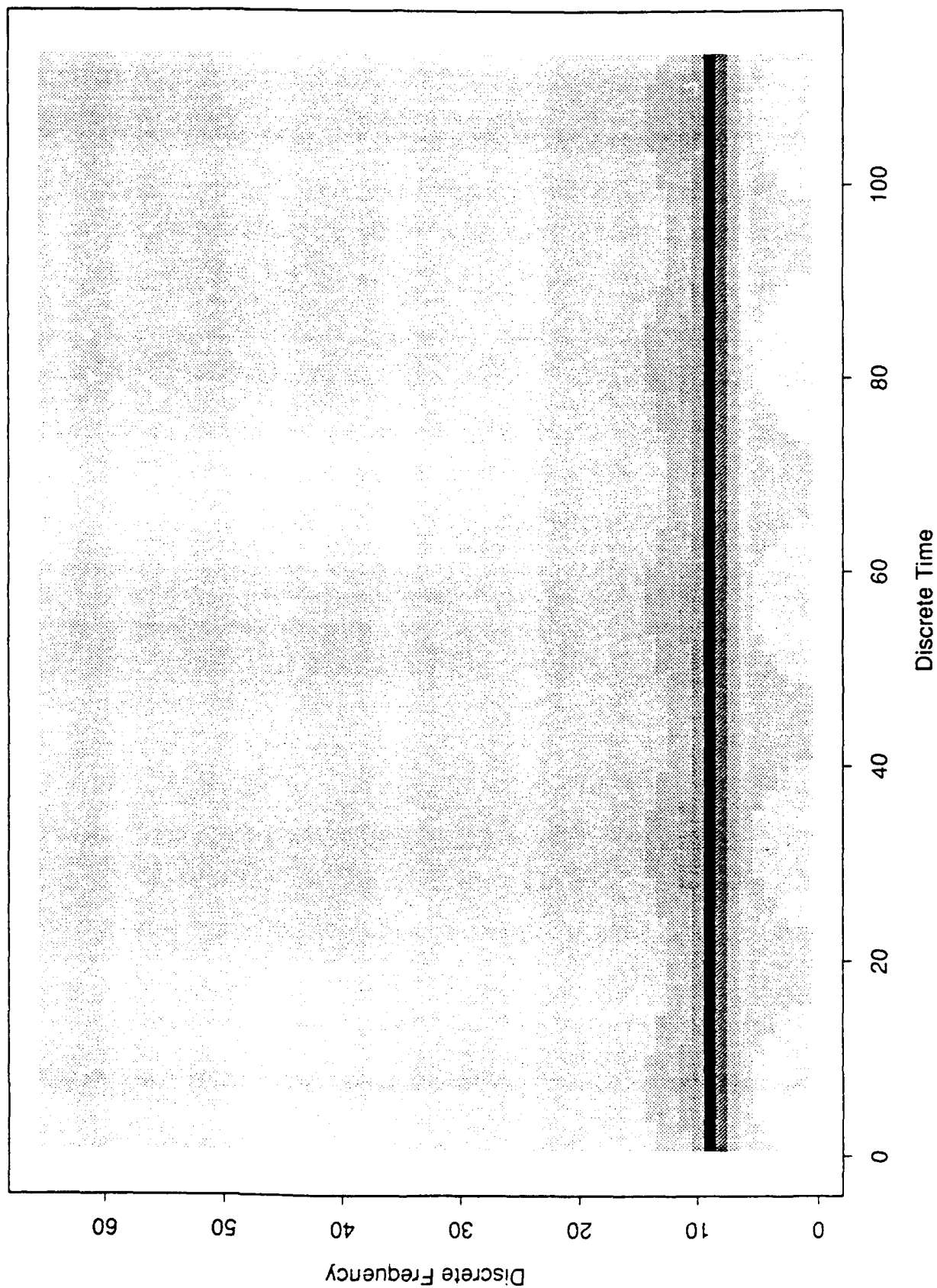


Figure V-19

Fourier Spectrogram of CW 120 Hz

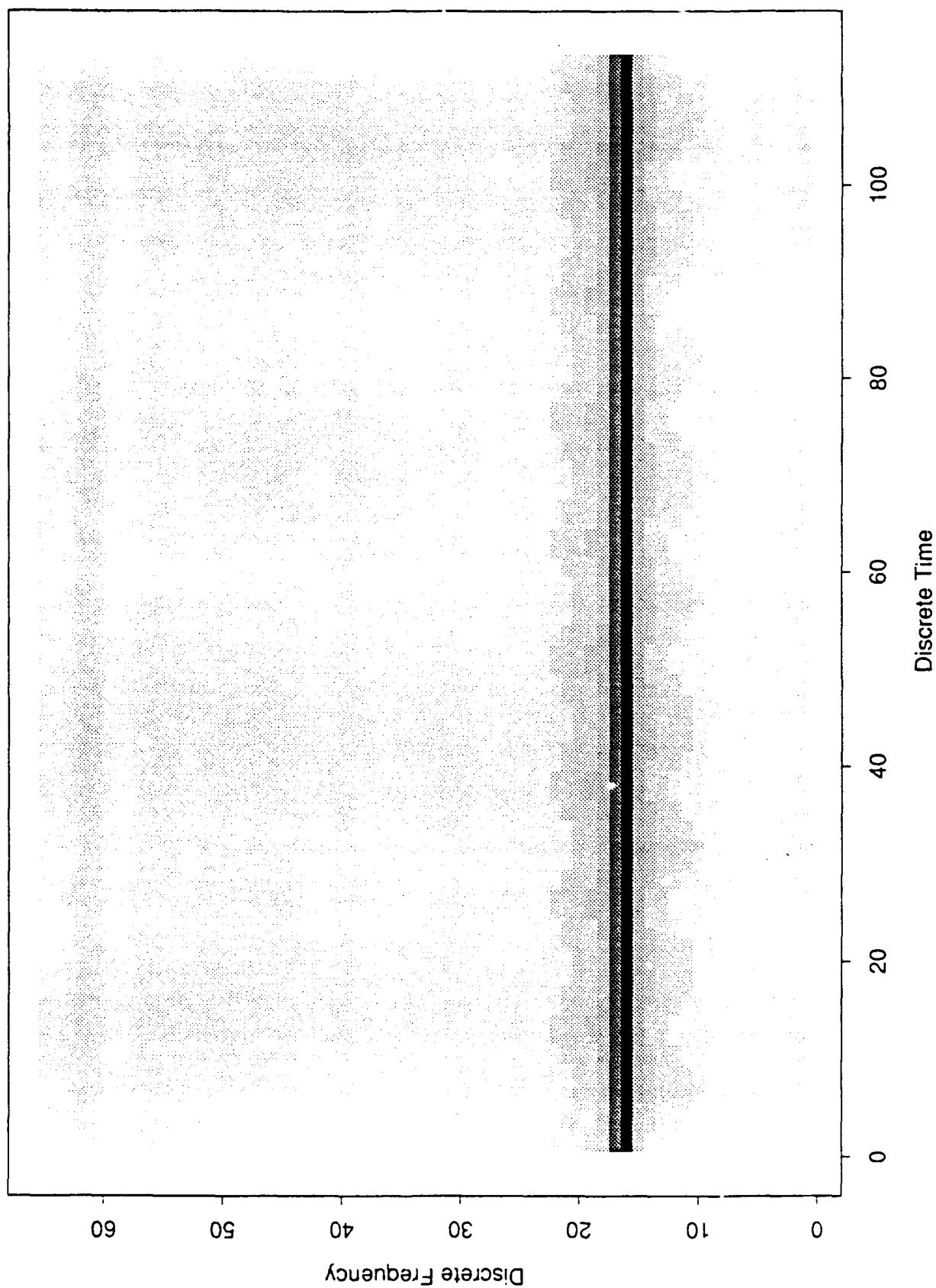


Figure V-20

Fourier Spectrogram of HFM 20-200 Hz

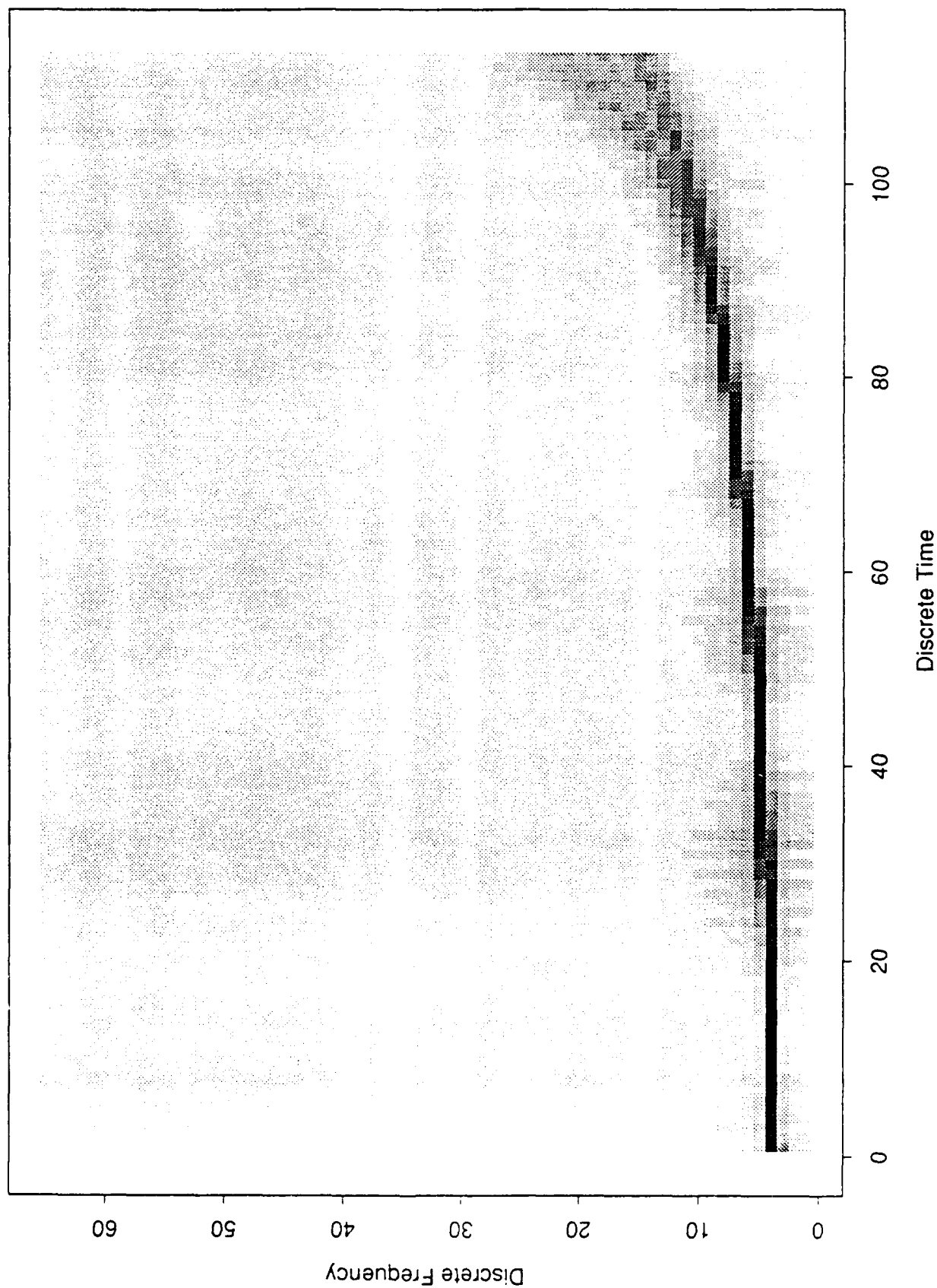


Figure V-21

Fourier Spectrogram of HFM 80-120 Hz

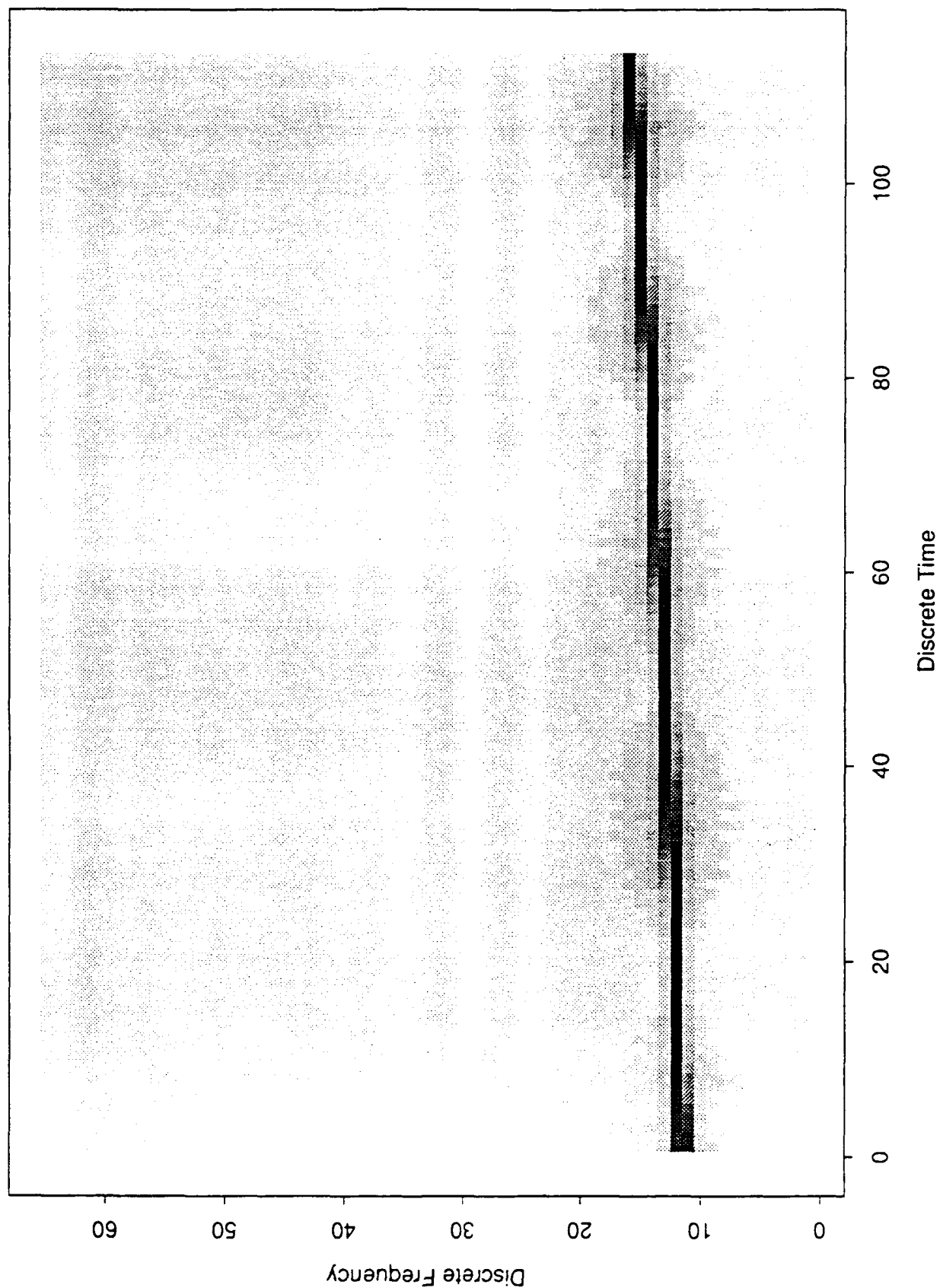


Figure V-22

Fourier Spectrogram of LFM 20-200 Hz

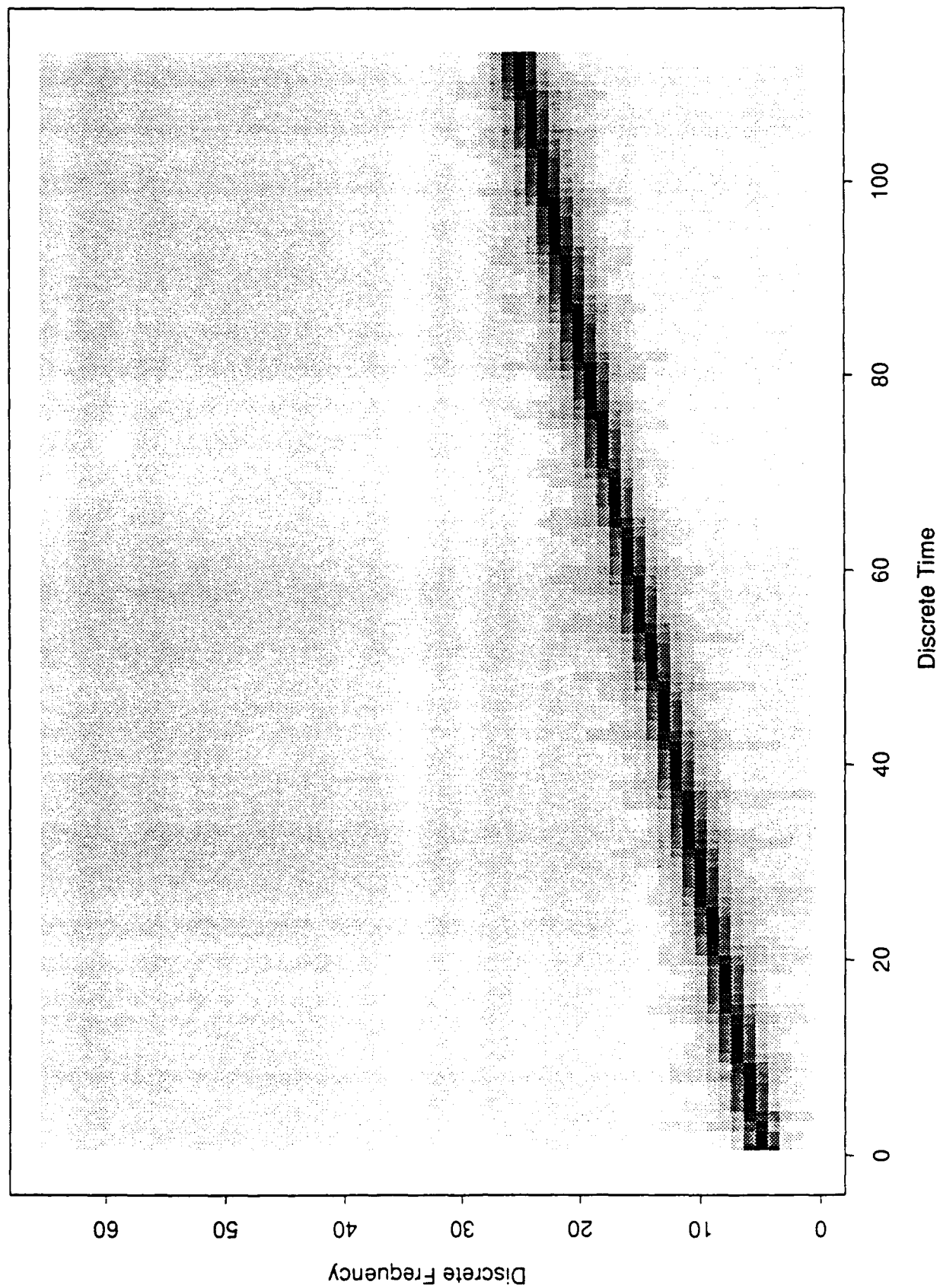


Figure V-23

Fourier Spectrogram of LFM 80-120 Hz

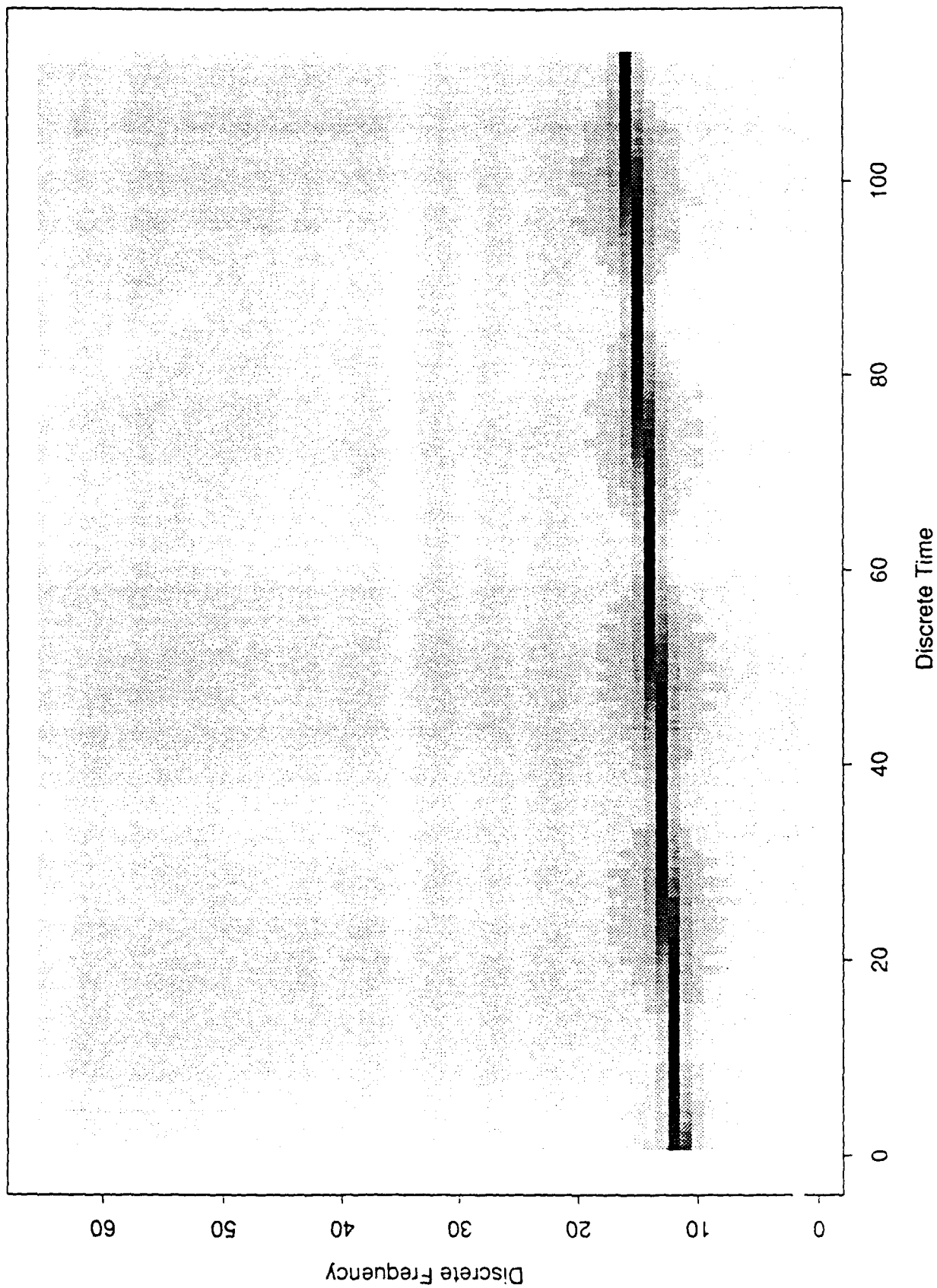


Figure V-24

Fourier Spectrogram of PRN 20-200 Hz

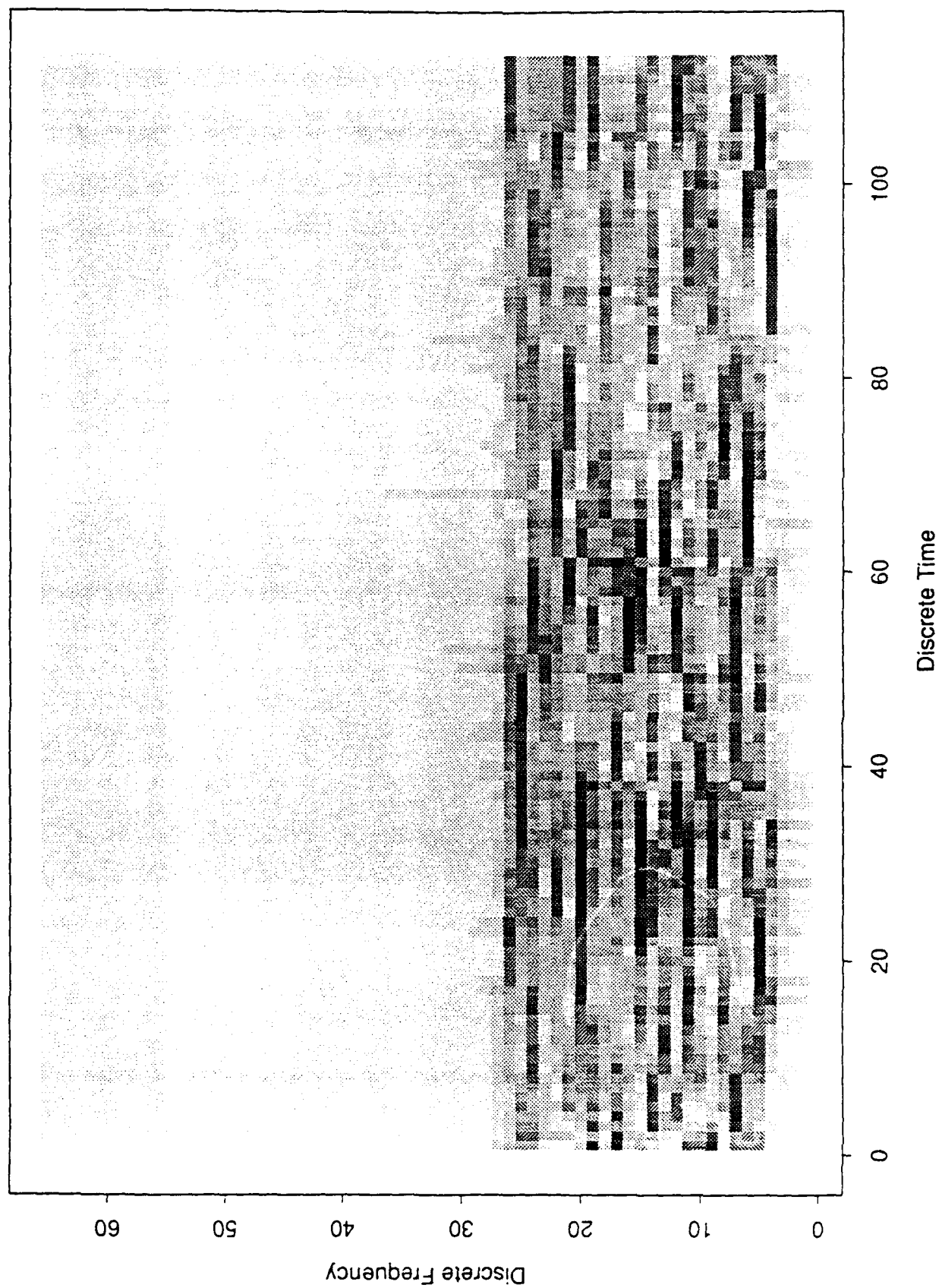


Figure V-25

Fourier Spectrogram of PRN 80-120 Hz

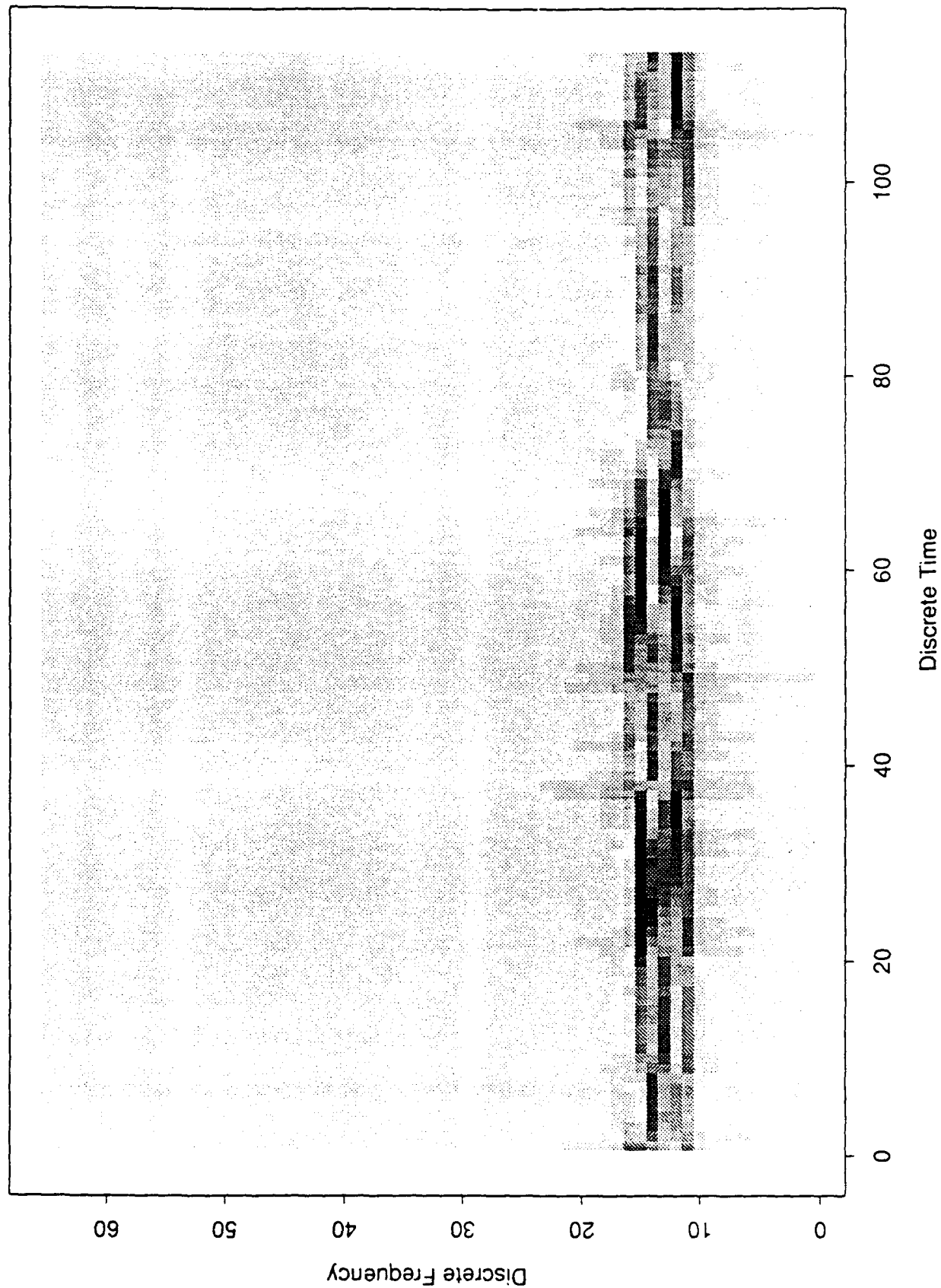


Figure V-26

Fourier Spectrogram of PUL 100 Hz (Short)

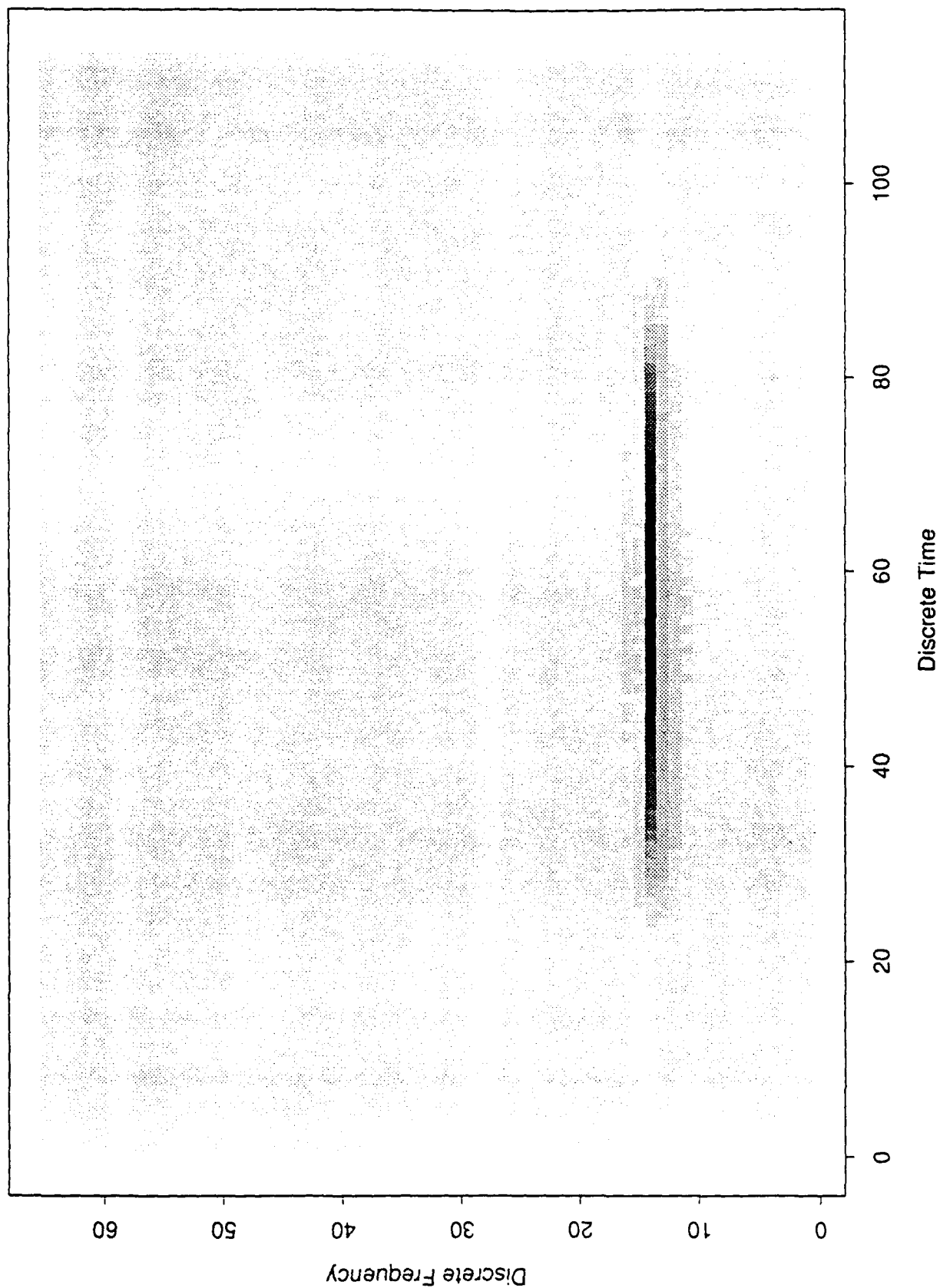


Figure V-27

Fourier Spectrogram of PUL 100 Hz (Long)

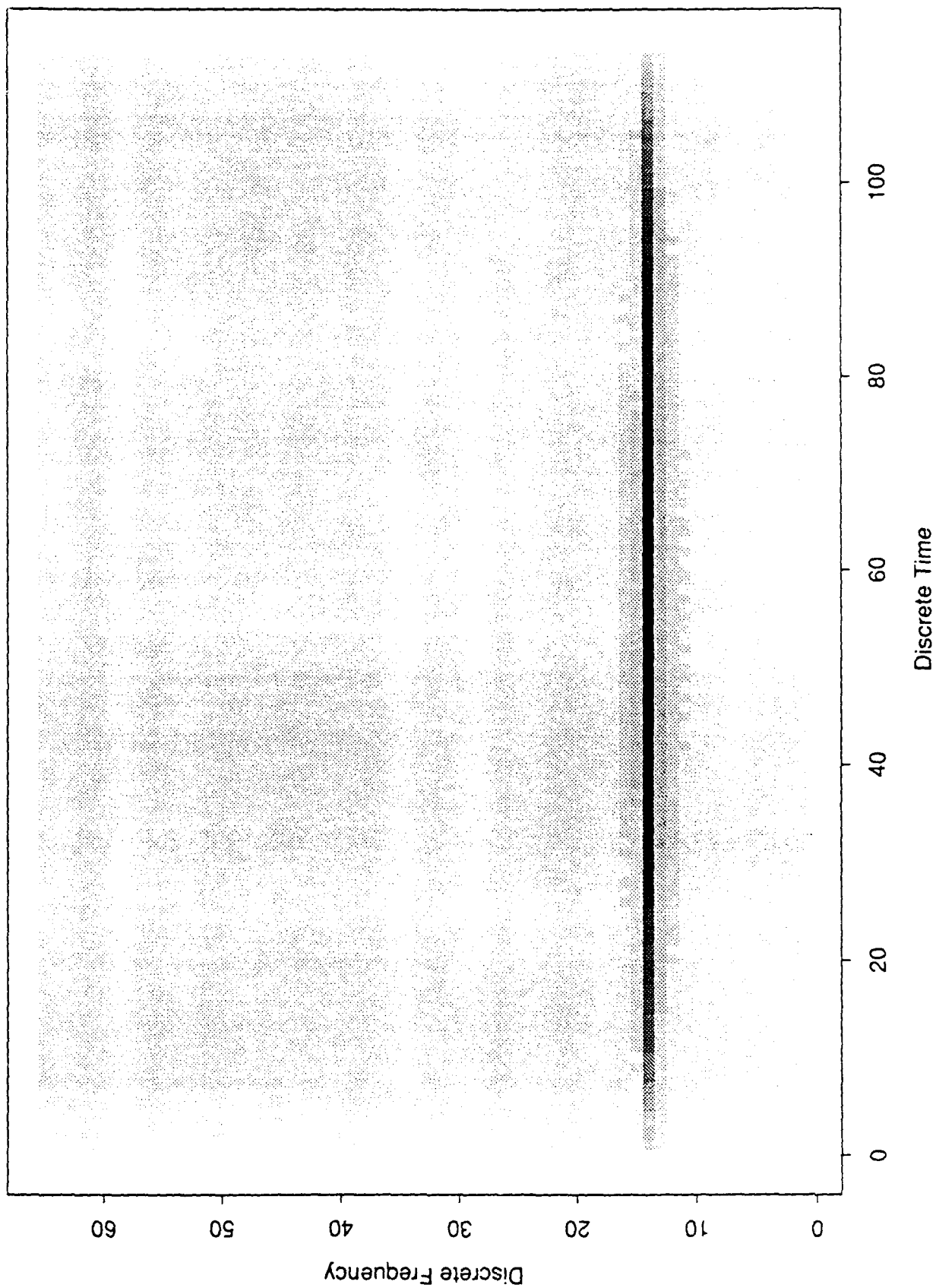


Figure V-28

CHAPTER VI

THE SIMULATION SYSTEM AND A DESCRIPTION OF THE EXPERIMENTS

In this chapter, we describe the transmission simulation system that we built to test the efficacy of the active signals we created. However, the primary emphasis of this chapter is to describe the experiments using the transmission simulation system. The results of the experiments and the data interpretation are given in the following chapter. Section 1 of this chapter will explain each of the modules that composes the simulation system. Section 2 explains our multi-channel detection algorithm, which aims to detect families of signals, classified by possible Doppler shifts or translational shifts. Section 3 presents an example of the compressed Neyman-Pearson detection algorithm (see Chapter IV) implemented on a hyperbolic frequency-modulated signal, CHIP2. This section shows how this signal, CHIP2, changes due to Doppler and bottom-bounce effects. Moreover, Section 3 also shows that the l^2 -closest wavelet basis outperforms all other bases with regard to the compressed N-P detector. Section 4 will describe the experiments using the multi-channel detector on the signal, CHIP2.

1. The Transmission Simulation System

The transmission simulation system is also described in the User's Guide (Reference [q]). The User's Guide is intended as a tutorial, and thus, it does not give much motivation or explanation as to how it was built.

Overall, the transmission simulation system (TSS) consists of eight modules. Each module is a separate routine that simulates a particular phase in the transmission history of the signal. These modules are:

- Signal Generator
- Projector Response
- Transmission (multi-path)
- Reflection
- Doppler

- Reverberation
- Hydrophone Response
- Receiver/Detector

The first module, the signal generator module, creates the signal. This module is not technically part of the TSS. The detector part of the last module is also not technically part of the TSS. These two are actually computed outside of the system. In practice, as currently implemented, we have a separate routine that generates the prototype signal and a separate routine that receives signal-like data and runs the compressed Neyman-Pearson detector, with an appropriate transform as its only user input.

1.1. Signal Generator

The signal generator module creates signals like those described in Chapter V. Such signals begin with norm equal to one (in most cases). They are then amplified so that the signal-to-noise-ratio (SNR) is about 230 dB. (The 230 dB is a default value; the user can set any SNR value.) Setting the SNR level is part of the TSS, hence we put this amplification phase among the simulation modules. The amplification routine is a straightforward linear scaling. In addition to scaling, we also add two windows' worth of noise.

The noise is actually zero noise, meaning that we take the signal – a finite sequence of length $N = 1024$ – and pad this sequence in front and back with 2048 zeros. The output of the signal generator is then a signal of length $5N = 5120$. The reason for the padding is that the transmission module is a finite impulse response filter that needs at least two windows' worth of data. We need to simulate the effects of the transmission also on noise, in addition to the effects on the signal.

1.2. Projector Response

The projector-response module simulates the nonflatness of most projectors. Projectors, because of their physical construction, do not project with equal intensity over all frequencies. The intensity at each frequency can be graphed as a function of the frequency. Such graphs are called frequency response curves.

Most projectors can be built to have a fairly flat response curve over the significant range. However, at the intensity levels of 230 dB SNR, there will be significant distortions, and the response curve will not be flat. Often, the upper frequency end will drop off, relative to the whole frequency spectrum. Since we are engaged in creating low-frequency active signals (i.e., frequency range between 20 Hz to 500 Hz), the drop-off at the high end is still small even at 230 dB SNR. This suggests that the flat response default (which we use) is a suitable default.

The input of this module is the scaled signal of length $5N = 5120$. The output is also of length $5N = 5120$. The routine simply multiplies each entry of the sequence by a scaling factor corresponding to the response curve and returns this value to the same position in the sequence. For the default setting, the scaling factor is set at 1 for all entries.

1.3. Transmission Effects

The next phase after the projector response is the effect simulated by the transmission module. This module simulates the effect of bottom bounce encountered in a shallow-water channel scenario. The result of bottom bounce is that the received signal is a conglomeration of the signal taking various paths. This effect is also known as multi-path.

The module routine is a *finite impulse response filter*, meaning that it takes a finite sequence and returns a finite sequence (possibly of a different length). We will first describe the model upon which the module is based. Then, we will give the equations for the filter.

This module employs the Pecris model for bottom bounce effects, as illustrated in Figure VI-1. When the sonar signal impinges on the bottom, there is attenuation loss because of the change in the signal medium from water to solid. The amount of attenuation loss is dependent on the angle of incidence, α , measured from the surface, as well as the specific gravity of the sea bed and the water pressure at the bottom. However, there is a critical angle, α_c , such that for angles of incidence greater than α_c , the signal will be completely absorbed by the bottom. This sets a maximum number of bounces off the bottom, given as a function of the distance between the source and target, their respective depths, the depth of the water channel, and the critical angle, α_c . There is no attenuation at the air-to-water interface.

The existence of a maximum number of bounces allows us to model this as a Finite Impulse Response (FIR) filter. In this filter, the signal (of size $5N$) is entered, and the output is a

longer duration signal (the size is about $7N$) because the multi-reflected paths are longer. The earlier arriving signal has less attenuation than the later arriving signal. The amount of attenuation is empirically calculated to be about 45 dB/sec, when given the parameters for the density of the sea bed and the respective speeds of sound in water and in the sea bed. The Pecris model and its equations were supplied by DARPA/AT&T Acoustic Warfare research.

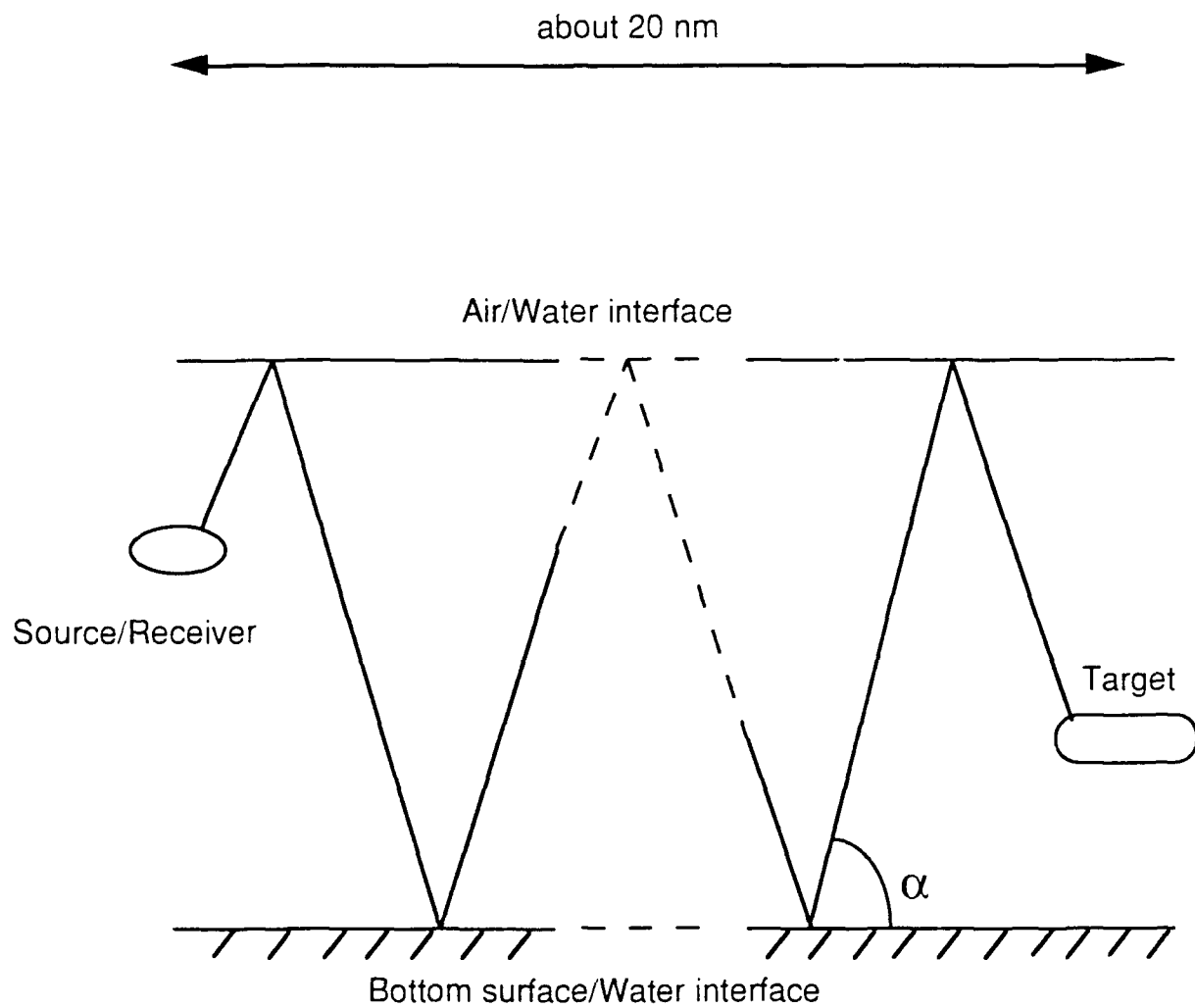
The equation for the filter is

$$s'(n) = \sum_{j=0}^{M-1} s(n-j) h(j),$$

where $h[n] = (h(0), h(1), \dots, h(M-1))$ is the filter, $s[n] = (s(0), s(1), \dots, s(5N-1))$ is the incoming signal, and $s'[n] = (s'(0), s'(1), \dots, s'(3N-1))$ is the output signal. The length of the filter, M , is usually $2N$, because of the channel depth and the source-to-target range. This is why the original signal was padded by two windows' worth of zero noise. To be precise, one should index the output signal, $s'[n]$, as $s'(2N-1), s'(2N), \dots, s'(5N-1)$.

Note that the output is only three windows long. The filter does not shorten the signal. Indeed, it actually lengthens the actual signal, which has length N , to $3N$. The output of the filter is all signal, with the first and last entry, $s'(0)$ and $s'(3N-1)$, equalling zero. This output is then padded again by two windows' worth of zero noise in both the front and the back. Thus, the final output of the module is a signal of length $7N$.

Figure VI-1
Bottom Bounce Model



The model should yield a linear drop in signal strength (measured in dB's) as a function of time. Because the arrival of the reflected signal occurs at discrete moments of time, the FIR filter is finite only at those discrete time moments corresponding to the arrival of the reflected signal, at all other points it is minus infinity. (Note that minus infinity intensity in dB is equal to zero intensity measured as amplitude height.)

This module is used again after the Doppler module. This is to model the returning portion of the signal's trip from source to target to receiver. In the second use of this module, the input-signal length is still $7N$. The output-signal length is then $9N$. This consists of two windows of noise followed by the signal, stretched out over five windows due to this bottom bounce effect, and finally followed by two more windows of noise. The noise window is just zero noise, so the upshot is five windows of signal padded in front and back by two windows' worth of zeros each.

1.4. Reflection

This module uses either the monostatic target strength or the average cosine approximation to the target strength for reflection of signals off targets. This model is also a finite impulse response filter. The input- and output-signal lengths are equal: $7N$. See Reference [o] or [r] for detailed descriptions of the reflection model. Our default input is the monostatic target strength model.

There was no change of this module from the previous presentation of the TSS (see Reference [a]).

1.5. Doppler

The Doppler module is also a finite impulse response filter. It filters via a sinc function (i.e., $\sin(t)/t$ function). The output of the Doppler module may spill the signal outside the window. This occurs when there is a negative Doppler shift (i.e., the target is moving away from the signal source/receiver). Nevertheless, the length of the output signal from this module is equal to the length of the input signal, which in our case is still $7N$.

The Doppler-shift filter is:

$$s_{D, p}(n) = \sqrt{t} \sum_{k=0}^{L-1} s(k) \text{Sinc}(n t - k),$$

where $s[n]$ is the incoming signal of length L , t is the amount of Doppler shift, and $\text{Sinc}(x)$ is the sinc function: $\text{Sinc}(x) = \frac{\sin(\pi x)}{\pi x}$. The effects of Doppler-shifting a signal are shown in several of the time-series plots of Doppler-shifted versions of our example signal, CHIP2.

1.6. Reverberation

This module models reverberation noise as a moving-average stochastic process. At any given time, reverberation from each sample of the signal is occurring at some random intensity.

The moving average equation is also a FIR filter:

$$v(m) = \sum_{k=0}^{M-1} s(k) a(m-k),$$

where M is the length of the signal (in our case, $M = 9N$), $s[k] = (s(0), s(1), \dots, s(M-1))$ is the signal (with the zero paddings in front and back), and $a[k] = (\dots, a(-1), a(0), a(1), a(2), \dots)$ is an infinite sequence of normal random draws with mean = 0.0 and standard deviation $\sigma = \text{input value}$. The sum, $v[m]$, is then the noise. This noise is added to the signal and the resulting sequence is the output of the module.

There is no default value for this module.

1.7. Hydrophone Response

The function and code for this module is identical to the projector-response module.

1.8. Comments

The actual filter codes used in the TSS are based on the equations given in the above subsections. The actual algorithms are modifications of these equations due to computing time and overflow/underflow constraints.

The following chapter includes illustrations of the time-series plot of a signal (CHIP2) affected by bottom bounce and Doppler effects.

2. The Multi-Channel Detector

The multi-channel compressed Neyman-Pearson detector is a system designed to detect the presence of any translate and Doppler shift of a returned signal. We begin with a prototype signal (called "CHIP2" in our experiments) of window size $N = 1024$. This signal is zero-padded at one end to make a signal of size $2N$. This padded signal is used to create a p -level l^2 -closest orthonormal wavelet basis. This is done using the construction described in Theorem III-3.

To create the multi-channel detector, we first generate Doppler shifts of the original signal, from 0 kts to $\pm m$ kts (m stands for maximum). Each distinct Doppler shift, including the zero-shifted signal, corresponds to a *channel* of the multi-channel detector. Each Doppler-shifted signal is also zero-padded, similar to the non-Doppler-shifted signal. We have a separate Doppler-shifting code that produces the Doppler shift of an input signal. This code is similar to the code used in the Doppler module of the TSS.

Now, each channel (i.e., each distinct zero-padded Doppler shift of the signal) is translated by one, N times. This translation is done to model the effect of not capturing the returned signal properly in the receiving window. For each channel and each translate, we compute the wavelet coefficients with respect to a fixed wavelet basis. The wavelet basis is now the detector in the sense of the compressed Neyman-Pearson detector (see Chapter IV).

The wavelet basis is generated by the wavelet function that is l^2 -closest to the original signal. In some of our experiments, we also used wavelet bases generated by wavelet functions that are l^2 -closest to the Doppler shifts of the original signal, as well as multi-path versions of the original

Fix a compression size $M < N$. This number is the size of the subset of all the wavelet coefficients that we will use in the compressed Neyman-Pearson detector. For this fixed M , we choose the M largest weights of the wavelet coefficients for each channel and each translate. This will determine the subset of the wavelet coefficients used in the compressed detector.

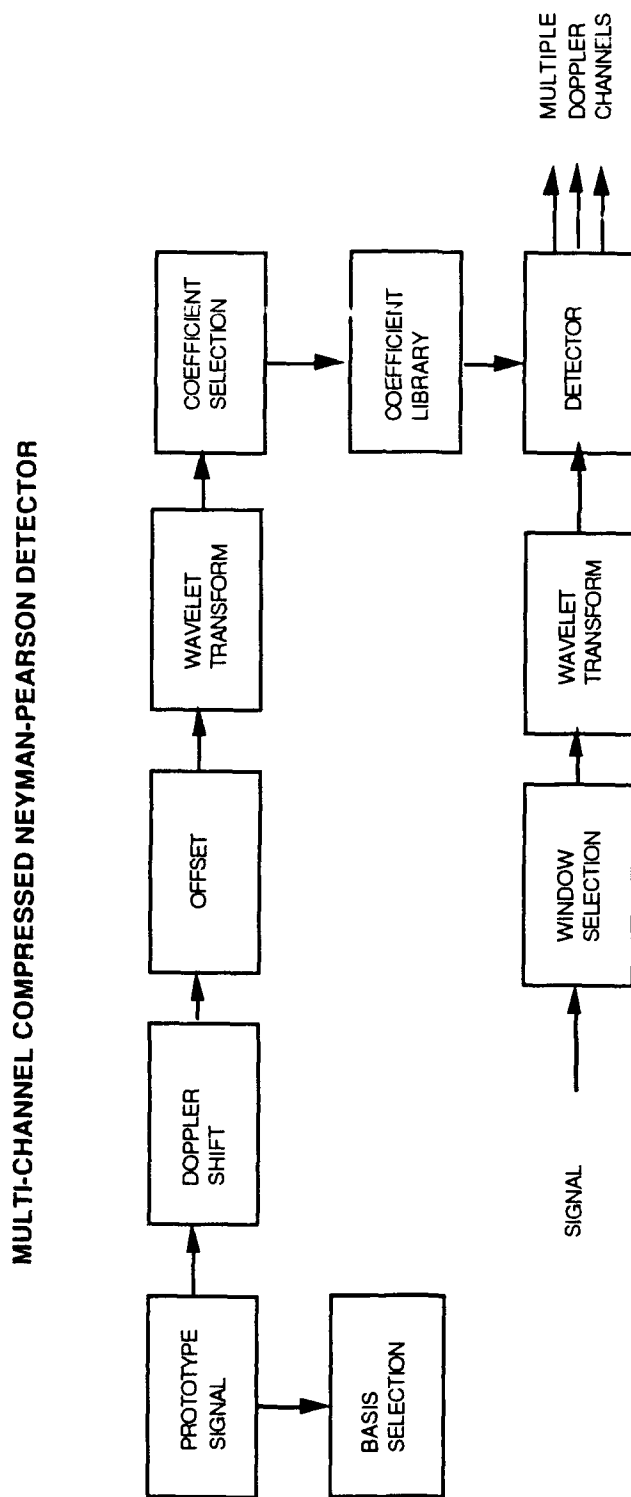
Because of the recursive nature of the wavelets, all these data are actually quite easy to store. It is not essential to store, for example, all translates of each channel; the first 2^p translates (including the zero translate) are sufficient to supply the data for the N translates.

We now receive a signal. In other words, we send a prototype signal (e.g., a CW or an LFM signal) through the TSS and take the output of the simulator as the return signal. This returned signal will look significantly different from the prototype signal that we send out (or rather, into the simulation system). It may also be the case that the received signal is just noise; the prototype signal is not present in that window.

Take the wavelet transform of the returned signal, using the same wavelet basis as the one chosen to create the detector. Use the subset determined above to check for the presence of the prototype signal in the received signal. We then check each channel to determine whether Doppler shifting has occurred in the signal.

A diagram of the multi-channel detector methodology is given in Figure VI-2.

Figure VI-2
The Multi-Channel Detector System



When using the multi-channel detector on the output of the TSS, the detector will scan through the nine window-lengths, yielding $8N$ data points. (It is not necessary to scan the very last point of the ninth window, so there are only 8 whole windows to consider.) A typical output of the multi-channel detector will be described at the end of the following example section.

3. The Example Signal

We created a signal called CHIP2. This signal is the concatenation of five HFM signals. The sampling frequency is 1000 Hz, and the window size is 1024; so the signal has a duration of 1.024 seconds. The HFM signals are:

- The first 0.27 sec. is HFM ranging from 80 Hz to 120 Hz.
- The second 0.24 sec. is HFM ranging from 120 Hz to 180 Hz.
- The third 0.24 sec. is HFM ranging from 180 Hz to 100 Hz.
- The fourth 0.10 sec. is HFM ranging from 100 Hz to 150 Hz.
- The fifth and last 0.17 sec. is HFM ranging from 150 Hz to 80 Hz.

See Figure VI-3 for a time-series plot of CHIP2. (Figure VI-3 and all following figures are given after the text.)

In using the basic compressed Neyman-Pearson detector, we create the l^2 -closest 3-level wavelet basis based on the signal. See Figure VI-4 for the time-series plot of the l^2 -closest 3rd-level wavelet function. Figure VI-5 shows the difference between the CHIP2 signal and the l^2 -closest 3rd-level wavelet function. Figure VI-6 shows the time-series plots of the wavelet functions at all levels: first, second, third, and the extra third-level wavelet functions.

We also sent this signal through our transmission simulation system, simulating a +5 kt Doppler, a shallow-channel bottom bounce effect (multi-path), and the combination of both: +5 kt Doppler and the effect of multi-path. Figure VI-7 shows the time-series plots of CHIP2 under these scenarios, compared to the prototype.

4. The Experiments

4.1. The Multi-Channel Detector Experiment

We were requested to conduct experiments to determine whether the multi-channel detector can be enhanced by using p -level wavelet bases generated by p^{th} -level wavelet functions that are l^2 -closest to Doppler shifts or multi-bounced versions of the prototype signal. We ran the multi-channel detector using different wavelet bases to see if the appropriate basis will have a better chance of detecting the expected return signal, compared to other wavelet basis. A thorough discussion of the experimental results is given in the following chapter. This subsection will explain the experimental procedures. The results of the tests are reported in the following chapter.

The first step was to construct the detection basis for the different Doppler shifts of the signal, CHIP2. To do this, we ran the signal through the TSS, assuming only Doppler of 0 and +5 kts. The return signals were then used to generate the l^2 -closest 3-level wavelet bases. This forms the standard and the Doppler-only detector.

The next step was to construct the detection basis to match a multi-path signal (i.e., a signal affected by bottom bounce). This signal is constructed by sending the prototype signal through the TSS with default setting on every module except the multi-path. The parameters for the multi-path are:

- Sea Depth = 2000 ft,
- Signal/Receiver Source Depth = 1000 ft,
- Target Depth = 1000 ft,
- Source-to-Target Range = 30 nm.

These are also our standard settings for the multi-path module.

We proceed as with the Doppler-only case and generate the l^2 -closest 3-level wavelet basis to the multi-path signal.

The third step was to build a detection basis to match a Doppler-shifted, multi-path signal. The Doppler shift is +5 kts, and the multi-path parameters are the same as above. Again, we generate the l^2 -closest 3-level wavelet basis for this signal.

We now run the experiment, sending a signal through the TSS, with and without Doppler, and with and without multi-path. The Doppler range for the experimental signals are 0 kts, ± 5 kts, ± 10 kts. The multi-path is set to the above parameters. Recall that the return signal consists of $9N = 9216$ data points. The multi-channel detector assumes Doppler speeds of 0 kts, ± 2 kts, ± 4 kts, ± 6 kts, ± 8 kts, and ± 10 kts - making up the eleven channels of the detector.

As mentioned in the above section on the multi-channel detector, the output of the detector is $8N = 8192$ data point per channel. It is impossible for the printer to get the resolution required for eleven channels of 8192 data points, so we resample the data points with a peak-picking method.

The first step is to set a threshold so that all data points below the threshold are set to zero. Next, we partition the 8192 data points into groups of 10 (in the order they were originally presented). In each of the groups of 10, we pick the largest value (i.e., peak-picked) and use it as the representative for that group of 10. Thus, we get 819 peak-picked data points. These points are then plotted on a *grass plot*. A grass plot is a plot of a sequence, cut below by the threshold.

We also conducted tests to show the efficacy of l^2 -closest wavelet bases for compressed Neyman-Pearson detection. We compared the l^2 -closest wavelet basis to the real Shannon wavelet basis, the Fourier basis, the Daubechies' D_4 wavelet basis, and the delta (time) basis. The tests were to determine how much dB loss were incurred by compressing the detecting basis for the various bases. We ran these tests for the CHIP2 signal sent through the TSS with the following settings:

- Only Doppler, at 0 kts, ± 2 kts, ± 4 kts
- Only Multi-Path, at standard parameters
- Doppler and Multi-path,
- Translated signal

4.2. Compression Loss versus Compression Ratio Tests

To implement the compressed Neyman-Pearson (N-P) detector, we need to find bases (in the sense of vector space bases) that do not degrade much due to compression. Indeed, the notion of a basis is equivalent to the detector. We show, in the following chapter, that the l^2 -closest (to the prototype signal CHIP2) wavelet basis significantly outperforms all other bases. However, we do not have mathematical proof that this basis is optimal for compressed detection. Additionally, we do not have proof that the compressed N-P detector is near optimal (see Chapter VIII, Section 3).

The N-P detector is optimal (see Chapter IV), but it is slow. Compressing the data increases the computation speed, the drawback being some signal loss. This can be measured as a dB loss, called the degradation due to compression. For different bases, the amount of degradation loss differs for an equal amount of compression.

The bases under comparison are the 3-level l^2 -closest wavelet basis, the 3-level real Shannon wavelet basis, the 3-level Daubechies D_4 wavelet basis, the Fourier basis, and the delta basis. The Fourier basis is actually the absolute value of the Fourier transform. The l^2 -closest wavelet basis is generated from the 3rd-level wavelet function, which is l^2 -closest to the prototype signal, CHIP2.

We test these bases for degradation under various scenarios; we consider detecting the prototype, translates of the prototype, and Doppler shifts of the prototype. Not all bases will be tested under all these scenarios. For example, there is no need to test the Fourier basis under translations since the absolute value of the Fourier transform is translation invariant.

To quantitatively measure how good a particular basis is for compressed Neyman-Pearson, we compute the dB loss due to compression. Because the Neyman-Pearson detector is basis-independent, all bases will give optimal detection if used without compression. What we want to measure, then, is the entropy of the transform.

Let \mathcal{B} be a particular orthonormal basis (e.g., the l^2 -closest wavelet basis, real Shannon wavelet basis) into which we want to transform the signal. If

$$\mathbf{s} = s[n] = (s(0), s(1), \dots, s(N-1))$$

is the signal in the time basis, and

$$\underline{s} = \underline{s}[n] = (\underline{s}(0), \underline{s}(1), \dots, \underline{s}(N - 1))$$

is the signal in basis \mathcal{B} , we rearrange the absolute value of the coefficients,

$$\{ |\underline{s}(0)|, |\underline{s}(1)|, \dots, |\underline{s}(N - 1)| \},$$

in decreasing order so that choosing the M largest weights is equivalent to taking the first M coefficients; these are then the elements of A . Assume now that the coefficients are reordered. Using the equations from Chapter IV, we compute the entropy:

$$Z^A = \left(\sum_{k=0}^{M-1} |\underline{s}(k)|^2 \right)^{\frac{1}{2}}$$

and then to determine a dB loss, we take the logarithm:

$$D^A = 20 \log_{10} Z^A,$$

which is now measured in dBs.

In our tests, we set up the runs so that for a given compression ratio (M / N), the code automatically finds the optimal subset, A , of cardinality M . The output is then a dB loss for every value of M , from 1 to N . The graph of dB loss versus compression ratio is a monotonically increasing function. Because of the semi-logarithmic scale of the axes, the graphs do not look monotone increasing for small compression ratios, although they are.

The results show quite clearly that the l^2 -closest wavelet basis stands above the other bases for compressed N-P detection purposes. Chapter VII shows these results.

A-Trace for CHIPS 2 (1.02 seconds at 1000 samples / second)

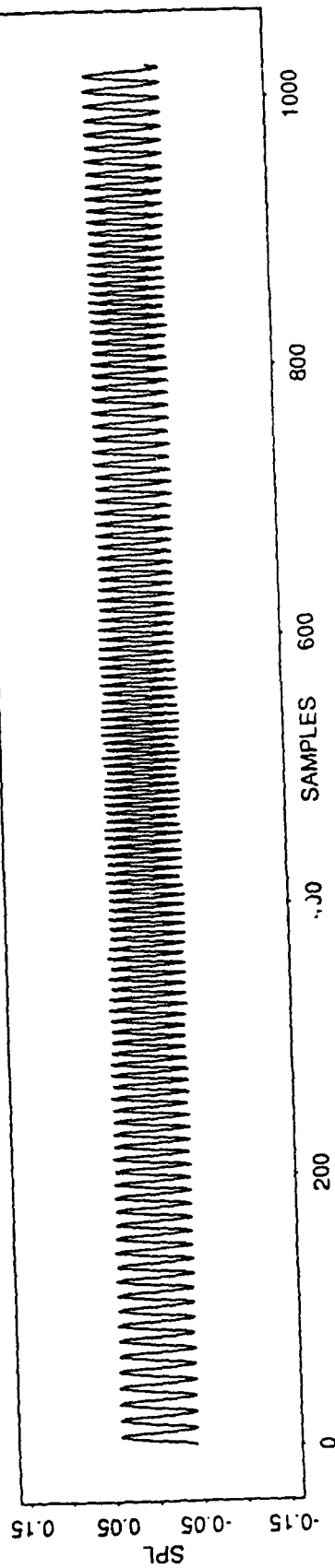


Figure VI-3

A-Trace for Closest Level 3 Wavelet of CHIPS 2 (1.02 seconds at 1000 samples / second)

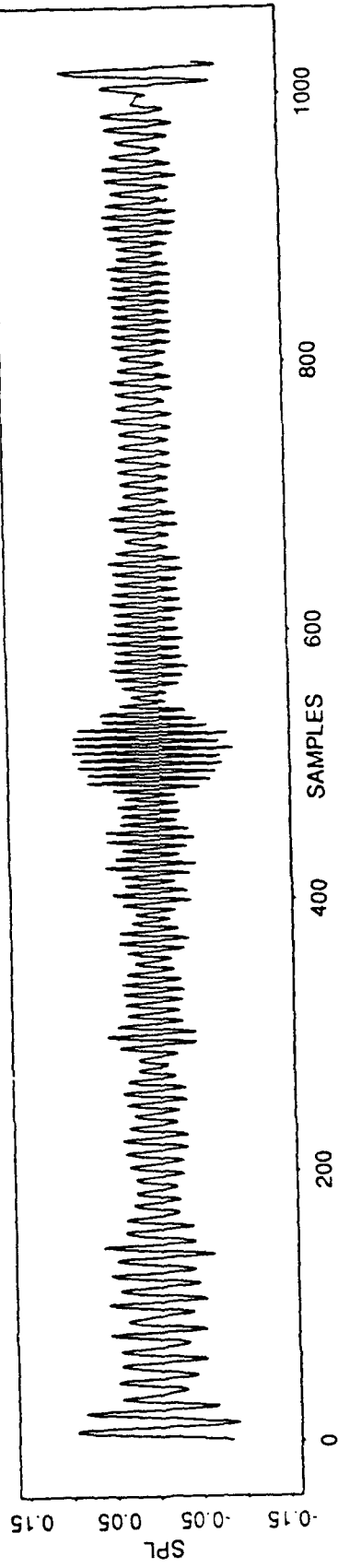


Figure VI-4

Difference Between the Two Signals

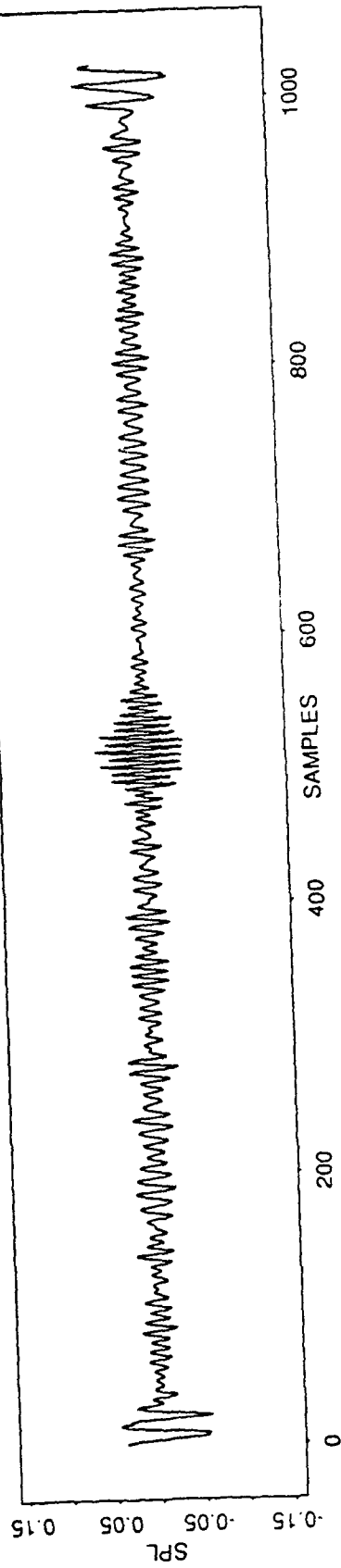
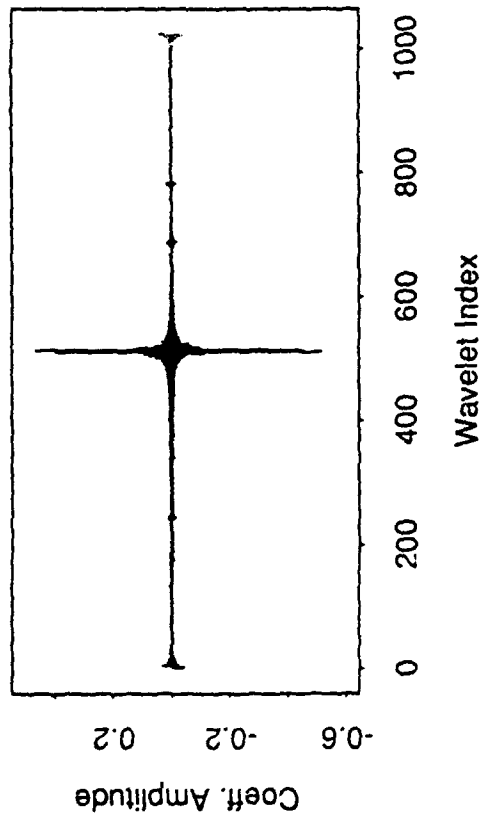


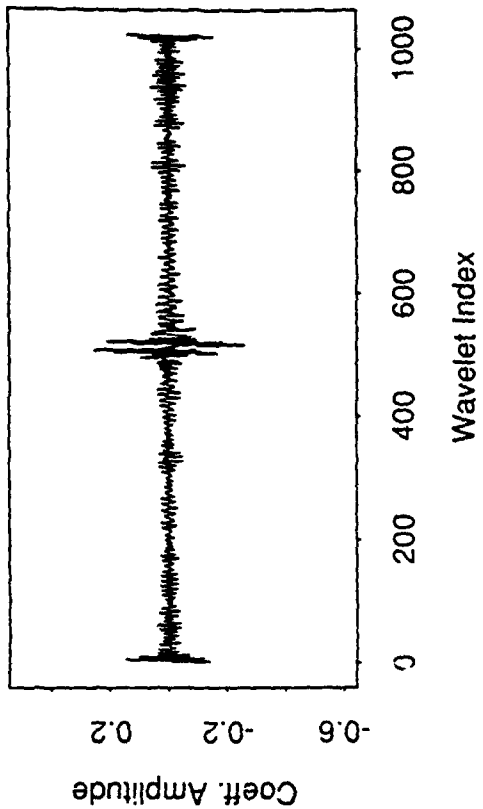
Figure VI-5

Wavelet Basis Functions CHIPS 2

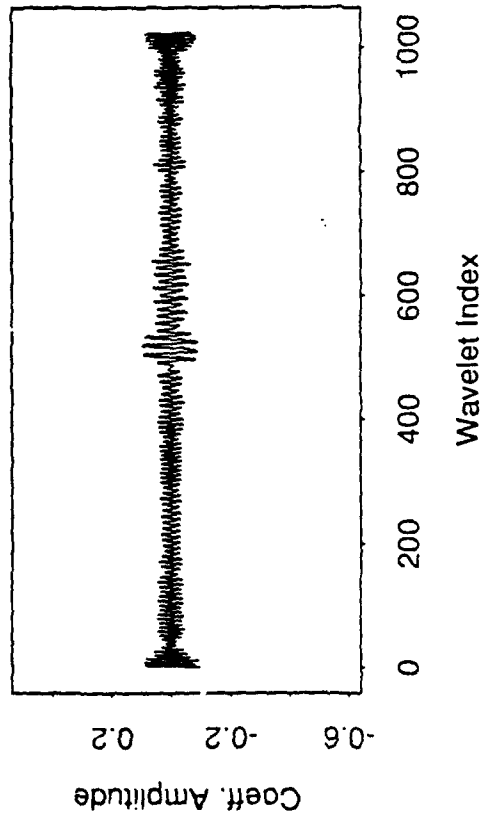
1st-level



2nd-level



3rd-level



Extra 3rd-level

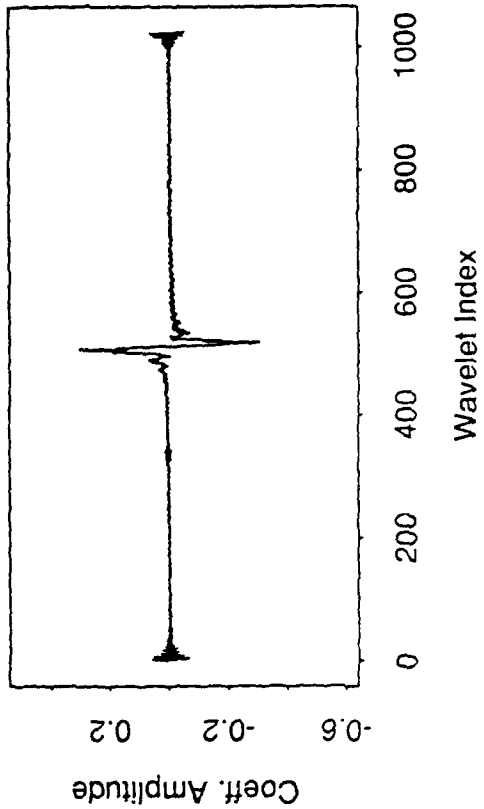
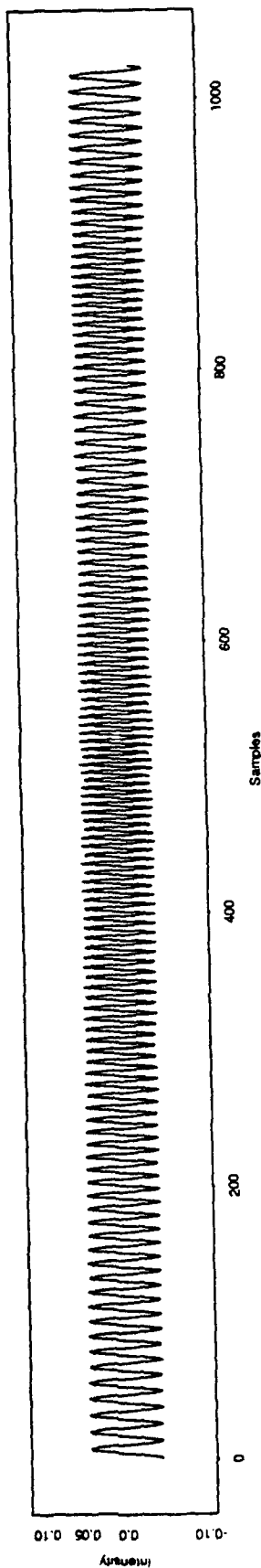
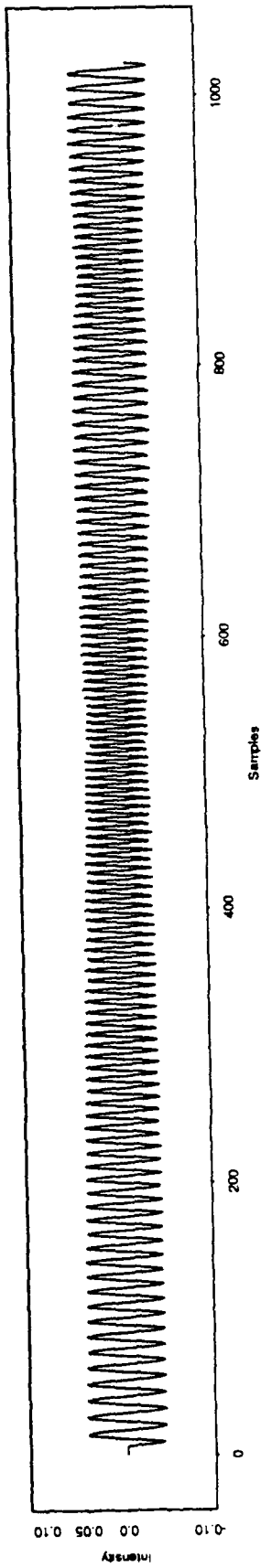


Figure VI-6

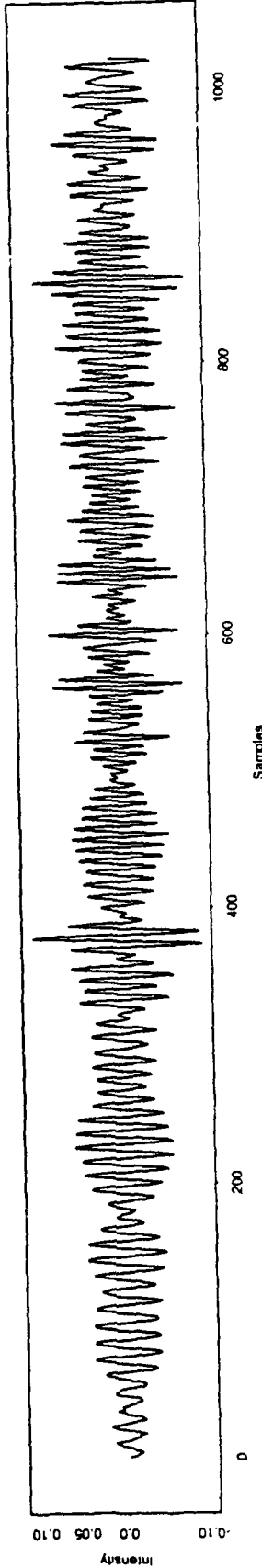
CHIP2



CHIP2 with Doppler Shift of +5 Knots



CHIP2 with Multi-Path Transmission Loss



CHIP2 with Doppler Shift of +5 Knots and Multi-Path Transmission Loss

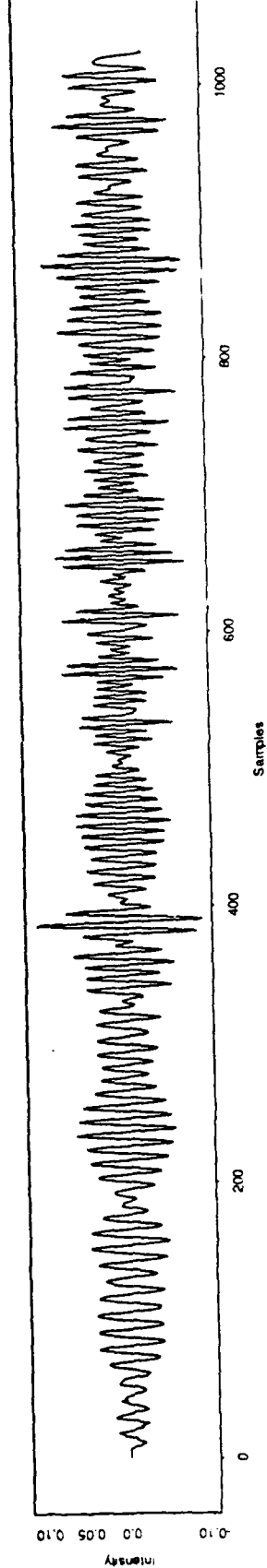


Figure VI-7

CHAPTER VII

SUMMARY OF THE EXPERIMENTAL RESULTS

We present and discuss the results of the experiments and tests described in the previous chapter. Our main conclusion for the multi-channel detector experiment is that the results are inconclusive. The conclusions for the compression loss-versus-compression ratio tests are more conclusive; they do point out that l^2 -closest wavelet bases perform better than other orthonormal bases with regard to the compressed Neyman-Pearson detector. The test results are illustrated by graphs. The multi-channel detector experiment results are also graphically illustrated. Section 1 presents the results of the multi-channel detector experiment, and Section 2 presents the results of the compression loss-versus-compression ratio tests.

1. The Multi-Channel Detector Experiment

The results of the multi-channel detector experiment are inconclusive. We wanted to know whether the multi-channel detector could be enhanced by using the Doppler shift of the signal (CHIP2) as the detecting prototype signal (see Chapter VI, Section 4.1 for details). The results show no appreciable improvement using the l^2 -closest (to the Doppler shift of the signal) wavelet basis, compared to the l^2 -closest (to the prototype signal) wavelet basis. However, the inconclusive result should not be misconstrued as that the detector is defective. The results *do* show that the detector does work. This is evident in the noticeable spikes in the grass plots. It is just that our intent was to see whether the detector can be enhanced by choosing a more appropriate detection basis. Moreover, the result does not disprove the efficacy of tailoring the detecting basis to the expected return signal.

The explanation for the inconclusive result is straightforward: the signal, CHIP2, is relatively Doppler-invariant. As mentioned in Chapter V, HFM signals are invariant under Doppler shifts. Since CHIP2 is constructed by concatenating a series of HFM signals, it, too, is Doppler invariant. Compare the time-series plots of the prototype signal and a +5 kt Doppler shift of the signal (see Figure VI-7). The two plots are almost identical. The time-series of the shallow-channel multi-path effects (with and without +5 kt Doppler) are also given in Figure VI-7; note the differences between the signals with and without multi-path.

We also plot the T-F distributions of these four return signals, using the windowed Fourier Spectrogram, as described in Section 3 of Chapter V (see Figures VII-1, VII-2, VII-3, and VII-4). The distributions verify again the similarities of the Doppler shifts to the unshifted versions.

The results of the multi-channel detector are read from the grass plots. Figures VII-5, VII-6, VII-7, and VII-8 show some grass plots from the experiment. These four plots all have a compression ratio equal to 0.01. For clarity, the grass plots do not include the first window, which is comparing noise, nor the fifth through eighth windows, which include the low end of the signal in addition to noise. We have test results using various possible combinations of detector signal (CHIP2, CHIP2 with Doppler, CHIP2 with multi-path, CHIP2 with Doppler and multi-path), return signal (similar to detector signal choices), and number of weights, and we also compared CHIP2 results with a pulse result. For brevity, we decided not to include all these results.

In the grass plots (those from the figures shown in this report and others), there is a noticeable peak corresponding to the correct matching of the return signal with the detecting signal. Some of the plots (mainly those in which the detecting basis is generated from the multi-path version of the signal or the return signal has been sent through the multi-path module) show that the main peak is not as definite. This suggests that the basis choice (hence, the signal choice) is not a good choice. It is in the similarity between the various channels that demonstrates the inconclusiveness of the whole experiment.

Let us study the plots in Figures VII-5 through VII-7. Figure VII-5 shows the result of attempting to detect a non-Doppler-shifted single-path return CHIP2 signal with a detector basis built from the CHIP2 signal. The peak occurs at the beginning of the third window, which is the first "signal" window. Note the similarities between the different channels. This is due to the fact that CHIP2 is Doppler-invariant; hence, the detector bases for the channels will be very similar to each other. Indeed, in all of the four figures (and many others not illustrated in this report) variations between channels are minimal, due to the Doppler invariance of CHIP2.

The major differences occur when comparing different detector bases, most noticeably when we use a CHIP2 with multi-path signal to generate the detector basis. The grass plot of Figure VII-6 (which uses CHIP2 with multi-path to generate the detector basis) starkly contrasts with that of Figure VII-5. The lack of a noticeable peak in Figure VII-6 shows that such a basis is not effective.

Unfortunately, the detector basis generated by CHIP2 with multi-path is equally ineffective in attempting to detect a CHIP2 with multi-path return signal. This is seen in Figure VII-7. Note again the lack of a distinctive peak. Our results indicate that the l^2 -closest wavelet basis built out of CHIP2 with multi-path is not a good detector basis.

Figure VII-8 shows a prominent peak, despite attempting to detect a non-Doppler-shifted signal. Again, this illustrates the Doppler invariance of CHIP2.

In general, our results show that detecting multi-path using a detector basis built from either CHIP2, CHIP2 with Doppler, or CHIP2 with multi-path was ineffective. Not one of the plots show any prominent peaks, and even increasing the number of weights did not improve detection discrimination. Compare Figures VII-7, VII-9, and VII-10. This lack of distinction also occurs when CHIP2 with multi-path is used to build the detector basis. Figures VII-11 and VII-12 illustrate these grass plots.

We attempted using the multi-channel detector on other signals. One other signal choice is the PULSE100 (short) signal. The results were also not very encouraging (see Figure VII-13). The Doppler Ambiguity Displays of pulse signals (see Figures V-17 and V-18) show that the effects of Doppler are appreciable only for shifts corresponding to speeds greater than ± 10 kts. Since our multi-channel detector output for the PULSE100 (short) is limited between -10 kts to $+10$ kts, this may be the reason for the lack of visual differences.

Our conclusion is that an appropriate choice for the detector basis is not necessarily the l^2 -closest wavelet basis to the expected return signal. It is also possible that certain return signals will be difficult to detect, no matter what the detector basis is. We did not try using more levels in our detector basis, which might have enhanced detection. (This may be one avenue of short-term future research.) The multi-channel detector experiments were all conducted using 3-level wavelet bases. We know higher-level wavelet bases yield better compressed detection capabilities. At this stage, we do not know whether the cause for the poor performance is in the choice for the detection basis or in something more fundamental. We feel the accuracy of the simulation system (TSS) is sufficient to warrant dismissing it from consideration as a possible cause for the poor performance of the multi-channel detector.

Fourier Spectrogram of CHIP2

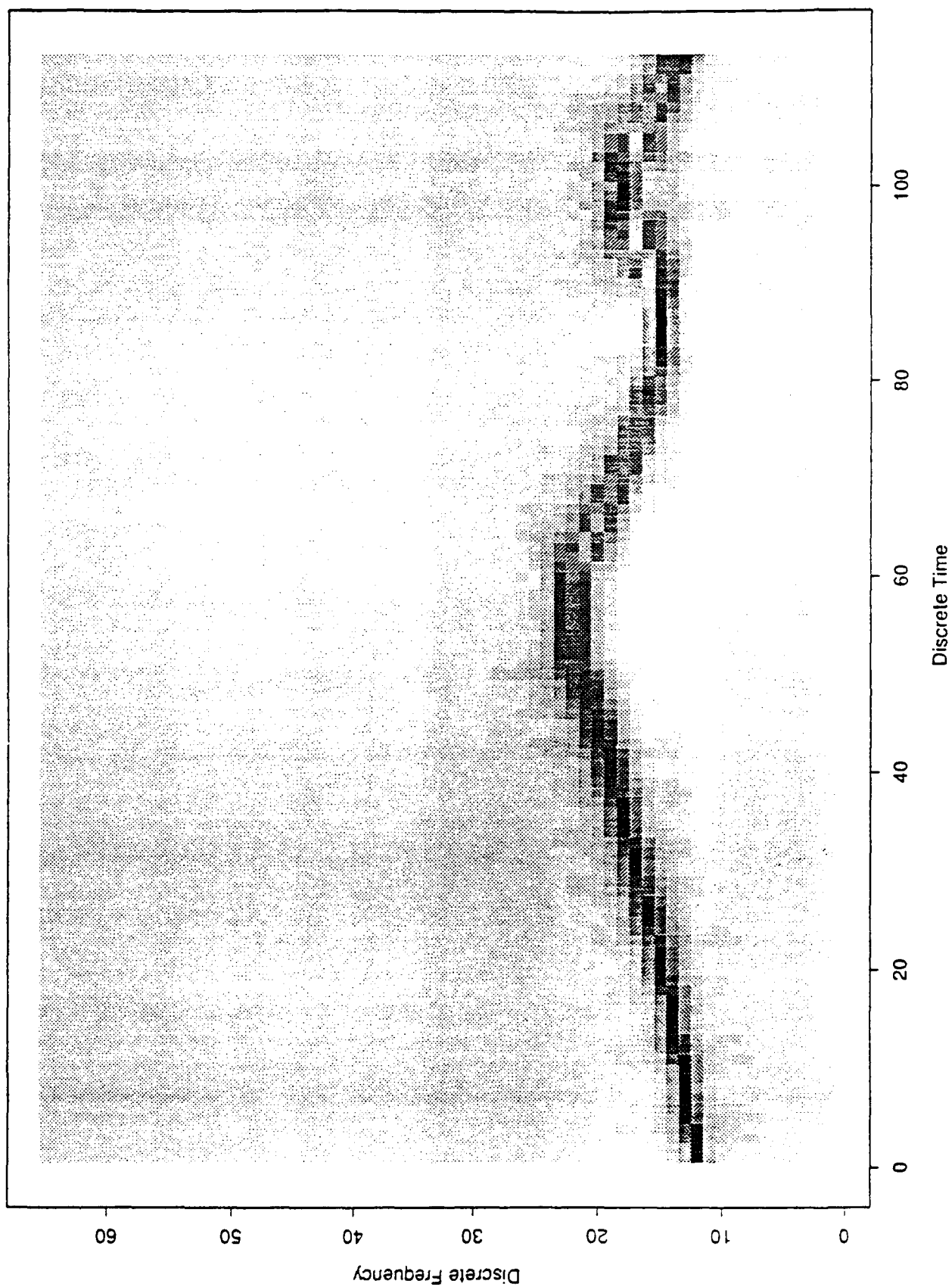


Figure VII-1

Fourier Spectrogram of +5 kts Doppler Shift of CHIP2

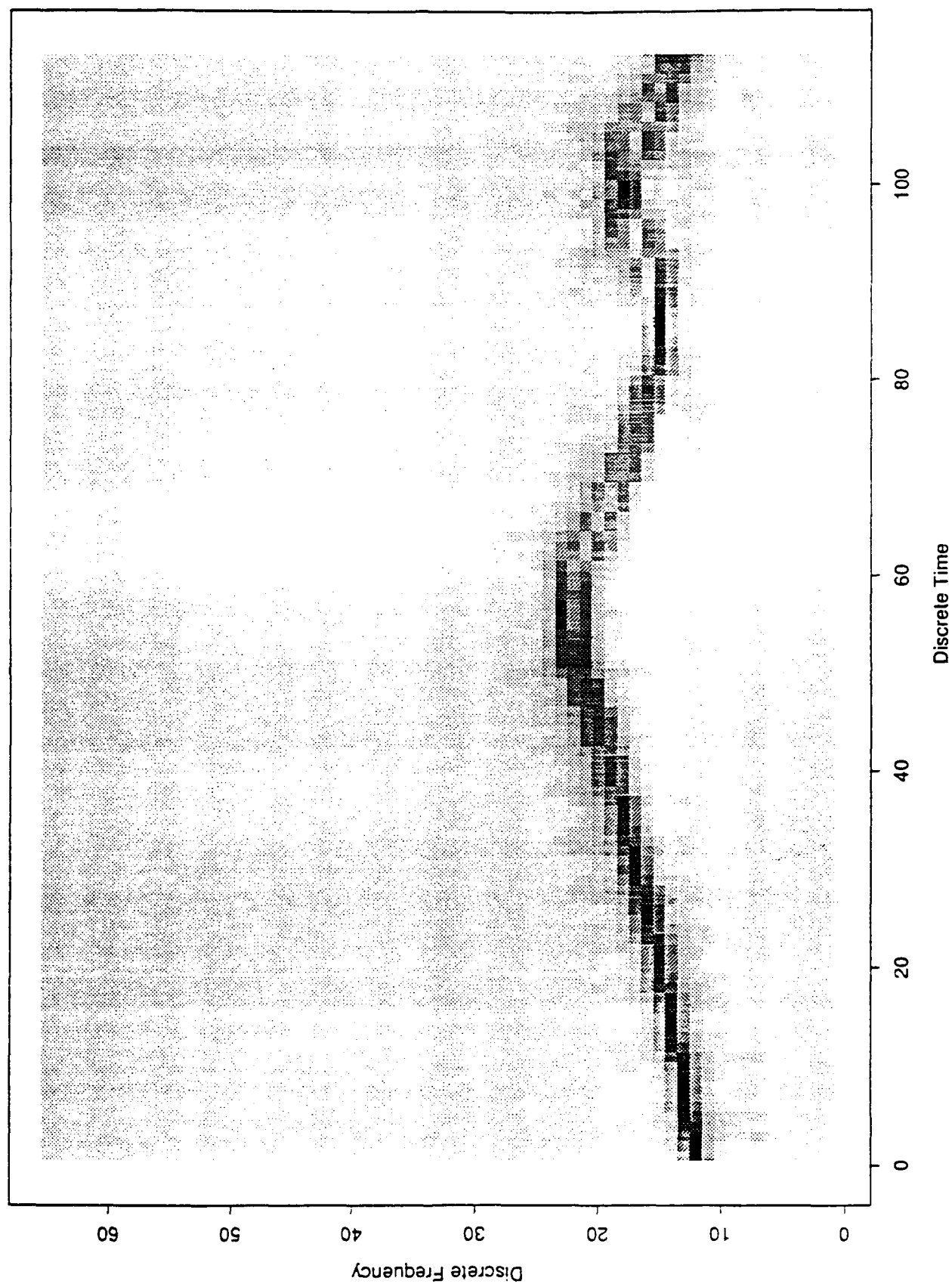


Figure VII-2

Fourier Spectrogram of Multi-Path of CHIP2

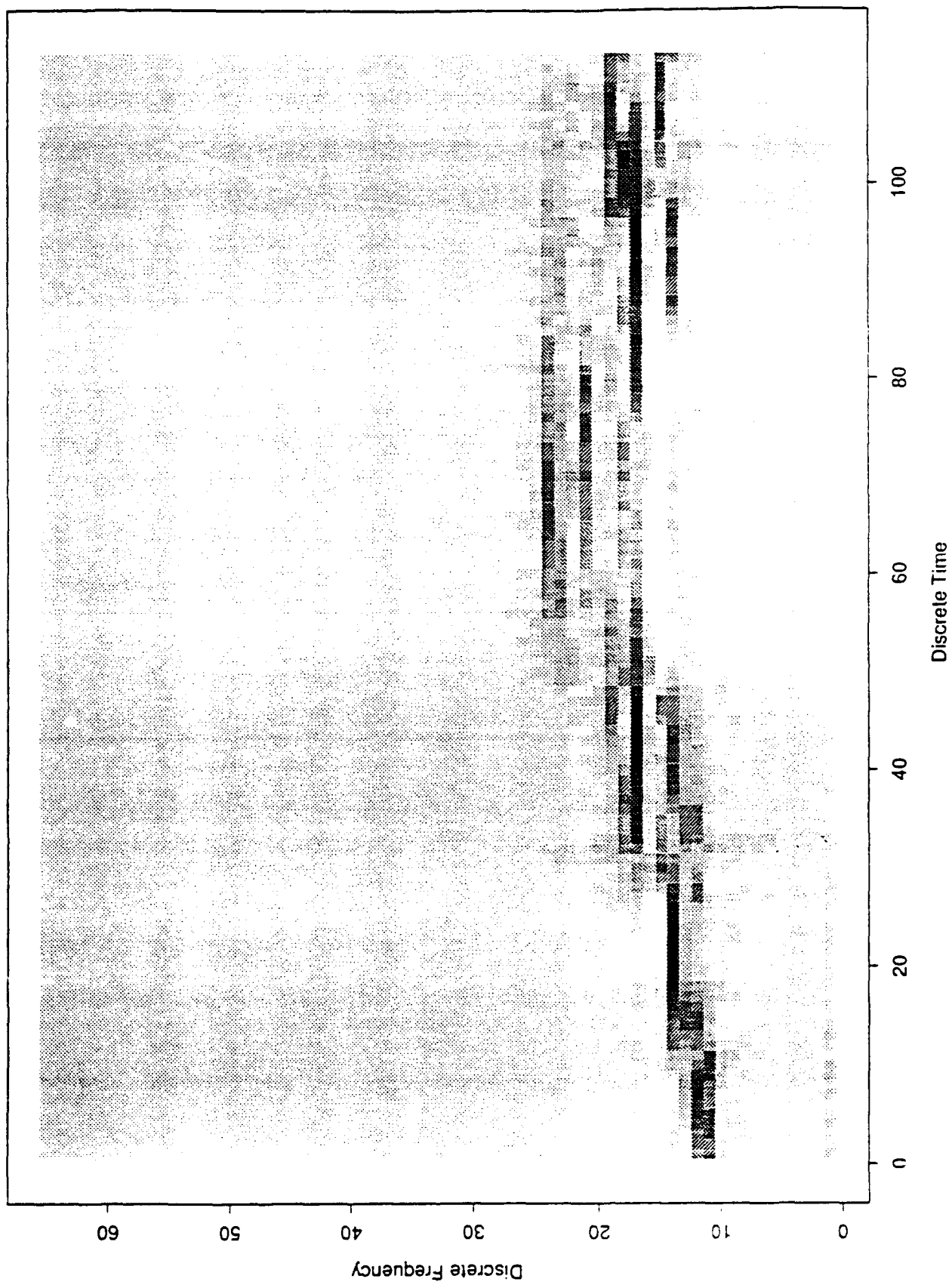


Figure VII-3

Fourier Spectrogram of +5 kts Doppler Shift and Multi-Path of CHIP2

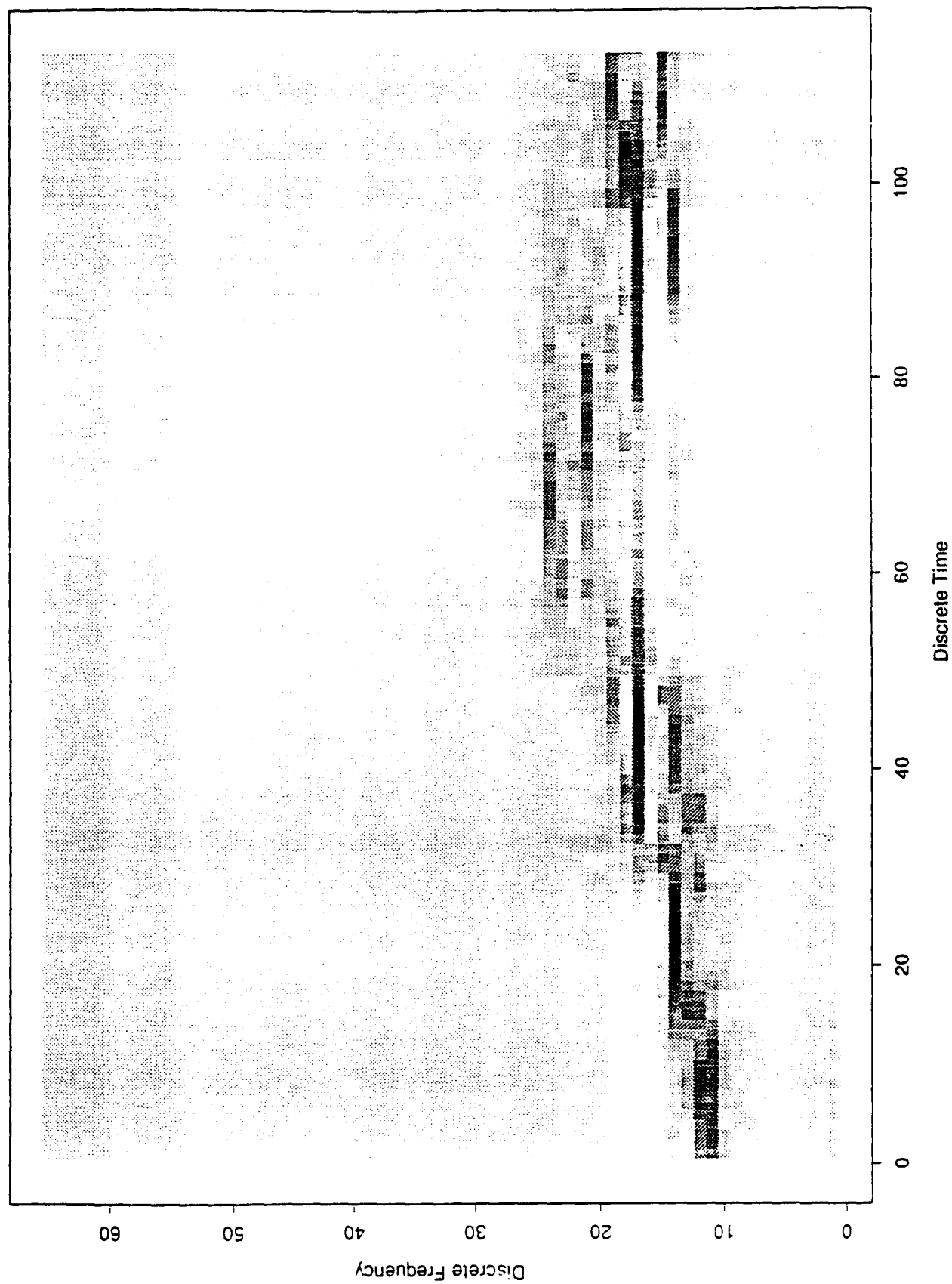


Figure VII-4

Compressed Detector +10 to -10 Doppler 10 Weights with Peak Picking
 $10 \cdot \log_{10}(\text{abs}(\text{SPL}))$ Range: 200dB to 220dB 9.18 seconds at 1000 samples / second
 Actual: 0 Doppler Single Path

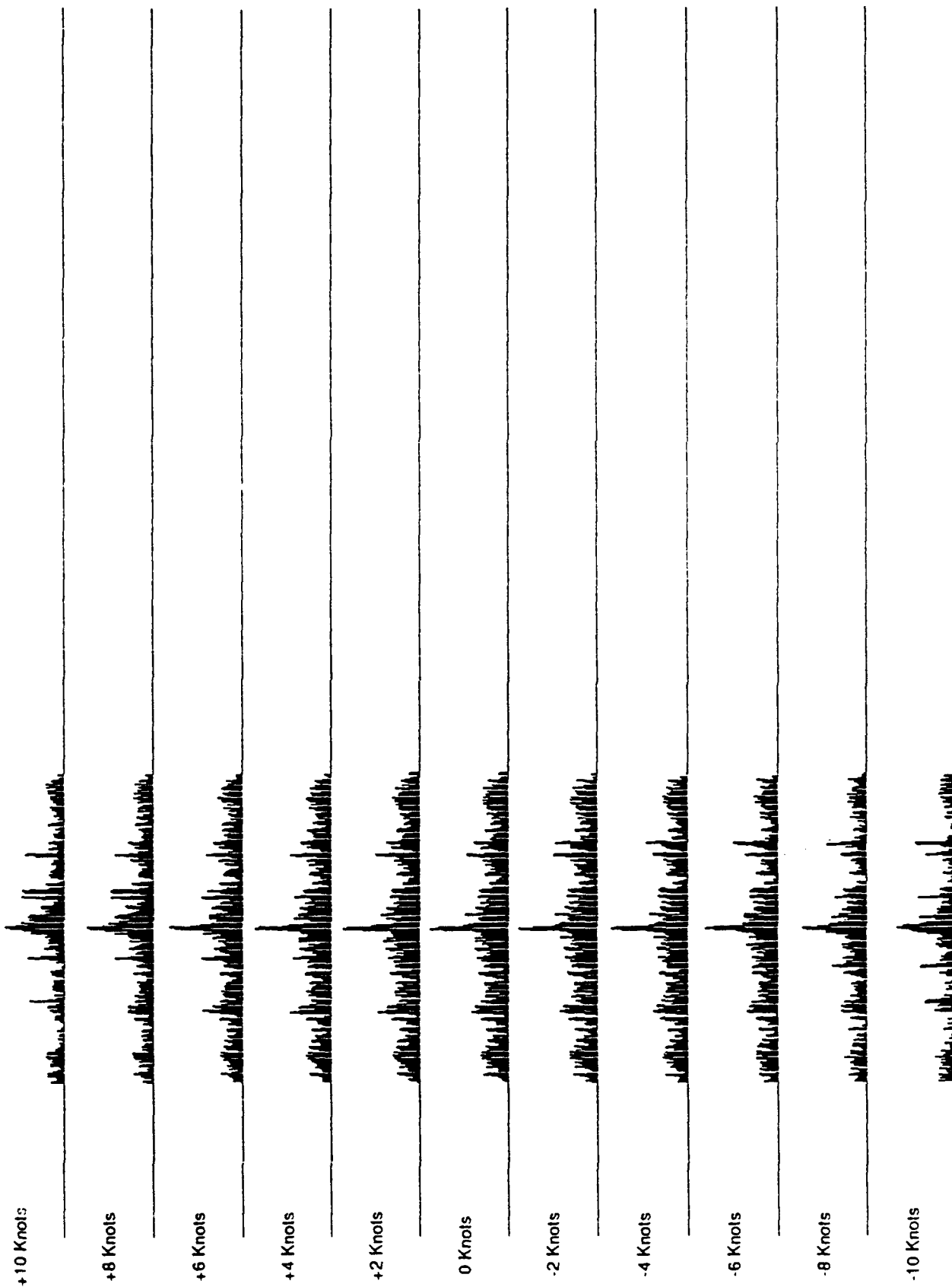


Figure VII-5

Compressed Detector +10 to -10 Doppler 10 Weights with Peak Picking
 $10 \cdot \log_{10}(\text{abs}(\text{SPL}))$ Range: 200dB to 220dB 9.18 seconds at 1000 samples / second
 Actual: Chip2/Multi-Path 0 Doppler Single Path

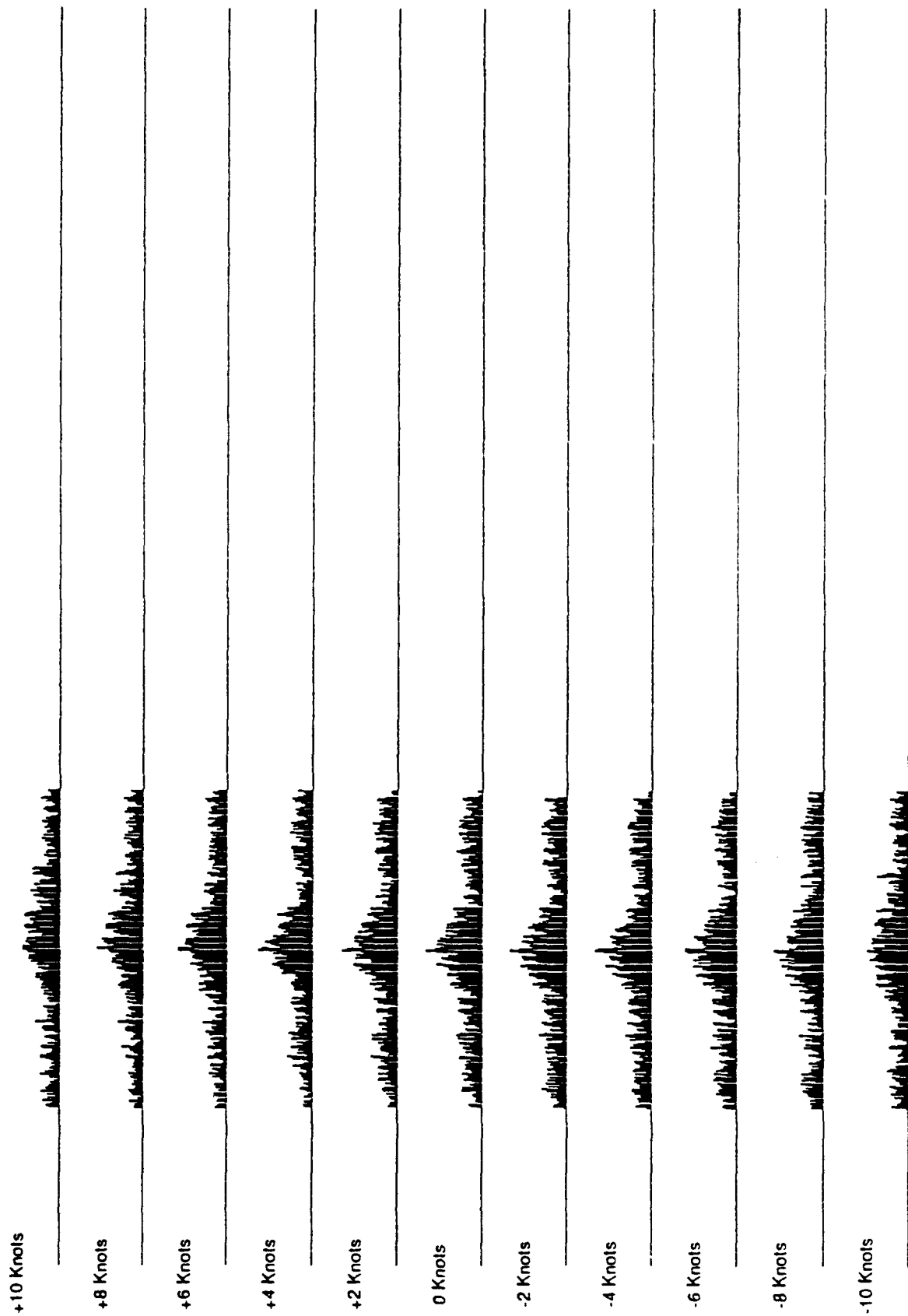


Figure VII-6

Compressed Detector +10 to -10 Doppler 10 Weights with Peak Picking
10*log10(abs(SPL)) Range: 200dB to 220dB 9.18 seconds at 1000 samples / second
Actual: Chip2/Multi-Path 0 Doppler Multi Path

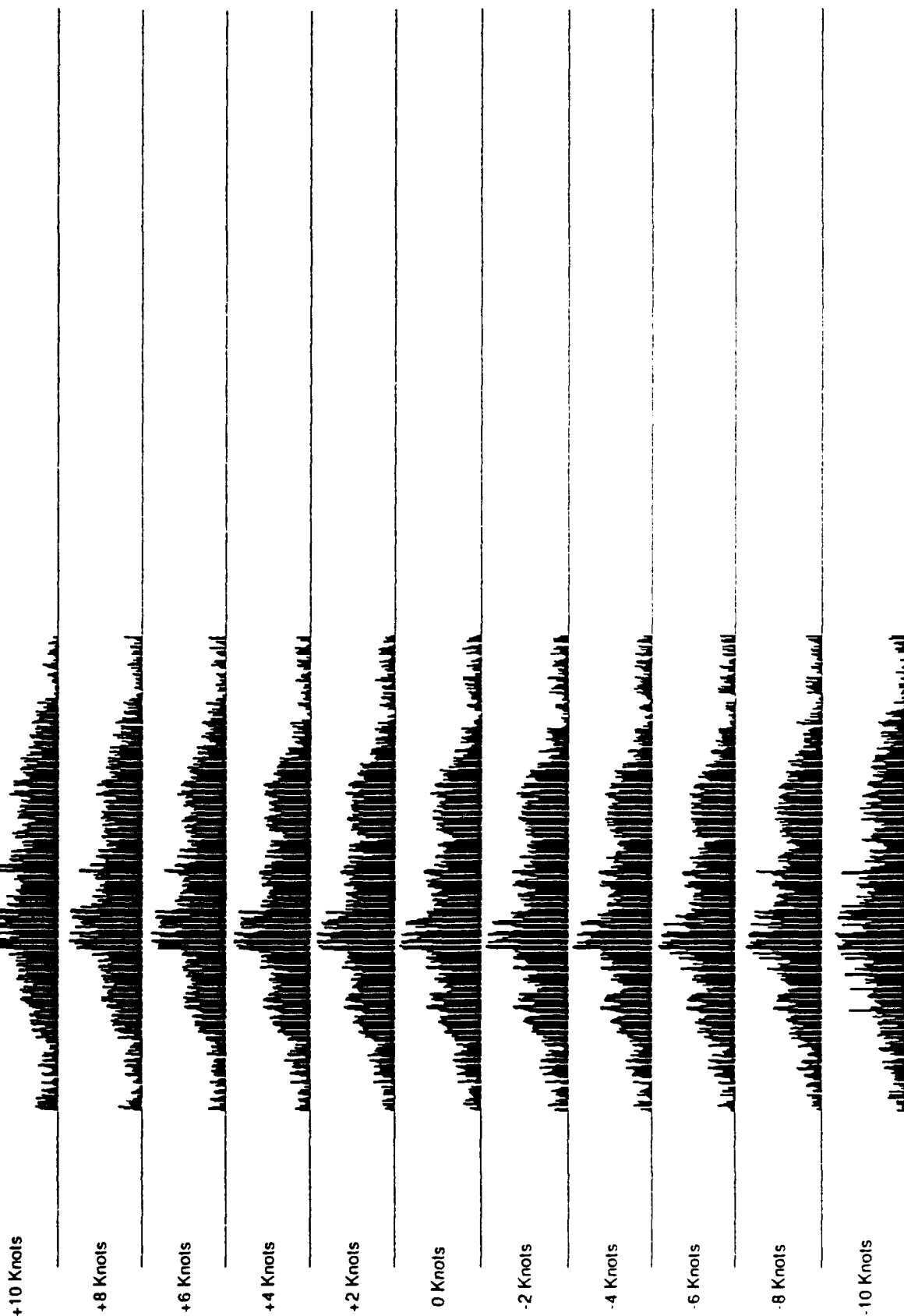


Figure VII-7

Compressed Detector +10 to -10 Doppler 10 Weights with Peak Picking
10*log10(abs(SPL)) Range: 200dB to 220dB 9.18 seconds at 1000 samples / second
Actual: Chip2/Doppler 0 Doppler Single Path

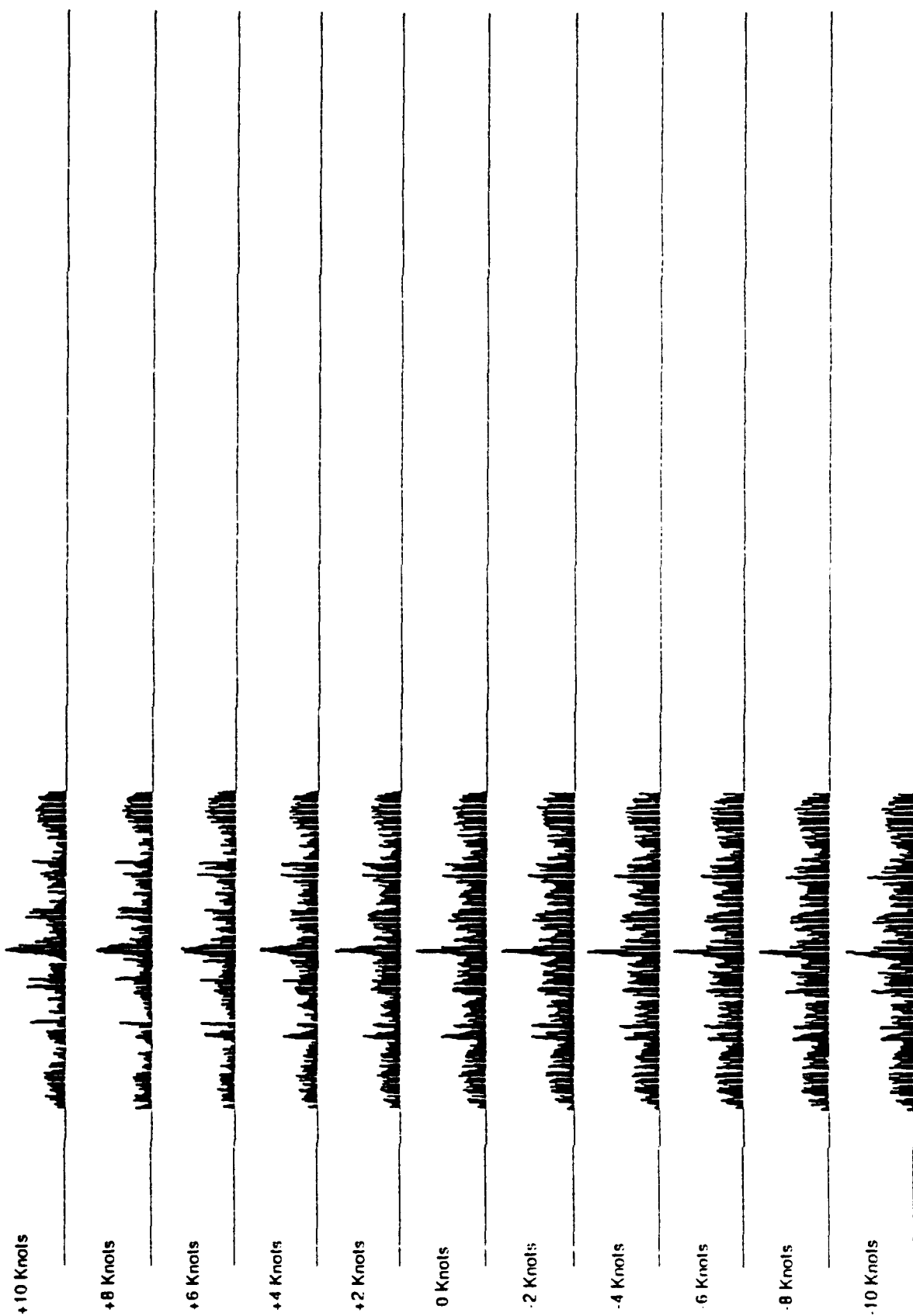


Figure VII-8

Compressed Detector +10 to -10 Doppler 10 Weights with Peak Picking
 $10 \cdot \log_{10}(\text{abs(SPL)})$ Range: 200dB to 220dB 9.18 seconds at 1000 samples / second
 Actual: 0 Doppler Multi Path

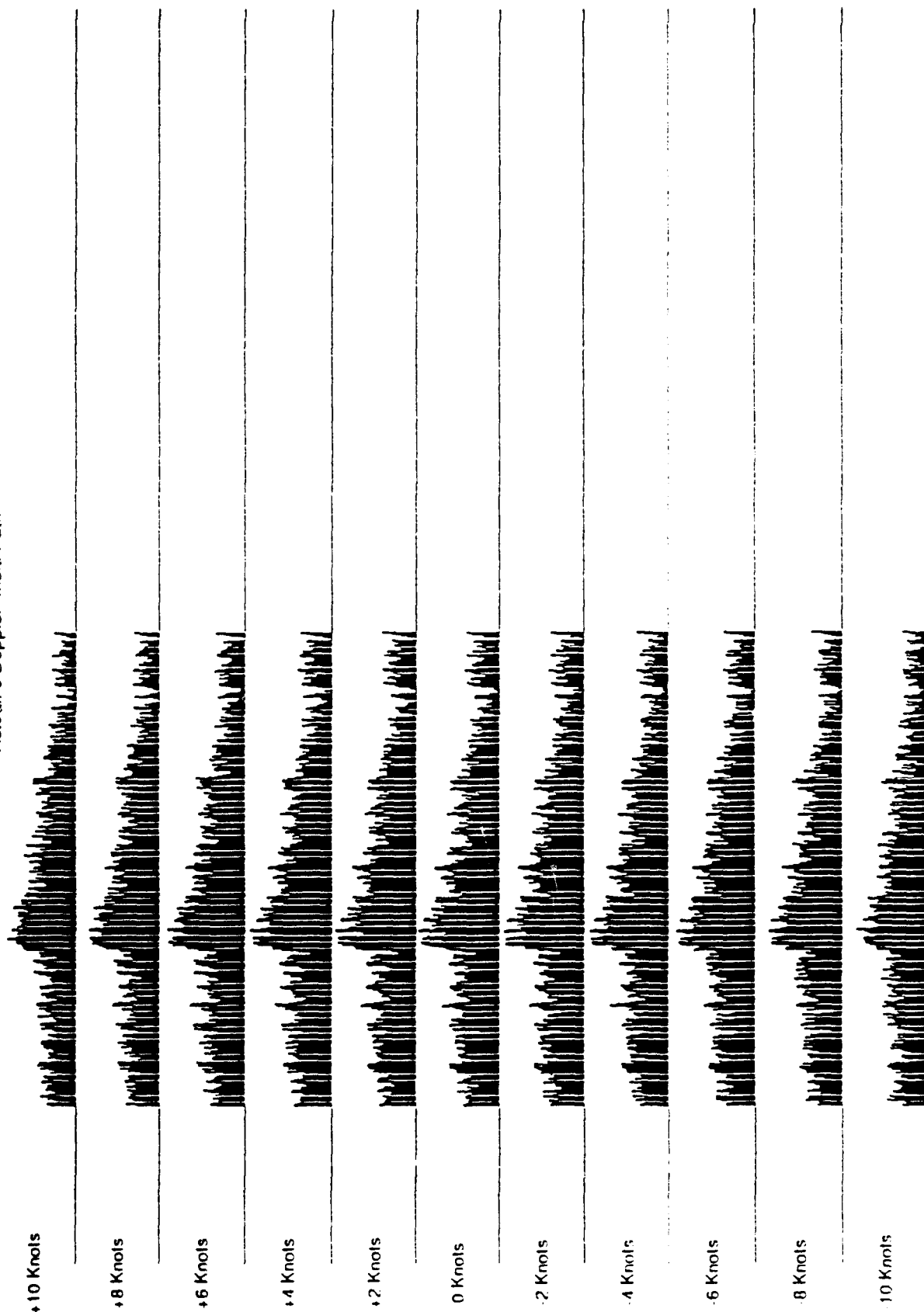


Figure VII-9

Compressed Detector +10 to -10 Doppler 10 Weights with Peak Picking
 $10 \cdot \log_{10}(\text{abs}(\text{SPL}))$ Range: 200dB to 220dB 9.18 seconds at 1000 samples / second
 Actual: Chip2/Doppler 0 Doppler Multi-Path

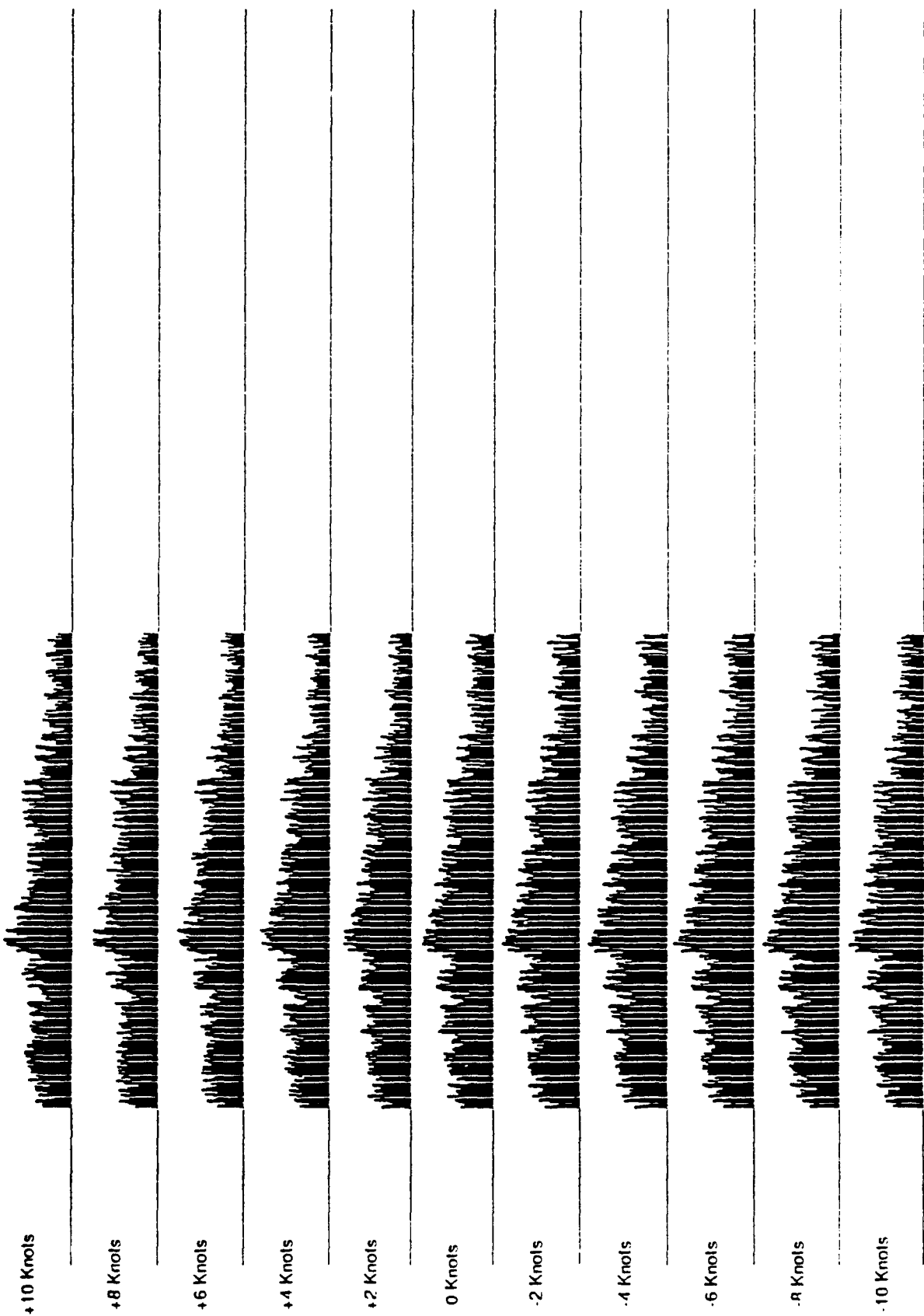


Figure VII-10

Compressed Detector +10 to -10 Doppler 10 Weights with Peak Picking
 $10 \cdot \log_{10}(\text{abs}(\text{SPL}))$ Range: 180dB to 200dB 9.18 seconds at 1000 samples / second
Actual: Chip2/Multi-Path +5 Doppler Multi-Path

+10 Knots

+8 Knots

+6 Knots

+4 Knots

+2 Knots

0 Knots

-2 Knots

-4 Knots

-6 Knots

-8 Knots

-10 Knots

Figure VII-11

Compressed Detector +10 to -10 Doppler 10 Weights with Peak Picking
10*log10(abs(SPL)) Range: 180dB to 200dB 9.18 seconds at 1000 samples / second
Actual: Chip2/Multi-Path +5 Doppler Single Path

+10 Knots

+8 Knots

+6 Knots

+4 Knots

+2 Knots

0 Knots

-2 Knots

-4 Knots

-6 Knots

-8 Knots

-10 Knots

Figure VII-12

Compressed Detector +10 to -10 Doppler 10 Weights with Peak Picking
 $10 \cdot \log_{10}(\text{abs}(\text{SPL}))$ Range: 210dB to 230dB 9.18 seconds at 1000 samples / second
 Actual: Pulse100_short 0 Doppler Multi Path

+10 Knots



+8 Knots



+6 Knots



+4 Knots



+2 Knots



0 Knots



-2 Knots



-4 Knots



-6 Knots



-8 Knots



-10 Knots



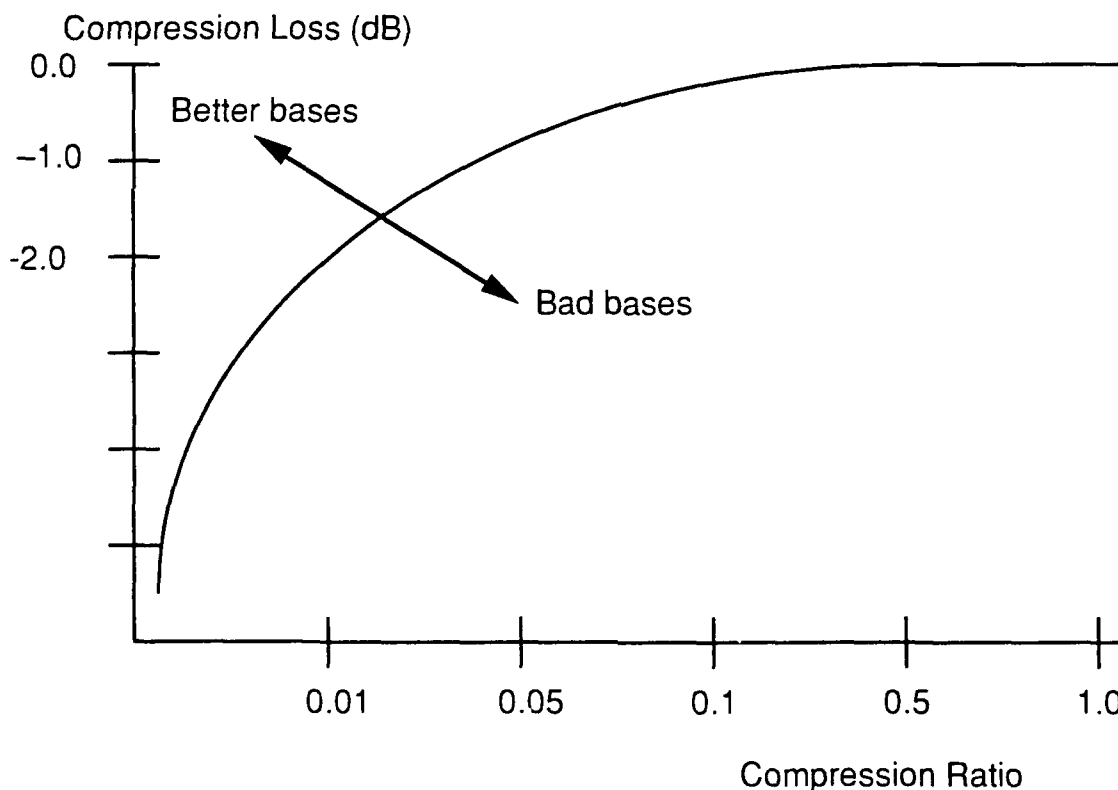
Figure VII-13

2. Compression Loss-versus-Compression Ratio Tests

The results of these compression loss-versus-compression ratio tests are much more encouraging and substantial than the multi-channel detector experiment. In these series of tests, we have definitely determined that the l^2 -closest wavelet basis outperforms all other standard bases for compressed Neyman-Pearson detection.

Recall from the previous chapter that the goal of choosing an appropriate basis is borne out by little compression loss for large compression ratios. Figure VII-14 shows a hypothetical compression loss-versus-compression ratio plot, with directions showing what makes for a "good" or "bad" detection basis.

Figure VII-14



In using the basic compressed Neyman-Pearson detector, we do not zero-pad the signal; hence, we create the l^2 -closest 3-level wavelet basis based on the signal. See Figure VI-4 for the time-series plot of the l^2 -closest 3rd-level wavelet function. Figure VI-5 shows the difference between the CHIP2 signal and the l^2 -closest 3rd-level wavelet function. Figure VI-6 shows the

time-series plots of all the wavelet functions: first, second, third, and the extra third-level wavelet functions.

Figure VII-15 shows the wavelet transform of CHIP2 (sometimes abbreviated as CH2), offset by 0, 1, 2, and 3. The wavelet basis is the l^2 -closest 3-level wavelet basis. One can see that the signal is highly concentrated in the zero offset at $n = 832$. We also sent this signal through our transmission simulation system, simulating a +5 kt Doppler, a shallow-channel bottom-bounce effect, and the combination of both: a +5 kt Doppler shift and the effect of a shallow channel. Figure VI-7 shows the time-series plots of CHIP2 in these situations, compared to the prototype. Figure VII-16 shows the wavelet transform of each of the above affected (Doppler, shallow channel) signal, with respect to the l^2 -closest 3-level wavelet basis. As expected, the prototype signal shows the best concentration of the weights in a small interval, and the shallow channel and +5 kt Doppler case has the worst concentration of weights.

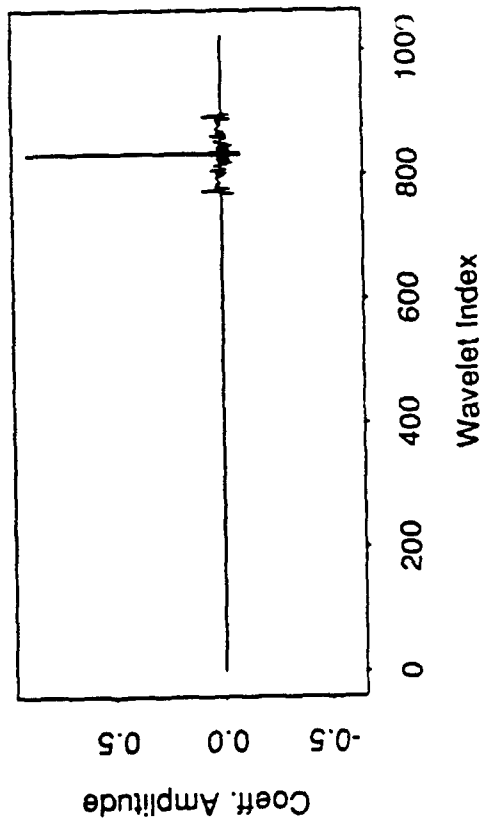
For comparison to the other bases, Figure VII-17 shows the transforms of CHIP2 in the delta basis (time basis, hence the identity transform), the absolute part of the Fourier transform, and the real Shannon wavelet transform, and the l^2 -closest wavelet basis. As expected, the l^2 -closest wavelet basis shows the best concentration of the weights in a small interval.

Figures VII-18 through VII-33 show the compression loss curves for various bases for the purpose of comparison. Figure VII-18 compares five bases in the case when there is no Doppler-shifting and the signal is not offset in the window; note that the l^2 -closest wavelet basis is the clear winner. Figures VII-19 through VII-23 show the result of offsetting the signal in the window on the various individual compressed detectors. Figure VII-24 compares the l^2 -closest wavelet basis, the D4 wavelet basis, and the real Shannon wavelet basis when the signal is offset by 2. Figure VII-25 compares the l^2 -closest wavelet basis, the real Shannon wavelet basis, and the Fourier basis when all offsets from 0-4 have been combined to form worst-case curves. (The recursive nature of the wavelet basis implies only the 0 through 4 translates be studied; any greater translates will yield redundant results.) In both Figures VII-25 and VII-25, the l^2 -closest wavelet basis performs the best. Figures VII-26 through VII-31 show the result of Doppler-shifting on six different bases. Figure VII-32 compares the l^2 -closest wavelet basis, the D4 wavelet basis, the delta basis, the Fourier basis, and the real Shannon basis when there is Doppler-shifting corresponding to -4 knots. Figure VII-33 compares the l^2 -closest wavelet basis, the delta basis, the Fourier basis, and the real Shannon basis when Doppler shifts from -4 knots to +4 knots (in 2-knot increments) have been combined to form worst-case curves. In these last two figures, the l^2 -closest wavelet basis is once again the winner.

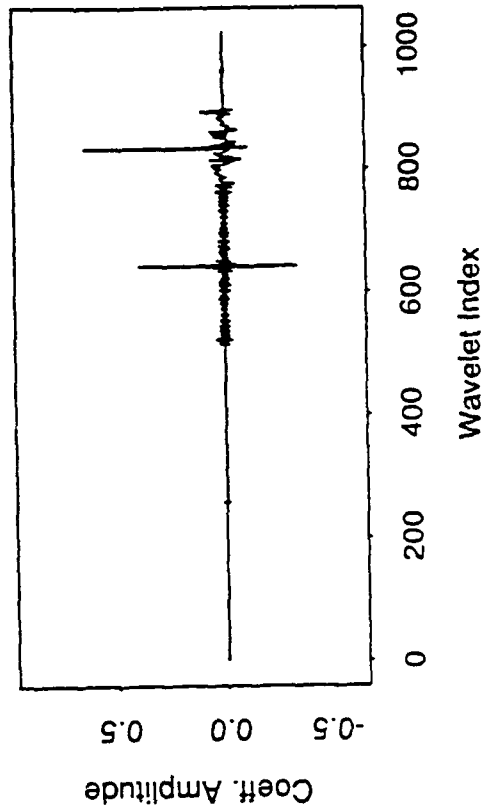
Finally, the most important test of computation speed is the amount of real time it takes to perform the computations to achieve a certain level of degradation. We conducted timing comparison studies and, again, showed the l^2 -closest wavelet basis achieves a low amount of degradation in a shorter computing time than other bases. Figure VII-34 shows the compression loss as a function of relative time.

Comparison of CHIPS 2 Representations Closest Wavelet Basis

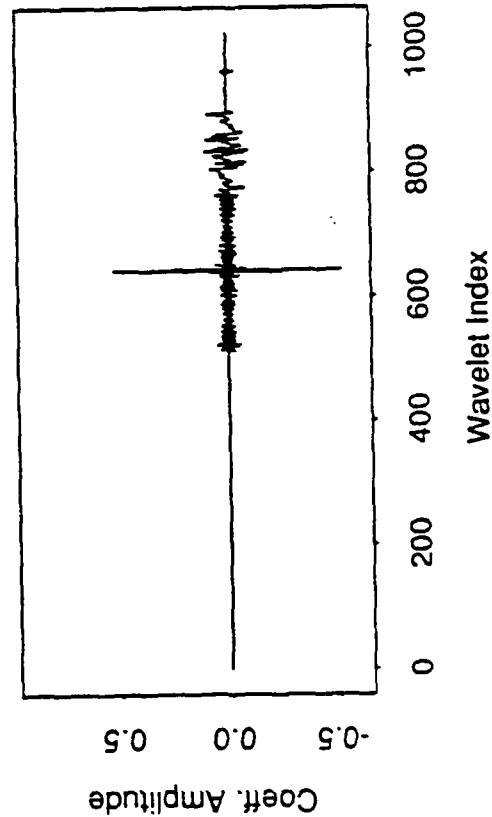
No Rotation



Rotated by 1



Rotated by 2



Rotated by 3

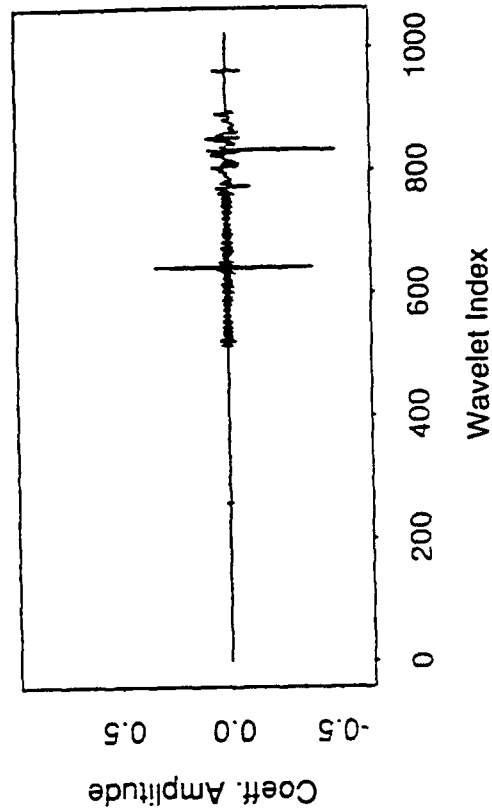
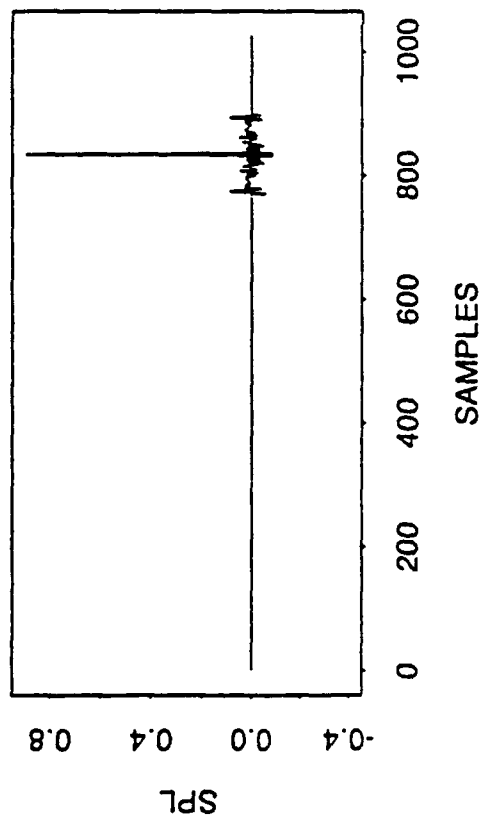


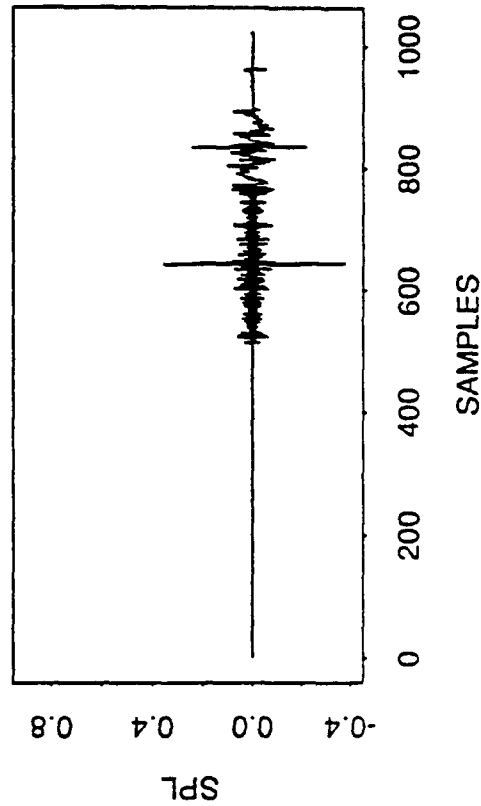
Figure VII-15

Transformation of CHIPS 2 Closest Level 3 Wavelet Representation

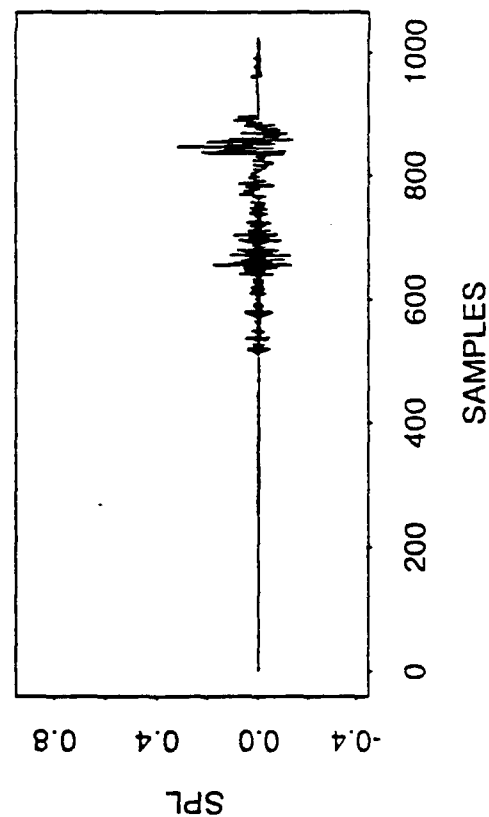
Original CHIPS 2



+5 Knot Doppler



Shallow Channel



Shallow Channel and +5 Knot Doppler

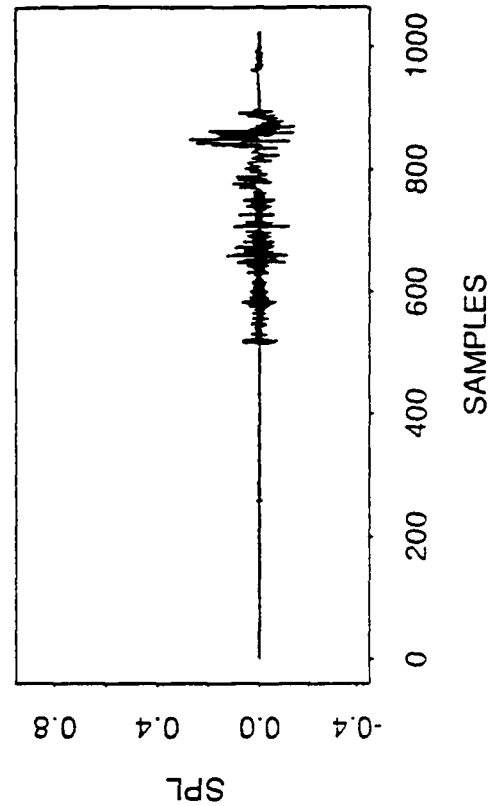
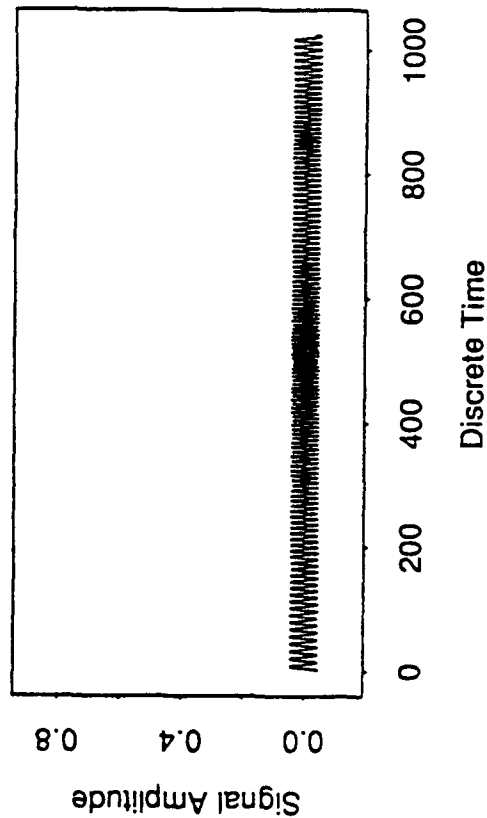


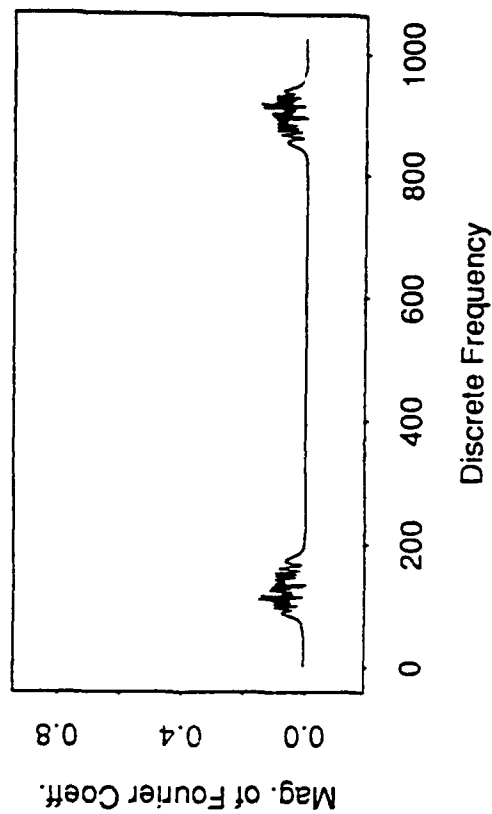
Figure VII-16

Comparison of CHIPS 2 Representations

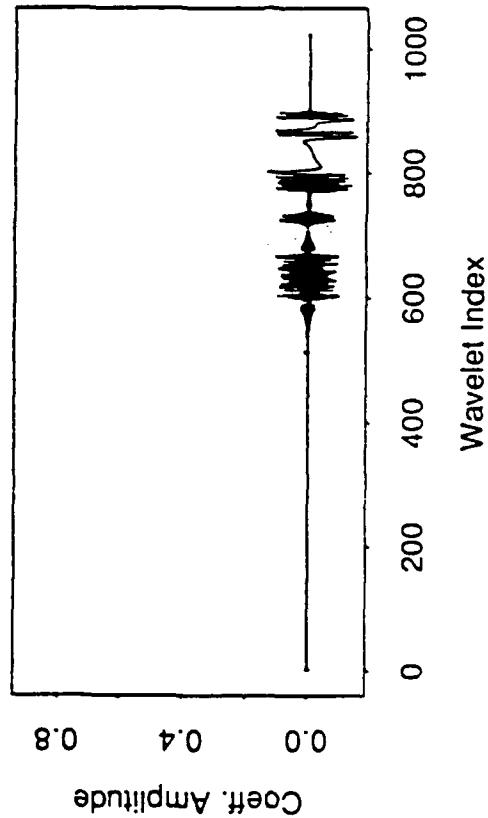
Time Series



Abs. part of Fourier transform



Shannon wavelet basis



Closest wavelet basis

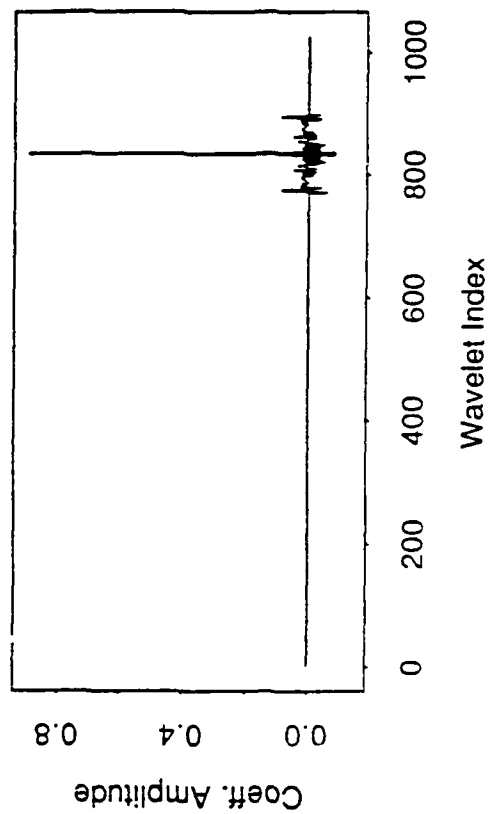


Figure VII-17

COMPRESSION LOSS CHIP2

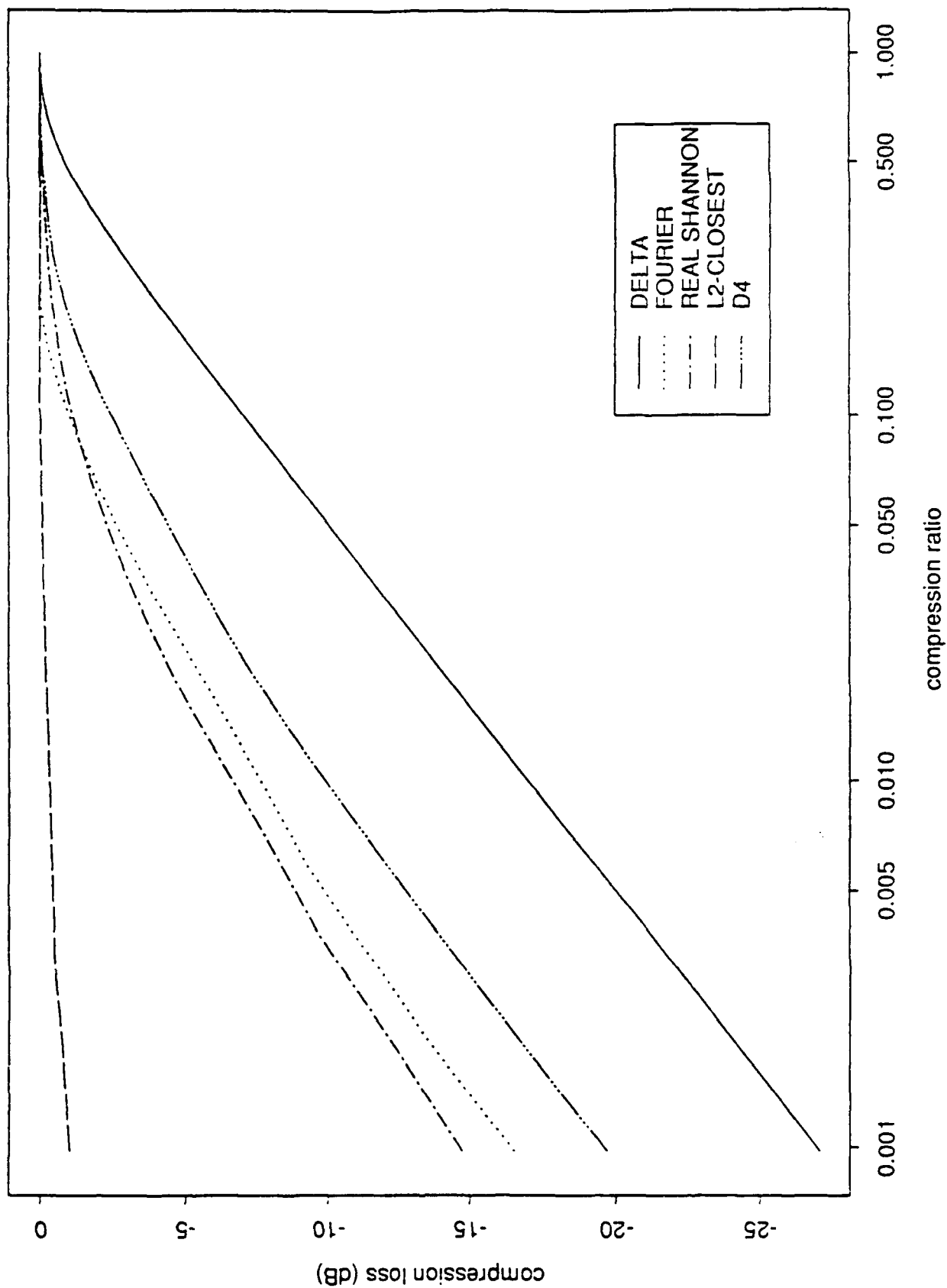


Figure VII-18

COMPRESSION LOSS, CHIP2, L2-CLOSEST

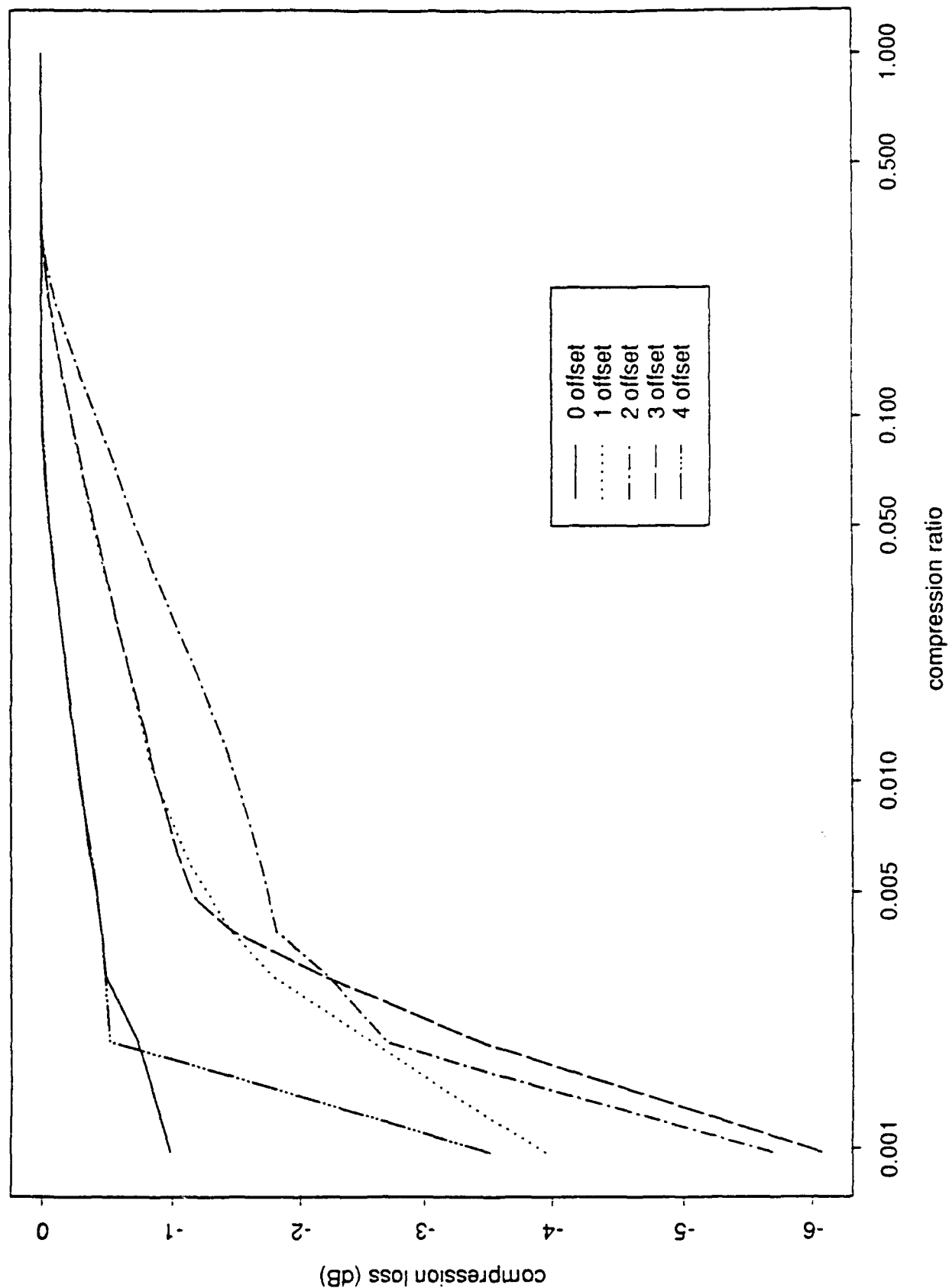


Figure VII-19

COMPRESSION LOSS, CHIP2, D4

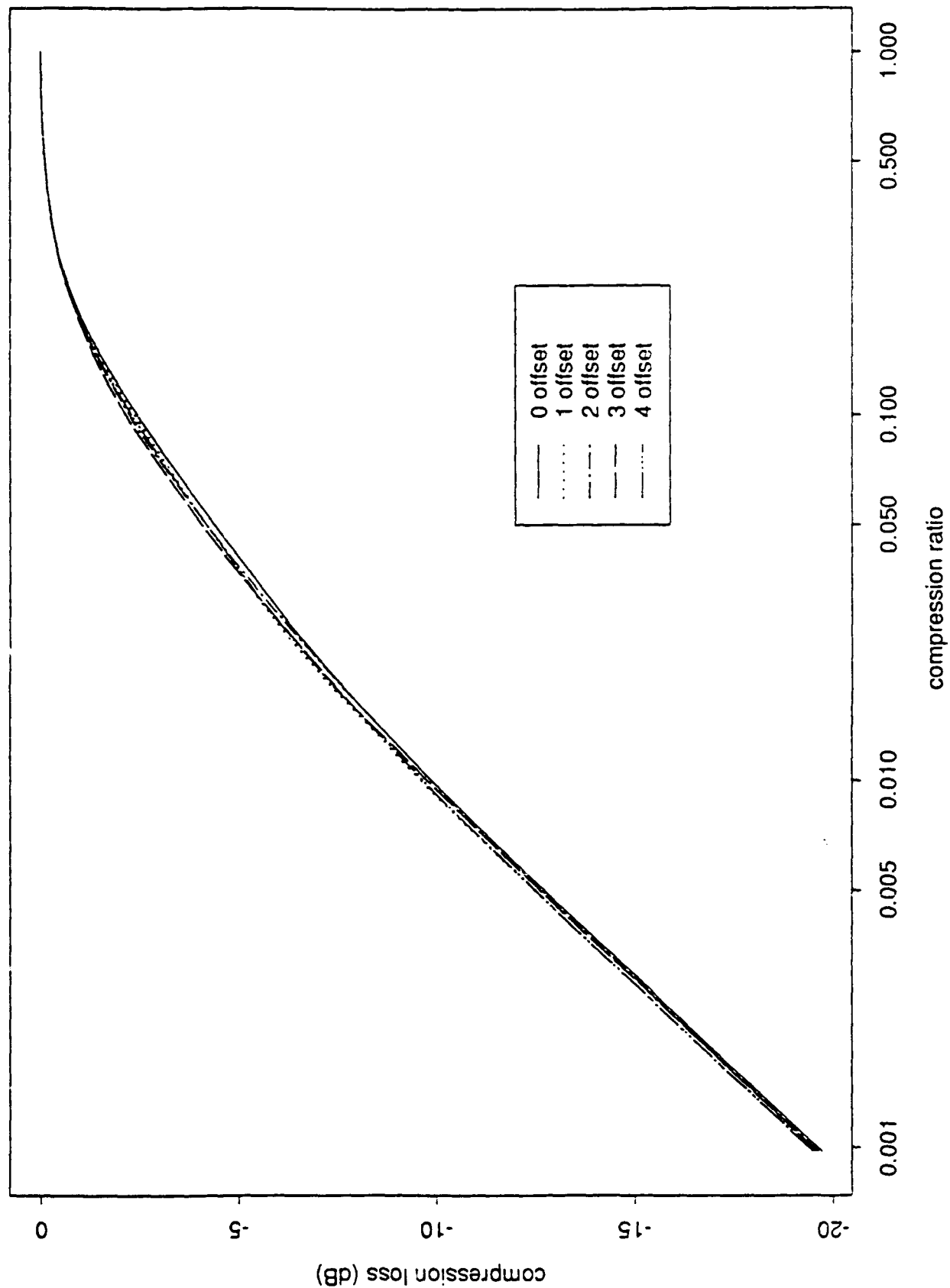


Figure VII-20

COMPRESSION LOSS, CHIP2, REAL SHANNON

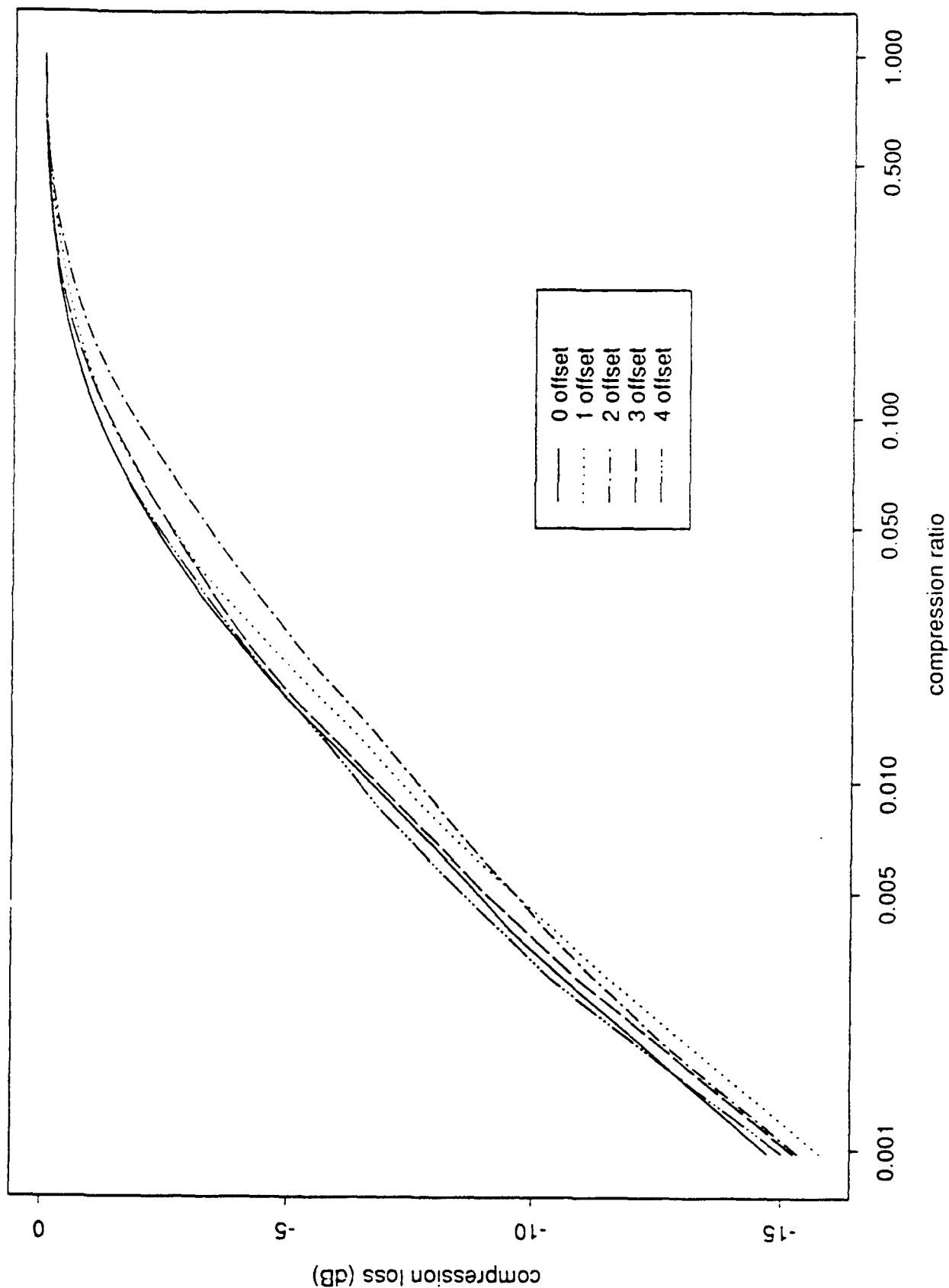


Figure VII-21

COMPRESSION LOSS CHIP2, OFFSETS CHIP2 - BINARY DECOMPOSITION

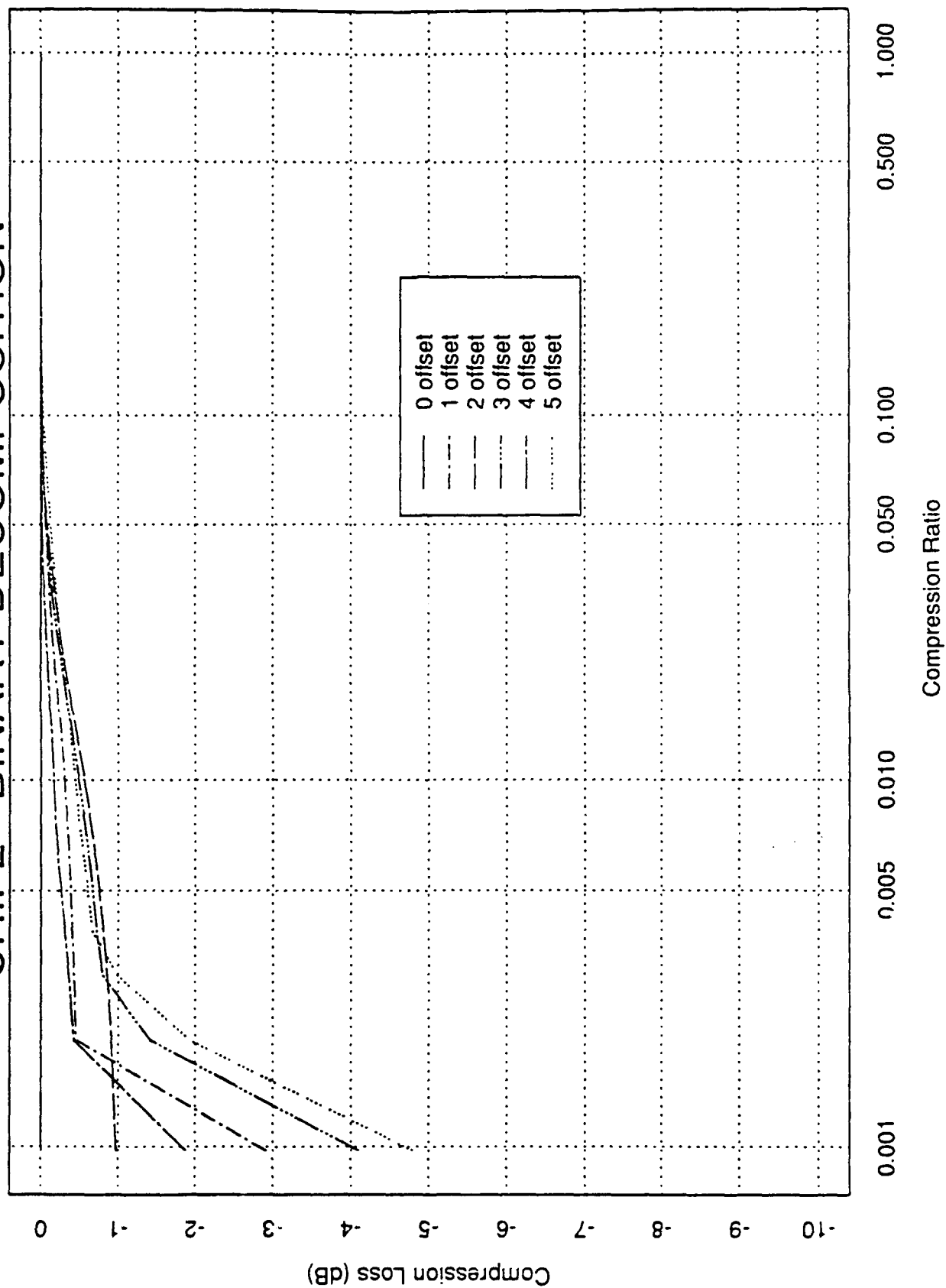


Figure VII-22

COMPRESSION LOSS CHIP2, OFFSETS CHIP2 - BINARY DECOMPOSITION

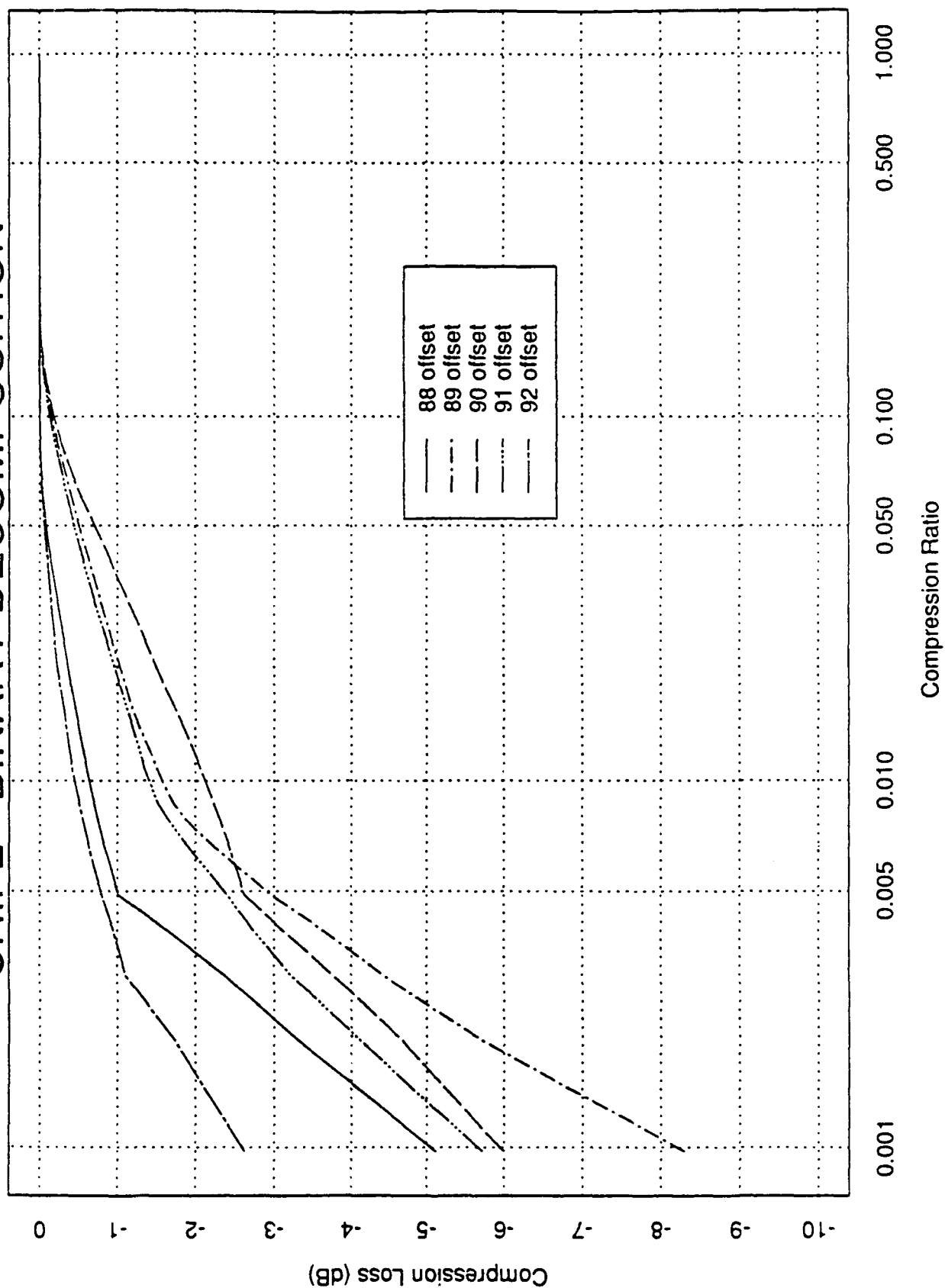


Figure VII-23

COMPRESSION LOSS, CHIP2, 2 OFFSET

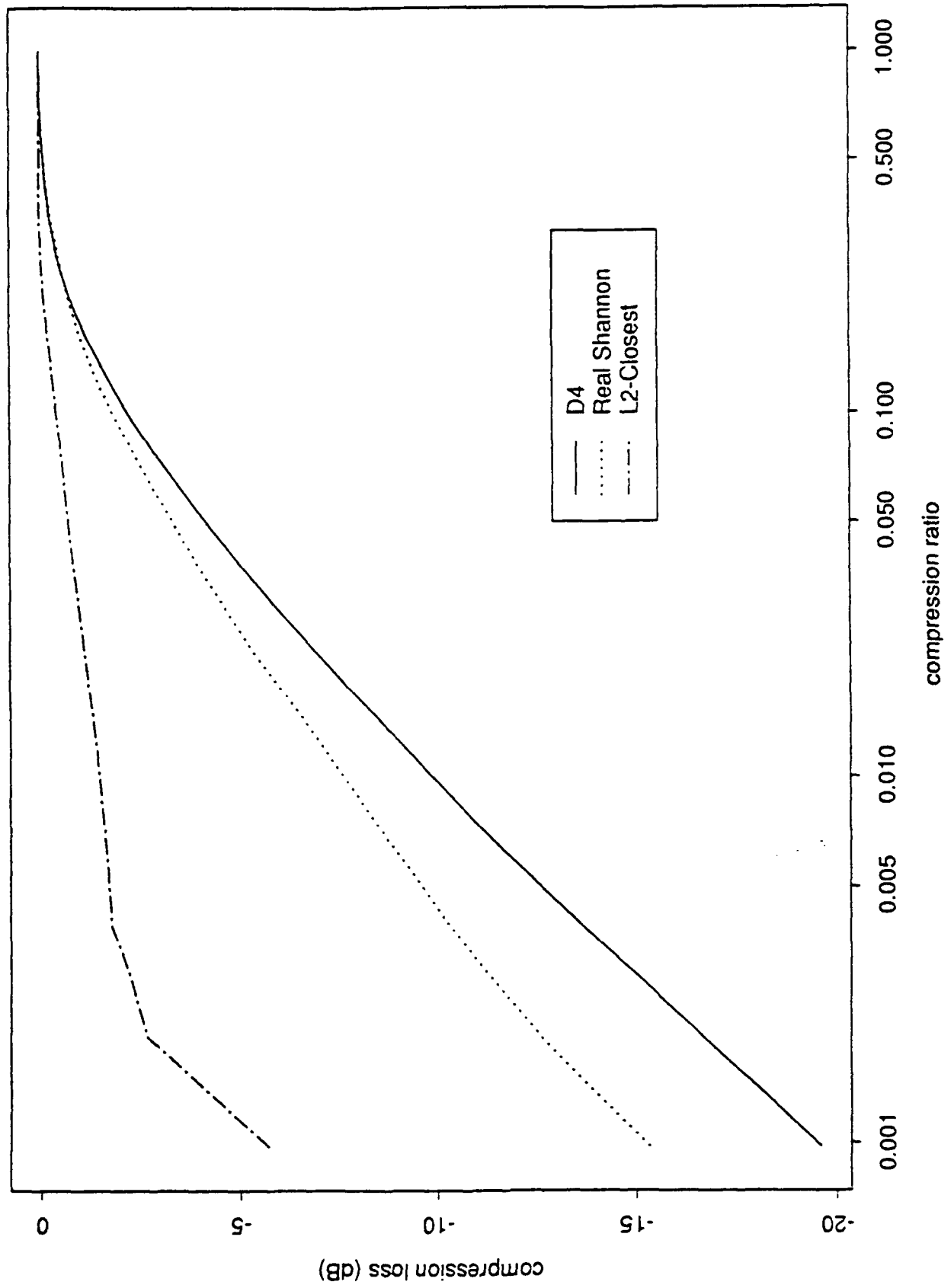


Figure VII-24

COMPRESSION LOSS, CHIP2, OFFSETS COMBINED

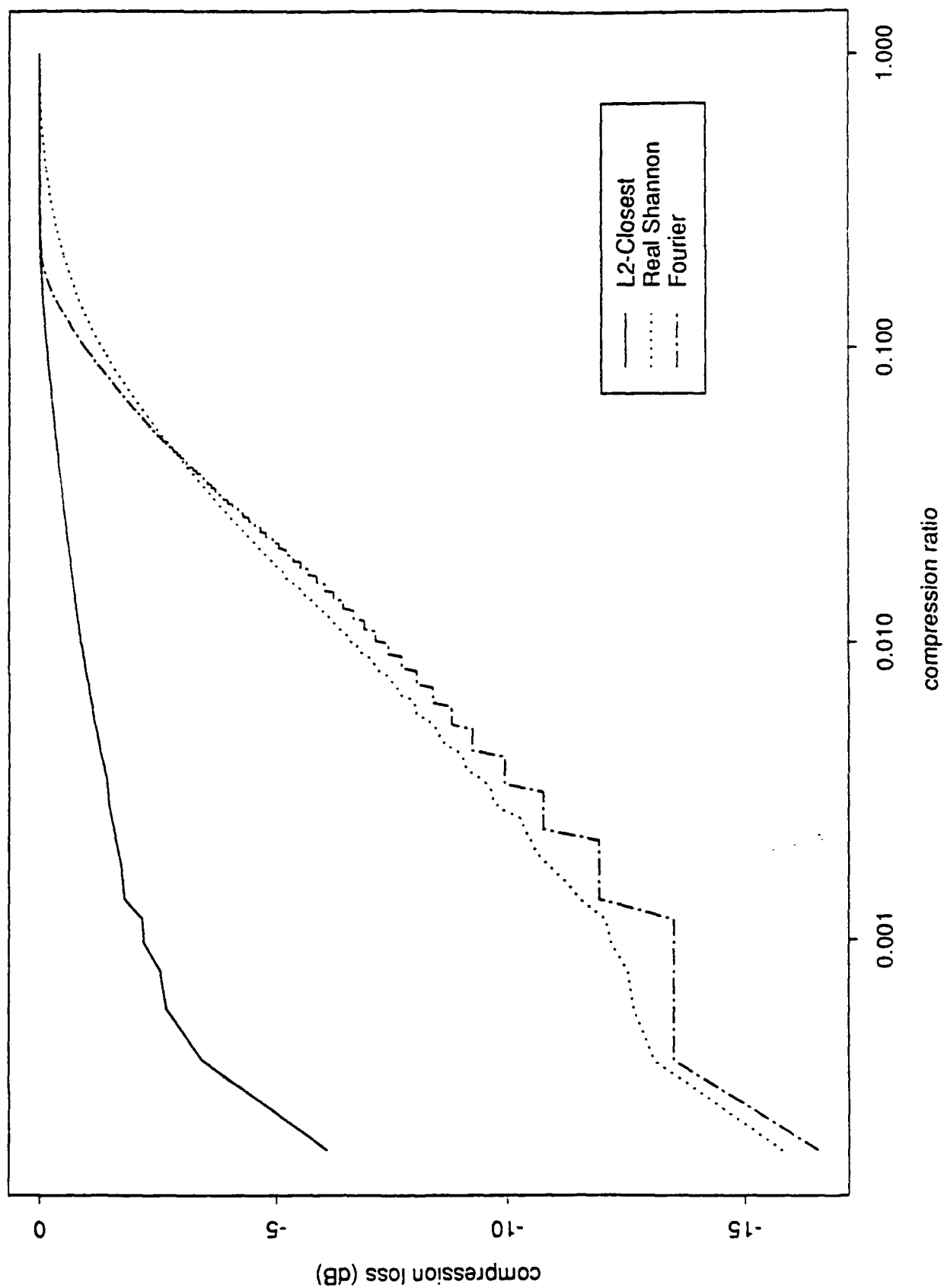


Figure VII-25

COMPRESSION LOSS, CHIP2 WITH DOPPLER, L2-CLOSEST

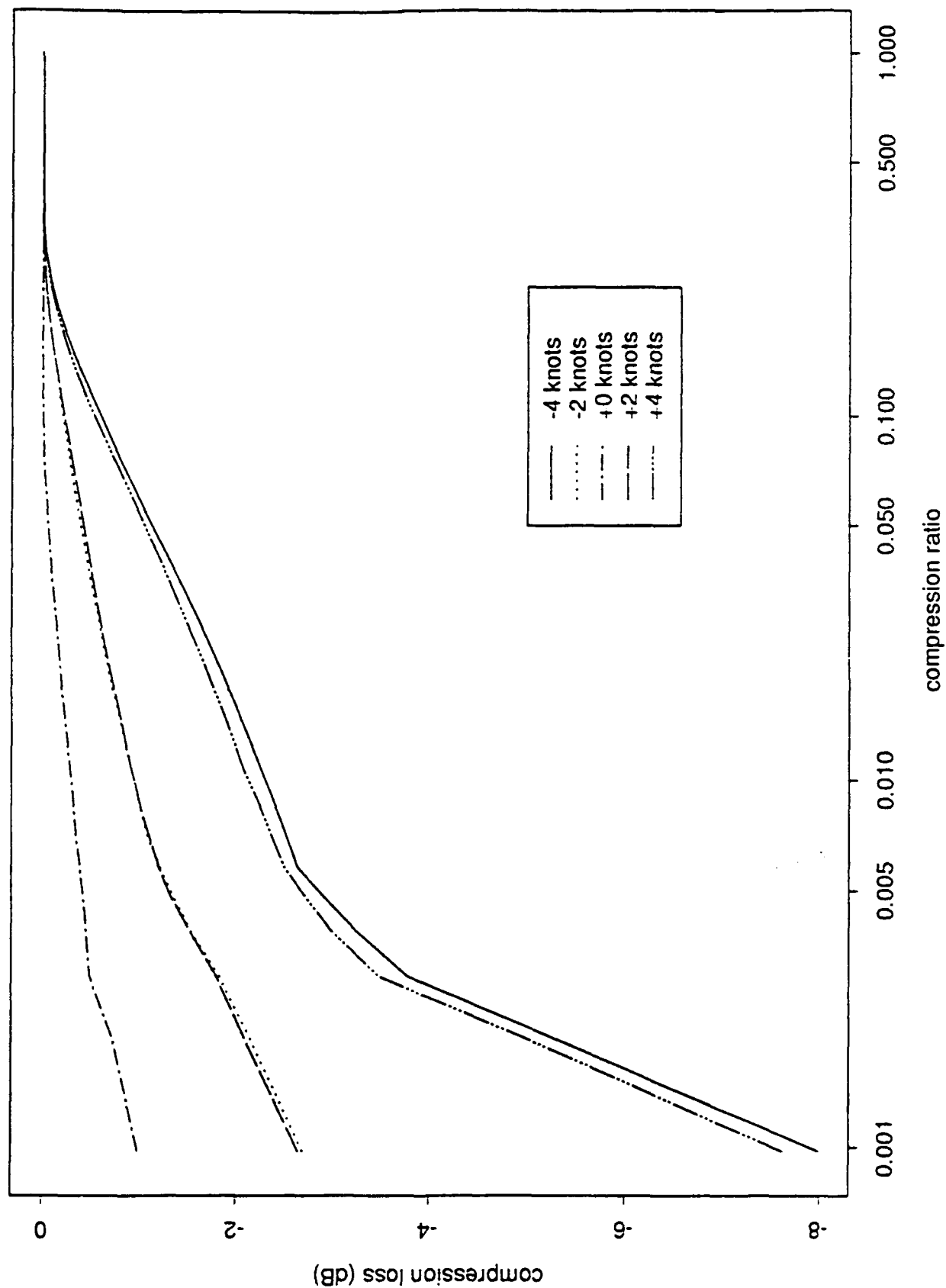


Figure VII-26

COMPRESSION LOSS, CHIP2 WITH DOPPLER, D4

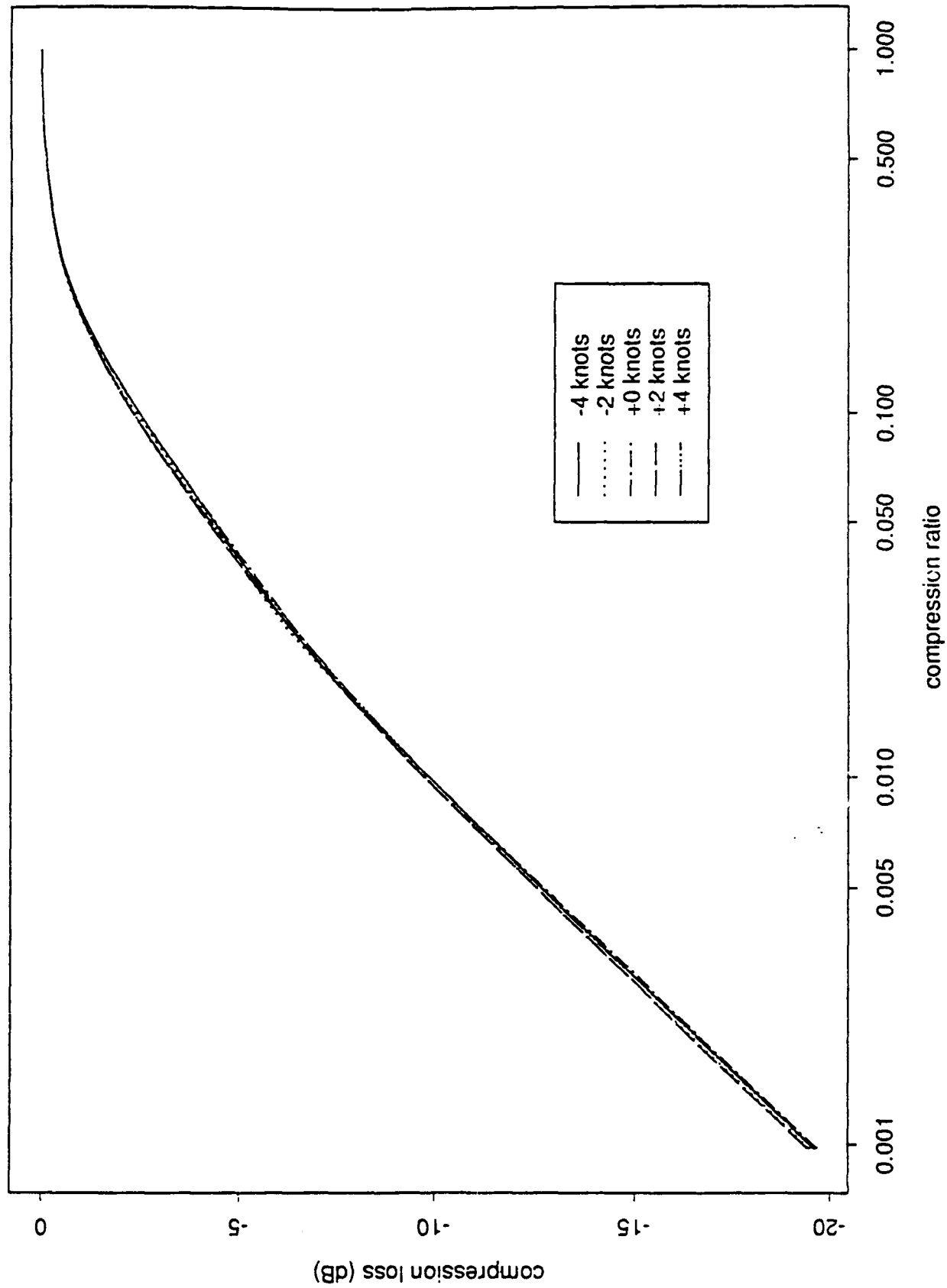


Figure VII-27

COMPRESSION LOSS, CHIP2 WITH DOPPLER, DELTA

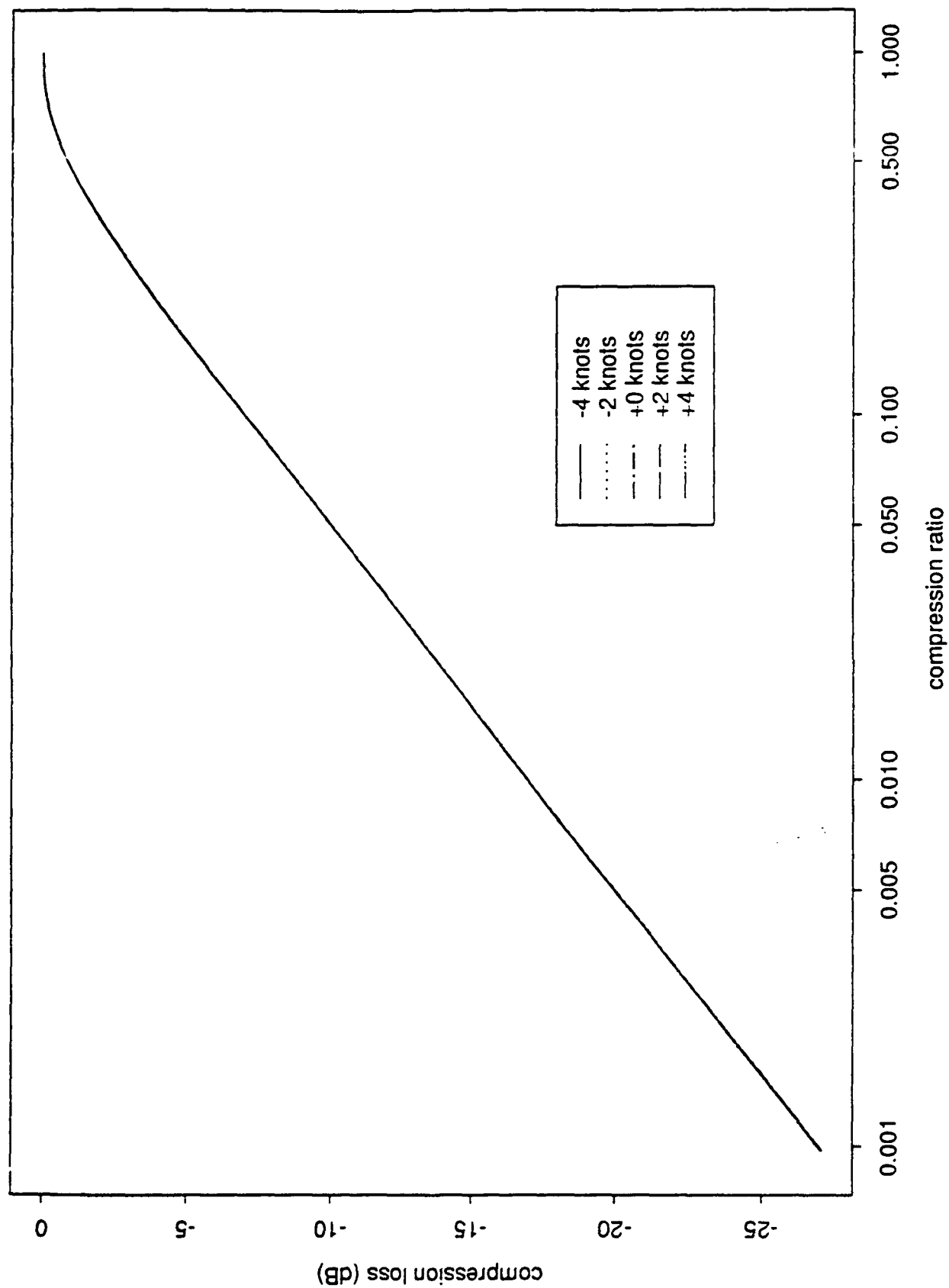


Figure VII-28

COMPRESSION LOSS, CHIP2 WITH DOPPLER, FOURIER

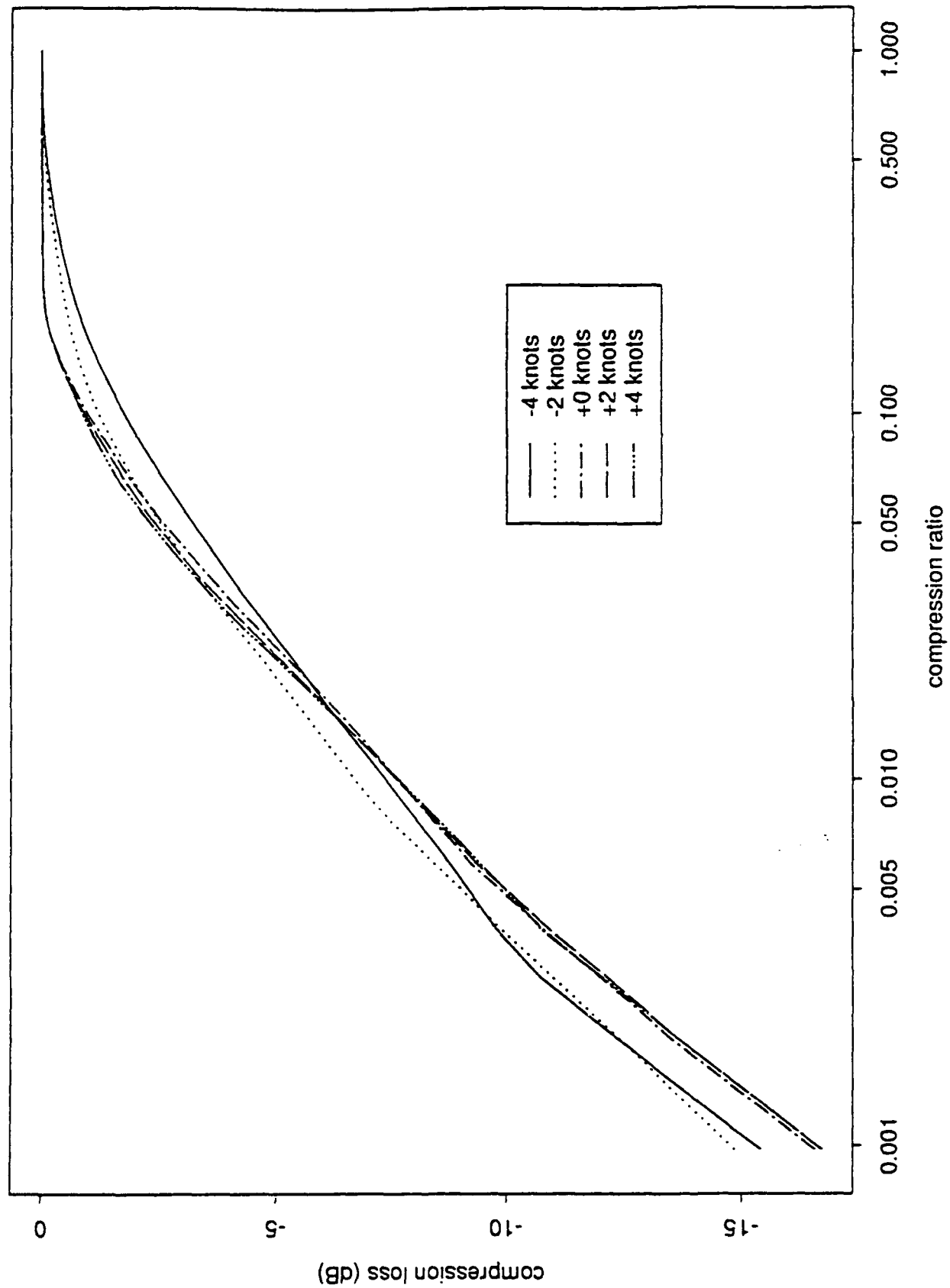


Figure VII-29

COMPRESSION LOSS, CHIP2 WITH DOPPLER, REAL SHANNON

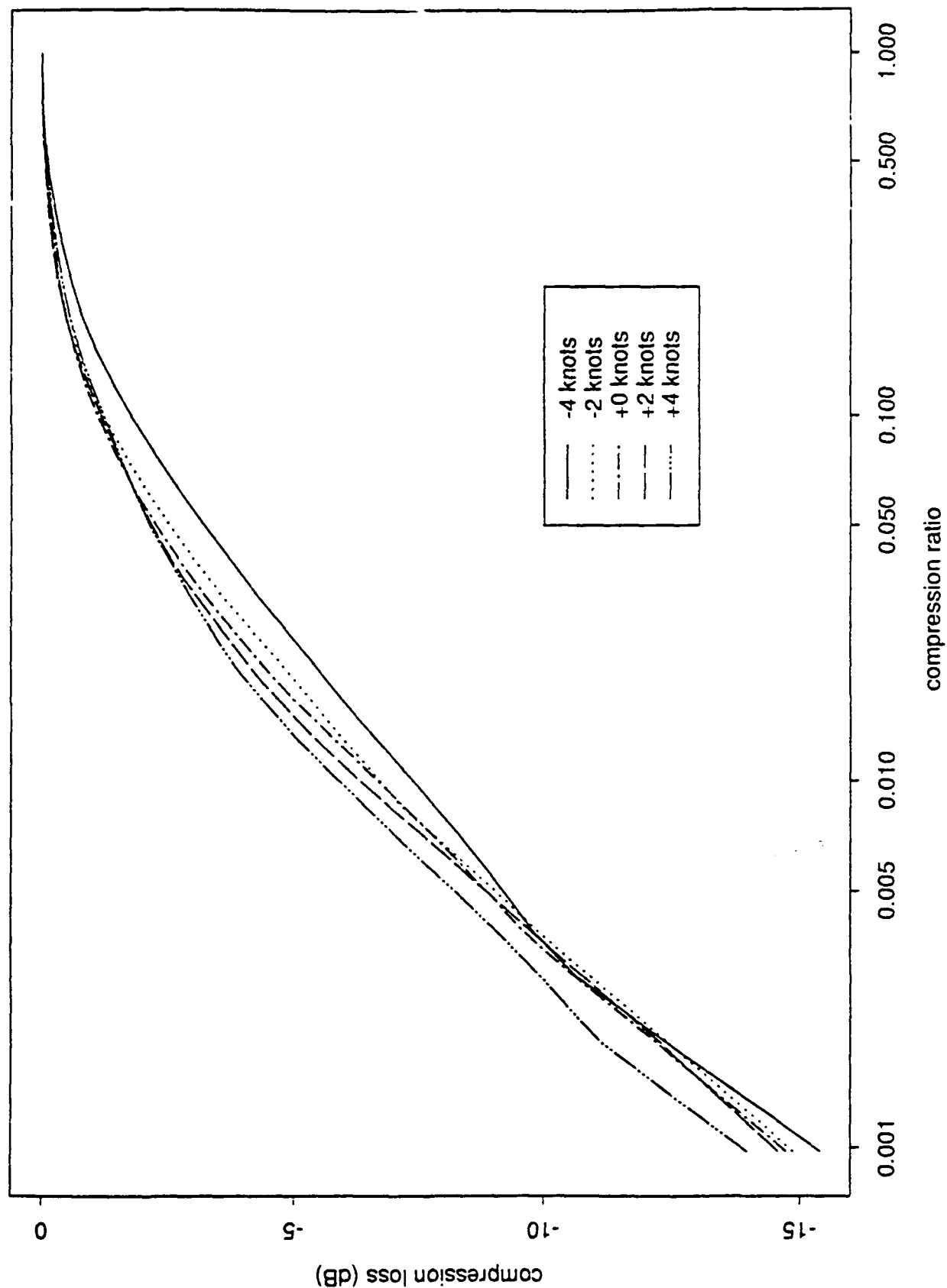


Figure VII-30

COMPRESSION LOSS, CHIP2 WITH DOPPLER, CHIP2 - BINARY DECOMPOSITION

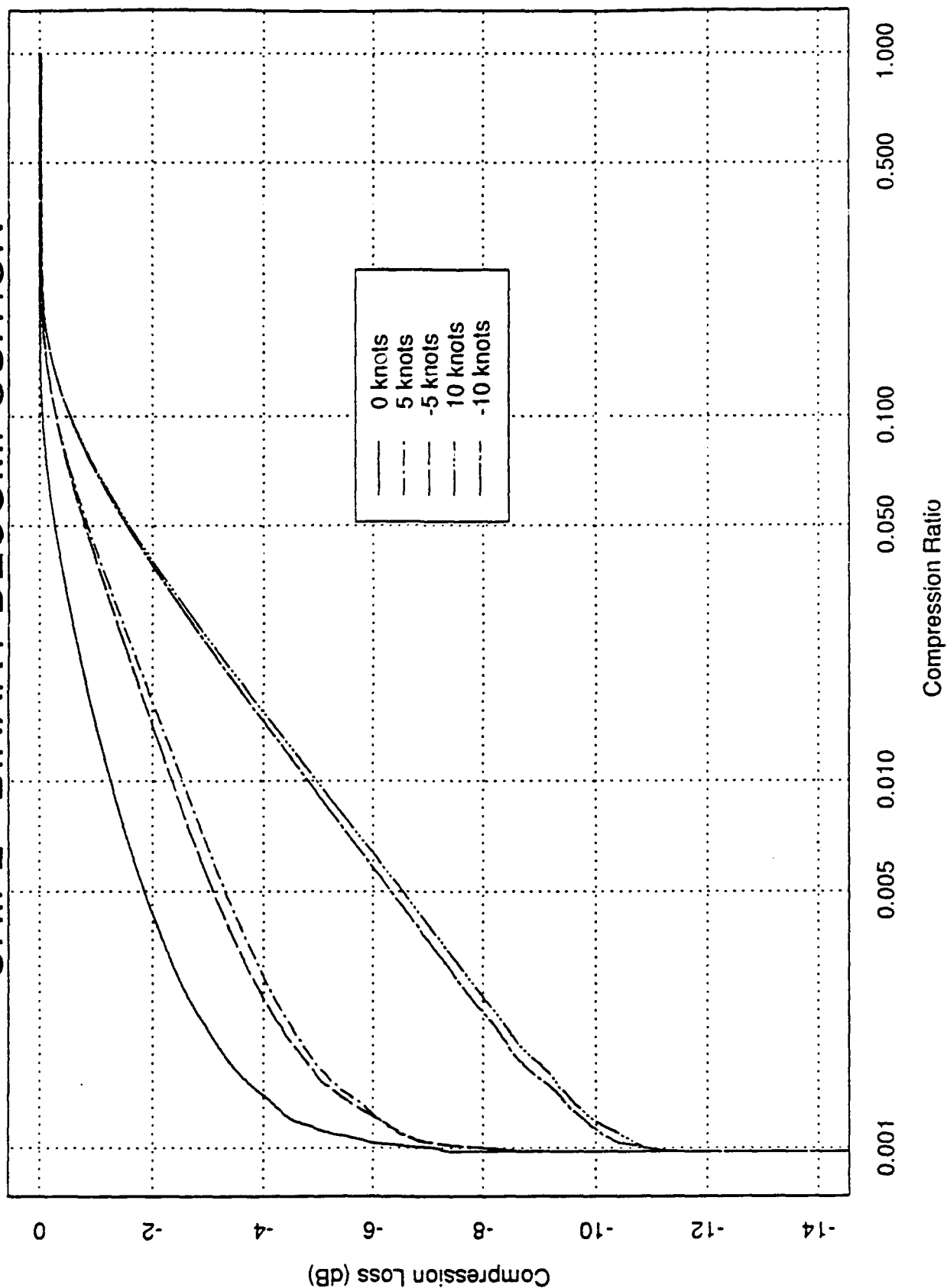


Figure VII-31

COMPRESSION LOSS, CHIP2, -4 KNOTS DOPPLER

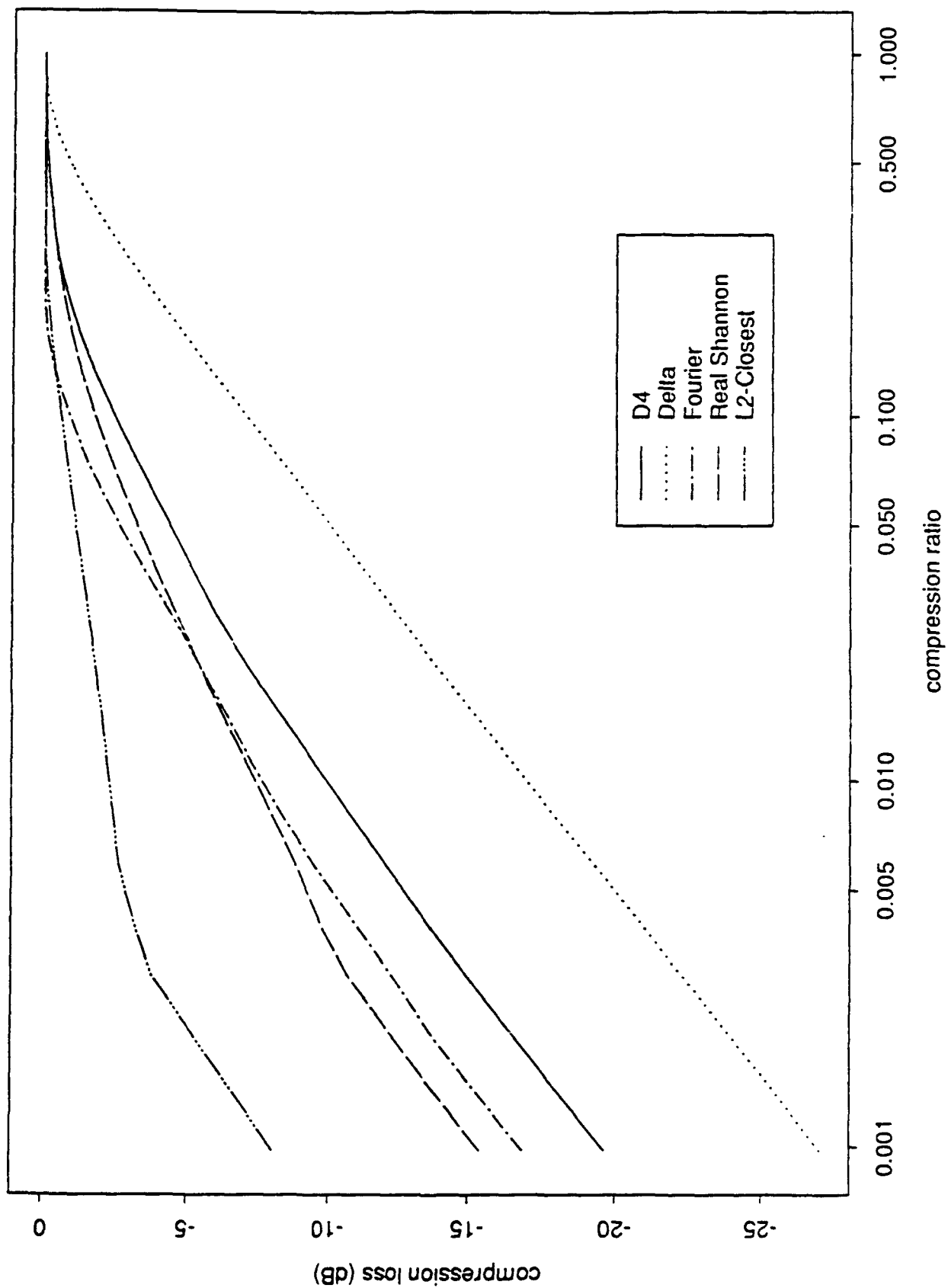


Figure VII-32

COMPRESSION LOSS, CHIP2, DOPPLER COMBINED

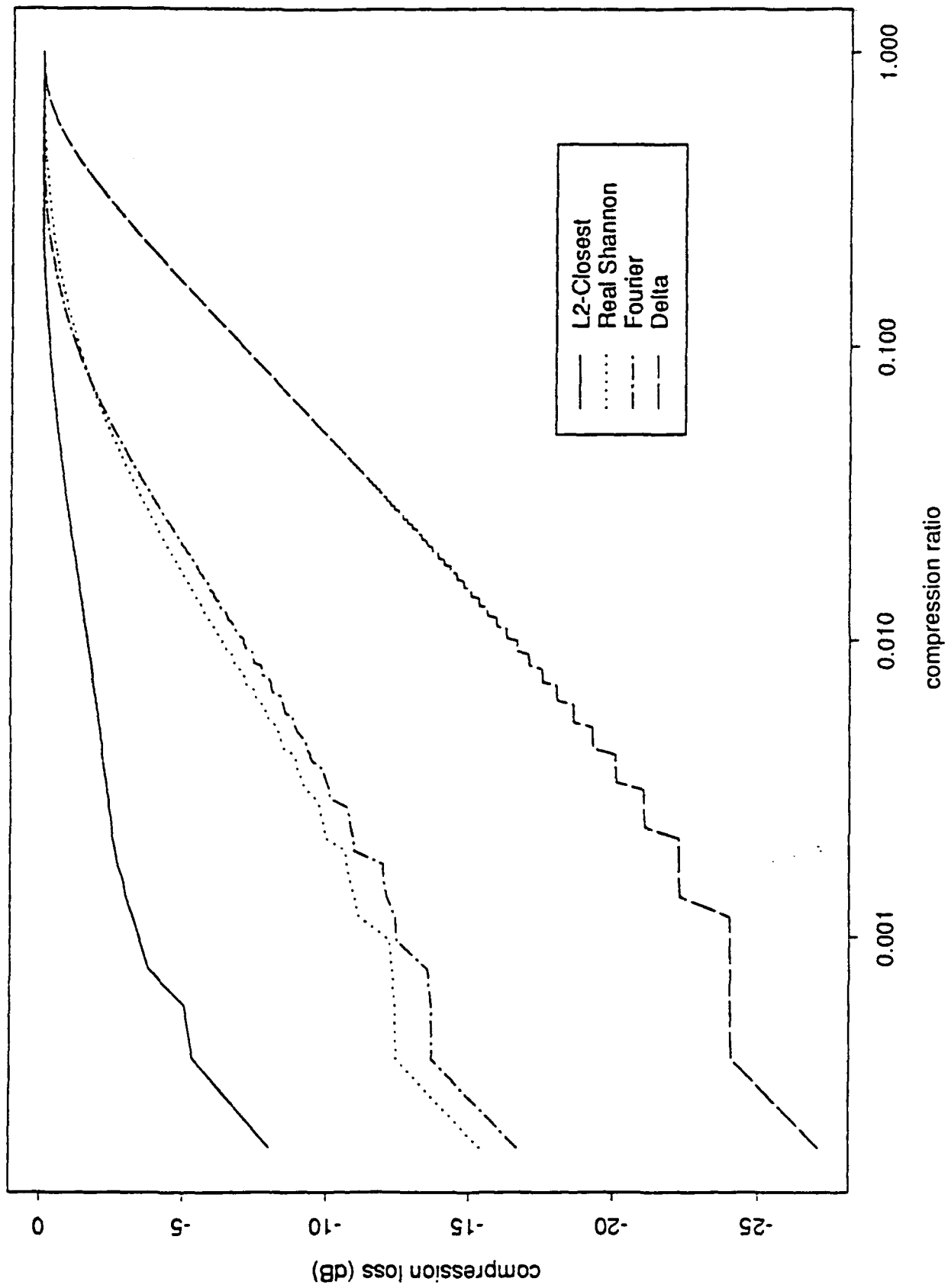


Figure VII-33

Compression Loss vs Time Varying Basis

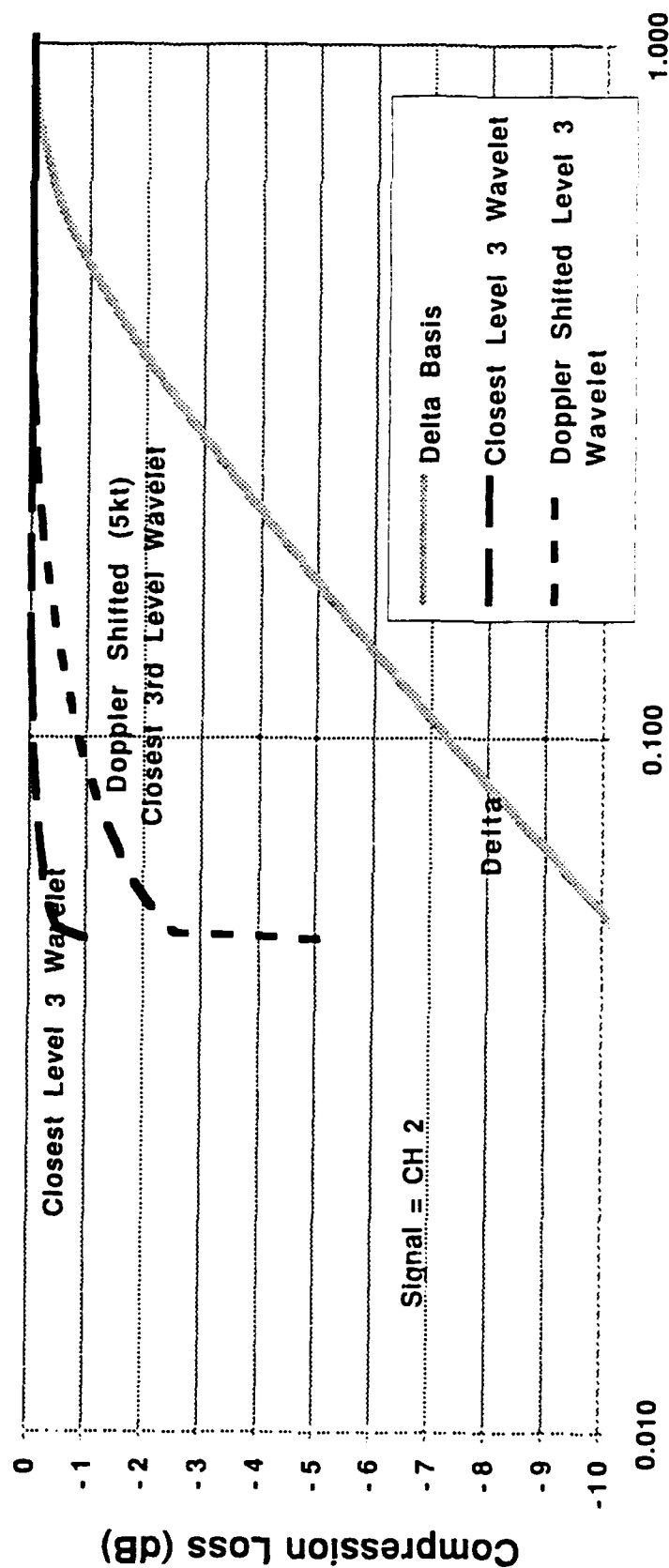


Figure VII-34

CHAPTER VIII

CONCLUSIONS FROM THE PRESENT RESEARCH

We summarize the main results achieved in our research program on LFA/LPI signals. This chapter is divided into two main sections, the first concerns the experimental results and the second concerns the theoretical results. We will discuss improvements and future work in the following chapter.

I. Experimental Results

Our efforts have generated the following experimental results:

- A compressed detection method and a detector that suffers the least degradation due to compression, in head-to-head comparison to other detector choices.
- A multi-channel detector for simultaneously detecting possible Doppler and time shifts of the return signal, relative to the prototype signal.
- A transmission simulation system (TSS) that simulates all phases and major environmental effects encountered by underwater sonar signals during their propagation.

Compressed Detector. Our compressed detector is based on the compressed Neyman-Pearson detector (see following section on theoretical results). We tested several bases to determine which performed better. The results (see Chapter VI for details on the tests and Chapter VII for the results) show the l^2 -closest wavelet basis significantly outperforms all other bases, including other standard wavelet bases, like the Daubechies D_4 basis and the real Shannon basis. The l^2 -closest wavelet basis detector is essentially a matched filtering system. It does have drawbacks, which we acknowledged and dealt with through the use of the binary decomposition method for detection purposes.

We emphasize that our compressed detector is indeed compressed: of the 1024 data points describing a finite discrete signal picked up by the detecting window, we use on the order of \sim to

16 data points for detection purposes and have losses that are less than 2 – 3dB overall! Figures VII-(18) though VII-(33) show that the detector using the l^2 -closest wavelet basis suffers very little degradation compared to detectors using the Fourier, the delta, or other wavelet bases. In order to perform compression, the signal must be transformed into the selected wavelet basis. We have shown that this can be done rapidly with little impact on the speed gains due to compression.

Simulation. The transmission simulation system allowed us to simulate Doppler and time-delay effects on prototype signals. We also wanted the prototype signals to be relevant to actual sonar signals and so, we developed a program to generate these signals. The combination of having a Doppler simulator and real-life signals allowed us to test the effectiveness of the detector. Our research in this direction led us to develop the multi-channel detector, which is capable of simultaneously detecting possible Doppler and time shifts of the signal.

The transmission simulation system involves over 10,000 source lines of code. Our updated version includes the Pecris Model to deal with shallow water channels, in which bottom bounces have an appreciable effect on the signal. The simulation is also equipped to compute Doppler ambiguity displays as well as wavelet and Fourier waterfall displays. The transmission simulation system is described in Chapter VI. It figures prominently in testing the multi-channel detector and other detection methods (see Chapter VII for the results of these tests).

Multi-channel Detector. The multi-channel detector performed as intended, emphasis on the recursive nature of wavelets led to fast computation and minimal storage requirements. Unfortunately, experiments conducted with the multi-channel detector did not illustrate its full capabilities, due to the poor choice of prototype signals. We address future experiments on the multi-channel detector in the next chapter.

2. Theoretical Results

In the theoretical arena, we have researched into the following:

- Near-optimal detectors, based on the optimal Neyman-Pearson detector.
- A binary decomposition method for signal detection to address the signal translation issue.

- New approaches to using discrete wavelets for detection methods as well as for perfecting time-frequency distributions.
- A better understanding of signals from using time-frequency analysis.

Detection. During our research efforts, we originally devised a detection method which was eventually shown to be suboptimal. Our research showed the Neyman-Pearson detection method is optimal, and thus, should be implemented. However, the Neyman-Pearson detector requires enormous computing efforts not available for real-time detection and immediate decisions. We then developed the compressed version of the detector so that this compressed version became much faster.

In conjunction with the detector is the detector basis. The choice of basis may allow for additional compression without significant degradation. Through wavelets, we discovered that the l^2 -closest wavelet basis yields very little loss even at high compression.

Binary Decomposition. Other uses of wavelets include the binary decomposition method, which has the additional capability of detecting translates of the signal better than just the l^2 -closest wavelet basis. We also studied the possibility of creating noise-optimal wavelets. Such wavelet bases would discriminate the signal from the noise by "matching" the wavelets to the noise. Then, the wavelet coefficients corresponding to the noise would be concentrated over a small support, disjoint (hopefully) from the support for the signal coefficients. Our results here showed that such bases were highly dependent on the noise and often affected the signal negatively and thus, such wavelets were eventually discarded.

Our work in developing signals created by wavelets showed that this procedure was indeed possible, but the process does not match the capabilities of current sonar signal generation methods. Recently, we have developed a wavelet spectrogram from our work in time-frequency analysis. This new tool may revive our signals generation goal with a new procedure that will definitely be fast and can be tailored to have specific characteristics. We will elaborate upon this in the following chapter.

Time-Frequency Analysis. Time-frequency analysis, performed by computing a time-frequency distribution, is a viable tool for investigating the properties of a signal, especially highly non-stationary signals, such as transient sonar signals. Our research into this area came only recently. We plan for further work in this area, as described in the next chapter.

CHAPTER IX

RECOMMENDATIONS FOR FUTURE RESEARCH

In this chapter, we discuss areas in which further work will benefit DARPA's LFA program.

1. Experimental

This area addresses testing of the compressed wavelet detector and the multi-channel detector. To date all of the testing of the detectors has been with simple simulation models such as the Pecris model. Further testing is necessary to demonstrate the effectiveness of the detectors in a real-world scenario. The following is recommended.

- Incorporate the Safari Model into the LFA Simulation.
- Perform testing of the compressed detector and the multi-channel detector using the Safari model to simulate the sound channel
- Perform testing of the compressed detector and the multi-channel detector using a sound channel derived from a real world experiments using an impulse charge at-sea.
- Perform test of the compressed detector and the multi-channel detector using the derived real world channel and signals actually generated and received at-sea.
- Determine the sensitivity of the multi-channel detector to Doppler shifts using a signal with greater Doppler dependence.

For example, our use of wavelets over the span of this research phase has evolved from signal generation to signal processing. We now feel this is the proper role for wavelets in regard to LFA/LPI signals. We also have reason to believe that wavelets will provide a new means to signal generation, one that we did not consider during our current research phase.

2. New Development

Future theoretical research topics include:

- Signal generation using the wavelet spectrogram. This effort is long-term.
- Time-frequency distribution for non-stochastic noise analysis. This work is definitely short-term.
- Additional utilizations of the l^2 -closest wavelet basis. This study is potentially a long-term research problem.
- Other detection methods. This research topic is most likely a long-term research proposal.
- Technical merits of the binary decomposition method. This effort is short-term.

We were asked to study the possibility of creating signals having prescribed Doppler Ambiguity displays (see Chapter V, Section 2 for a brief description of Doppler Ambiguity plots). We were able to construct signals having certain properties, as suggested by their Doppler Ambiguity plots, but we have not been able to take an ambiguity plot and create a signal from it. We have made some progress in this area and see this as a possible short-term effort.

Although our use of wavelets has moved from signal generation to signal processing, we do see a possibility of the application of wavelets in signal generation. This application relates to the wavelet spectrogram. One theoretical advantage of the wavelet spectrogram is that it is an invertible process. While all the other T-F distributions are non-invertible processes (i.e., many signals may yield the same T-F distribution plots, due to taking the absolute value and due to the localizing nature of the distribution functions), the wavelet spectrogram is an invertible process; for each signal, there is a unique wavelet spectrogram plot, and conversely. This means there is a quick way to construct a signal with a prescribed wavelet spectrogram. More importantly, one must understand that this process cannot be accomplished with any of the other T-F distributions. In this aspect, signal generation is a long-term effort.

This use of wavelets will enable us to model noise more effectively than our current moving-average methods. Certain noises, like biologics and reverberation, are not completely

stochastic; there are certain key frequencies that characterize the noise. These frequencies can be determined through T-F distribution plots, and time-series noise can be recreated by an inverse wavelet spectrogram.

For short-term efforts, we would like to apply the detector on the T-F distribution data. Moreover, we have worked on a classification method to classify families of signals. We would like to apply this classification method to T-F distributions. In this way, we can classify signal types by the signal's spectrogram.

Finally, we want to determine some of the technical merits of the ψ -binary decomposition algorithm for detection purposes. The ψ -binary decomposition algorithm was developed late in the research phase and has not been fully tested. Testing it will be a short-term effort.

We would like to consider other detection methods. Although the Neyman-Pearson detector is optimal, the compressed Neyman-Pearson is only near-optimal. Perhaps there is an alternative detection method that yields better results for equal or comparable computing effort.

3. Conclusion

We believe that our research to date has demonstrated the utility of wavelets in the fields of signal generation, signal processing, detection, and classification. We have developed, in particular, detection algorithms that have greater accuracy and greater speed than the standard techniques in use. It has become evident from our research on this project that wavelet theory is an immensely promising and fruitful field of research with many potential applications; continued research is truly imperative. It is our hope to be a part of that continued effort and to follow up on the potential topics for further study that arose during the research performed for this project.

References

- [a] User's Guide: Low Frequency Active Simulation System, Daniel H. Wagner Associates BAA Final Report for the basic contract with DARPA, by D. Bernhart, K. Holmquist, and A. Schillace, September 1992.
- [b] Discrete-Time Signal Processing, A Oppenheim, R. Schafer, Prentice Hall, Englewood Cliffs, New Jersey, 1989.
- [c] Low Frequency Active Signal Detection Methodology and Simulation Employing Discrete Wavelet Transforms, Daniel H. Wagner Associates Draft Technical Report to DARPA, by E. Dew, R. Lipshutz, and D. Miner, August 1992.
- [d] Applications of Wavelet Theory in Transient Signal Detection and Classification, Daniel H. Wagner Associates Phase II SBIR Final Report to DARPA, by R. Lipshutz, M. Grunert, E. Dew, D. Miner, D. Bernhart, A. Caramagno, and K. Thrift, in preparation.
- [e] "Theory of Communications," D. Gabor, J. Inst. Elect. Eng. (London), Vol. 93, 1946.
- [f] "Multiresolution approximations and wavelet orthonormal bases in $L^2(\mathbf{R})$," S. Mallat, Trans. of the American Mathematical Society, Vol. 315, No. 1, 69-87, 1989.
- [g] "Orthonormal Bases of Compactly Supported Wavelets," I. Daubechies, Comm. Pure Appl. Math., Vol. 41, 909-996, 1988.
- [h] Ondelettes et Operateurs, Y. Meyer, Vol.1, Hermann, Paris, 1990.
- [i] "Ondelettes et Bases Hilbertiennes," P. J. Lemarie, Y. Meyer, Rev. Math Iberoamericana, Vol. 2, Nos. 1 and 2, 1986.
- [j] "Wavelets in Numerical Analysis," G. Beylkin, R. Coifman, V. Rokhlin in Wavelets and Their Applications, M. B. Ruskai, et. al., eds., Jones and Bartlett, Boston, 1992.
- [k] "Some Preliminary Results Concerning l^2 -closest Wavelets," E. Dew, in preparation.
- [l] Applications of Wavelet Theory in Transient Signal Detection, Daniel H. Wagner Associates Phase II SBIR Semi-Annual Report to DARPA, by R. Lipshutz, M. Grunert, C. Peters, L. Jevons, and D. Bernhart, November 1991.
- [m] LPI/LFA Technical Final Report, Daniel H. Wagner Associates BAA Final Report for the basic contract with DARPA, by R. Lipshutz, E. Dew, K. Holmquist, A. Schillace, February 1992.
- [n] Sonar Signal Processing, R. Nielson, Artech House, Inc., Mass., 1991.
- [o] Underwater Acoustic System Analysis, 2nd Ed., W. Burdic, Prentice Hall, Englewood Cliffs, New Jersey, 1991.

- [p] "On Sonar Signal Analysis," C. Black, T. Glisson, A. Sage, IEEE Transactions on Aerospace and Electronics Systems Vol. AES-6, No. 1, January 1970.
- [q] "Asymptotic Evaluation of the Ambiguity Functions of High-Gain FM Matched Filter Sonar Systems," B. Harris, S. Kramer, Proceedings of the IEEE, Vol. 56, No. 12, December 1968.
- [r] Principles of Underwater Sound, 3rd Ed., R. Urick, McGraw-Hill Book Co., New York, 1983.